

SPECKLE AND MOTION BASED VASCULAR IMAGE ANALYSIS FOR
OPTICAL COHERENCE TOMOGRAPHY

by

Ho Yiu Cheng

A thesis submitted in conformity with the requirements
for the degree of Doctor of Philosophy
Graduate Department of Electrical and Computer Engineering
University of Toronto

© Copyright 2015 by Ho Yiu Cheng

Abstract

Speckle And Motion Based Vascular Image Analysis for Optical Coherence Tomography

Ho Yiu Cheng

Doctor of Philosophy

Graduate Department of Electrical and Computer Engineering

University of Toronto

2015

Optical Coherence Tomography (OCT) is an emerging optical imaging modality that is capable of imaging biological tissues with micron resolution and millimeter penetration depth. In clinical diagnostic imaging and pathology, OCT has helped fill a gap in terms of both resolution and imaging depth, in between traditional fluorescence based microscopes and non-invasive organ level imaging. In this domain, OCT can be used both as an *ex vivo* pathological examination tool or *in vivo* imaging modality.

As OCT becomes more diversified, data obtained also become more diversified in terms of information but more complicated. For instance, in catheter based endovascular OCT (EV-OCT), data were acquired radially instead of the traditional raster scanning. Moreover, during the pullback scanning in EV-OCT, motion artefacts are severe and this restricts the amount of functional information to be obtained. Furthermore, as OCT imaging speed becomes faster, reaching as high as 3.2 MHz axial scan rate [1], flow imaging is obliged to undergo paradigm shift, particularly from conventional ultrasound practices.

The main goal of this thesis was to address the development and validation of a set of algorithms that tackle these problems we now face in modern OCT systems and increase the utility of information obtained. In this thesis, an experimental protocol was first developed for proper porcine carotid arterial EV-OCT imaging. The data obtained were then utilized for the first time to dynamically detect microvessels (*vasa vasorum*) in major

arterial wall. Meanwhile optimized digital speckle noise removal was performed for the first time on Fourier domain EV-OCT system data to further facilitate vessel wall evaluation and microvessel detection. Lastly, a novel depth enhanced OCT microangiography algorithm was devised for *in vivo* microvascular imaging of malformed vascular networks of human skin with genetic origins for the first time. The significance of this thesis lies in the potential of helping better understand the mechanism, progression and the effect of therapeutic intervention on various vascular diseases such as atherosclerosis and hereditary hemorrhagic telangiectasia. Better preventive measures and treatment options can ultimately be devised with advanced understanding of vascular diseases formation.

Dedication

With my deepest and warmest gratitude and love, I dedicate this thesis to my mother, who is always supportive of my endeavors with encouragement and selfless guardianship and who has helped me get through numerous obstacles and difficult times. I also want to dedicate to Winnie, who has journeyed with me in my ventures and always lightened me with happiness.

Acknowledgements

I feel very grateful for the technical and scientific support from both of my supervisors, Prof. Victor X. D. Yang and Prof. Peter R. Herman. I am especially thankful for their advice on some other life matters in Canada. Over the years, I am also very lucky to have worked with many brilliant and intelligent students, technicians, scientists and professors, including but not exclusively Dr. Kenneth Lee, Dr. Adrian Mariampillai, Dr. Beau Standish, Ms. Lauren McKeeman, Ms. Danielle Gifford, Dr. Adili Reheman, Dr. Juan Cruz, Dr. David Cadotte, Mr. Jason Grenier, Mr. Michael Leung, Dr. Moez Haque, Dr. Jianzhao Li, Dr. Luis Fernandes and Dr. Stephen Ho. I would also like to thank my fellow graduate students friends Dr. Fei Ye, Mr. Yiwei Zhang, Mr. Zhiyuan Tang and Mr. Liang Yuan for their sharing and advice. I am absolutely honored to have Prof. Brian Wilson and Prof. Stewart Aitchison sparing their precious time to advise me in my thesis advisory committee. Lastly, I would like to thank the whole University of Toronto Electrical and Computer Engineering Connection Conference 2013 Organization Committee to give me a chance to work and learn with them as the treasurer.

Over the four years of my PhD studies, I have been fortunate to have the support of the graduate scholarship from the Edward S. Rogers Sr. Department of Electrical and Computer Engineering. I also have the honor to be able to receive the SPIE Officer Travel Grant to attend the student leadership workshop hosted by the annual SPIE Optics + Photonics Conference, in which I have learnt a lot in organizational skills which turned out to be useful to my research and activity organization afterwards. I have also received the SPIE Optics and Photonics Education Scholarship to further support my studies.

Contents

1	Introduction	6
1.1	Principle of Optical Coherence Tomography (OCT)	6
1.2	Functional imaging using OCT	11
1.3	Intravascular / Endovascular OCT	13
1.4	Alternative technologies	15
1.5	Current limitations in OCT and their remedies	21
1.6	Thesis outline	22
2	OCT Anatomical and Vascular Imaging	23
2.1	Vascular imaging and its applications	23
2.2	OCT Imaging for Disease Diagnosis	25
2.3	OCT for Therapeutic Monitoring	28
2.4	OCT for Functional Imaging	29
2.5	Atherosclerosis	30
2.6	Current capabilities of EV-OCT	32
2.7	Hereditary vascular diseases	34
2.8	Conclusion to Introduction: Motivation of the Thesis	35
3	Theoretical Basis and Algorithm Development	38
3.1	Candidate Contribution	38
3.2	Image Formation	38

3.3	Basic Common Image Processing Techniques	39
3.4	Information Divergence	40
3.5	Speckle, Origin and Characteristics in OCT	41
3.6	Motion in OCT and its Relationship with OCT Speckle	42
3.7	Application I: Detection of Vasa Vasorum using Higher Order Statistics .	44
3.8	Application II: Speckle Reduction by a Parametric Iterative Algorithm .	49
3.9	Summary of Chapter 3	52
4	Feasibility of Endovascular OCT in Carotid Artery of Large Mammals	53
4.1	Candidate Contribution	53
4.2	Endovascular Imaging Protocol	53
4.3	OCT Imaging of Healthy and Thrombi Filled Carotid Artery	56
4.4	OCT Guidance in Carotid Stenting	57
4.5	Impact of EV-OCT on Neurovascular Interventional Procedures	61
4.6	Preliminary Study on Vasa Vasorum Detection	66
4.7	Speckle Reduction of Endovascular OCT	79
4.8	Summary of Chapter 4	92
5	OCT Micro-Angiography for Hereditary Hemorrhagic Telangiectasia	93
5.1	Candidate Contribution	93
5.2	Depth Enhanced OCT Micro-Angiography	93
5.3	Experimental Setup	97
5.4	Phantom Results of Depth Enhanced OCT Micro-Angiography	99
5.5	Hereditary Hemorrhagic Telangiectasia	99
5.6	Initial Demonstration of In Vivo Monitoring of Skin Abnormal Vasculature of HHT patient	102
5.7	Advantages, Limitations and Potentials of Depth-Enhanced OCT Micro- angiography	107

5.8	Summary of Chapter 5	110
6	Discussion, Summary and Conclusions	112
6.1	Discussion and Impact of the Work	112
6.2	Summary	115
6.3	Future work	117
A	Data Processing Codes	120
	Bibliography	133

List of Tables

1.1 Resolution and Penetration Depth of different imaging modalities.	16
4.1 Metrics Comparison Between the Original Image and Processed Images Using Different β	84

List of Figures

1.1	First generation OCT design.	8
1.2	Exemplary OCT interferogram when a single reflector is placed on the sample arm beam path.	9
1.3	Schematics of an exemplary SS-OCT.	11
1.4	Exemplary intravascular OCT catheter.	13
1.5	Exemplary EV-OCT dataset.	14
1.6	Competing intravascular imaging technologies.	16
1.7	An exemplary intravascular ultrasound probe.	18
1.8	Laser speckle imaging setup.	20
2.1	Exemplary OCT image of the retina at the macula.	27
2.2	Types of Atherosclerotic Plaques	31
2.3	Fibrocalcific plaque with lipid pools.	33
2.4	Red and white thrombi.	34
2.5	Cerebrovasculature in the skull base region.	36
3.1	H&E staining of porcine carotid artery. The black arrows point to vasa vasorum at the adventitia.	45
3.2	Different types of vasa vasorum.	47
4.1	Operating room setting for porcine experiments.	54
4.2	Schematics of carotid EV-OCT catheter system.	55

4.3	EV-OCT images of normal porcine carotid artery	58
4.4	H&E staining of normal porcine carotid artery.	58
4.5	Elastin trichrome staining of normal porcine carotid artery.	59
4.6	EV-OCT image of porcine carotid artery undergoing vasospasm.	59
4.7	3D view of vasospasm.	60
4.8	Flattened view of porcine carotid artery adventitia.	60
4.9	Side view of flattened adventitia.	61
4.10	EV-OCT image of stented porcine carotid artery.	62
4.11	3D rendering of properly stented pig carotid artery	62
4.12	Stented porcine carotid artery with clots formed over the stent.	63
4.13	3D rendering of stented porcine carotid artery with blood clots.	63
4.14	Image jittering resulting from excessive contrast injection or high imaging catheter pull-back speed.	64
4.15	EV-OCT image artifacts caused by double reflection.	65
4.16	30 gauge flow phantom results of kurtosis analysis.	68
4.17	EV-OCT image of the blood-saline flush experiment.	69
4.18	svOCT image of the blood-saline flush experiment.	70
4.19	One example kurtosis map of the blood-saline flush experiment when the flow took on a sudden change.	70
4.20	Stationary EV-OCT image of porcine carotid artery when the imaging catheter is placed close to the vessel wall.	71
4.21	svOCT of porcine carotid artery with the catheter parked.	72
4.22	Kurtosis signal map of porcine carotid artery when the imaging catheter is placed close to the vessel wall.	72
4.23	Average intensity of a region of interest around the vasa vasorum and an arbitrary section of the vessel wall versus time.	73

4.24 Average speckle variance of suspected vasa vasorum region and arbitrary vessel wall versus time.	74
4.25 Average kurtosis of suspected vasa vasorum region and arbitrary vessel wall region versus time.	74
4.26 H&E staining of porcine carotid artery. The black arrows point to vasa vasorum at the adventitia.	75
4.27 Structural image of vasa vasorum data set 2.	76
4.28 Kurtosis map of vasa vasorum data set 2.	77
4.29 Speckle reduction of EV-OCT finger skin image.	81
4.30 Original porcine carotid artery EV-OCT image before speckle reduction.	81
4.31 Despeckled porcine carotid artery EV-OCT image.	82
4.32 Enlarged view of the red ROI in the porcine arterial wall image.	83
4.33 Enlarged view of the green ROI in the porcine arterial wall image.	84
4.34 Trade-off between CNR and edge preservation by adjustment of β	85
4.35 Original EV-OCT image of vasa vasorum.	86
4.36 EV-OCT image of vasa vasorum after speckle reduction when the major artery was cleared of blood.	86
4.37 EV-OCT image of vasa vasorum before speckle reduction when blood flows back to the major artery lumen.	87
4.38 EV-OCT image of vasa vasorum after speckle reduction when blood flows back to the major artery lumen.	87
4.39 Vasa vasorum detection using kurtosis as validation.	88
4.40 EV-OCT vasa vasorum imaging scenario.	89
4.41 M-Mode image of the vasa vasorum.	90
4.42 Atherosclerotic plaque image before speckle reduction.	90
4.43 Atherosclerotic plaque image post speckle reduction.	91
5.1 Plots of the imaginary parts of the different characteristic functions.	95

5.2	Interface used for HHT imaging.	96
5.3	Schematic of OCT setup for skin microangiography.	98
5.4	Agrose phantom experiment for Depth Enhanced OCT Micro-Angiography.	100
5.5	Human HHT skin lesion.	101
5.6	B-mode angiography of healthy fingernail root.	103
5.7	In vivo Depth Enhanced OCT Micro-Angiography of human fingernail root and skin HHT lesion.	105
5.8	Depth Enhanced OCT Micro-Angiography of a placebo HHT lesion. . .	106
5.9	a) Treated HHT lesion 1, week 1; b) Treated HHT lesion 1, week 3; c) Treated HHT lesion 1, week 5; d) Treated HHT lesion 1, week 7. Scale bar represents 300 μ m;	108
5.10	a) Treated HHT lesion 2, week 1; b) Treated HHT lesion 2, week 3; c) Treated HHT lesion 2, week 5; d) Treated HHT lesion 2, week 7. Scale bar represents 300 μ m;	111
6.1	Zemax simulation of proposed catheter imaging probe design.	118

List of Publications

Refereed Journals

1. **Kyle H. Y. Cheng** ; Adrian Mariampillai ; Kenneth K. C. Lee ; Barry Vuong ; Timothy W. H. Luk, et al., "Histogram flow mapping with optical coherence tomography for in vivo skin angiography of hereditary hemorrhagic telangiectasia", *J. Biomed. Opt.* 19(8), 086015 (Aug 20, 2014);
<http://dx.doi.org/10.1117/1.JBO.19.8.086015>

Contribution: Design of algorithm, alignment of swept source laser for the imaging system, patient scanning, data analysis, manuscript writing.

2. Cuiru Sun, Felix Nolte, **Kyle H. Y. Cheng**, Barry Vuong, Kenneth K. C. Lee, Beau A. Standish, Brian Courtney, Thomas R. Marotta, Adrian Mariampillai, and Victor X. D. Yang, "In vivo feasibility of endovascular Doppler optical coherence tomography," *Biomed. Opt. Express* 3, 2600-2610 (2012).
<http://www.opticsinfobase.org/boe/abstract.cfm?URI=boe-3-10-2600>

Contribution: Organization of and help in animal experiments, help in experiments, help in data processing.

3. **Kyle H. Y. Cheng**, Edmund Y. Lam, Beau A. Standish, and Victor X. D. Yang, "Speckle reduction of endovascular optical coherence tomography using a generalized divergence measure," Opt. Lett. 37, 2871-2873 (2012).

<http://www.opticsinfobase.org/ol/abstract.cfm?URI=ol-37-14-2871>

Contribution: Design of algorithm, organization of and help in animal experiments, data analysis, manuscript writing.

4. **Kyle H. Y. Cheng**, Cuiru Sun, Juan P. Cruz, Thomas R. Marotta, Julian Spears, Walter J. Montanera, Aman Thind, Brian Courtney, Beau A. Standish and Victor X. D. Yang, "Comprehensive data visualization for high resolution endovascular carotid arterial wall imaging", J. Biomed. Opt. 17, 056003 (May 04, 2012);

<http://dx.doi.org/10.1117/1.JBO.17.5.056003>

Contribution: Design of algorithm, organization of and help in animal experiments, data analysis, manuscript writing.

5. **Kyle H. Y. Cheng**, Cuiru Sun, Barry Vuong, Kenneth K. C. Lee, Adrian Mariampillai, Thomas R. Marotta, Julian Spears, Walter J. Montanera, Peter. R. Herman, Tim-Rasmus Kiehl, Beau A. Standish, and Victor X. D. Yang, "Endovascular optical coherence tomography intensity kurtosis: visualization of vasa vasorum in porcine carotid artery," Biomed. Opt. Express 3, 388-399 (2012).

<http://www.opticsinfobase.org/boe/abstract.cfm?URI=boe-3-3-388>

Contribution: Design of algorithm, organization of and help in animal experiments, data analysis, manuscript writing.

Conference Presentations

1. **H. Y. Cheng**, J. Grenier, and P. R. Herman, "Femtosecond Laser-Written Couplers in Fused Silica Fiber: Towards Fiber Cladding Optical Circuits," in CLEO: 2013, OSA Technical Digest (online) (Optical Society of America, 2013), paper CM1H.3.

Contribution: Device fabrication, data analysis, manuscript writing.

2. **Kyle H. Y. Cheng**, Cuiru Sun, Juan P. Cruz, Thomas R. Marotta, Julian Spears, Walter J. Montanera, Peter R. Herman, Aman Thind, Brian Courtney, Beau A. Stan-dish and Victor X. D. Yang, "Feasibility of endovascular optical coherence tomogra-phy for high-resolution carotid vessel wall imaging", Proc. SPIE 8207, 82074N (2012); doi:10.1117/12.910455

Contribution: Design of algorithm, organization of and help in animal experiments, data analysis, manuscript writing.

List of Acronyms

CAS Carotid Artery Stenting

CNR Contrast to Noise Ratio

DOT Diffuse Optical Tomography

ENL Equivalent Number of Looks

EV-OCT Endovascular Optical Coherence Tomography

GI Gastrointestinal

GRIN Gradient Refractive Index

H&E Hematoxylin & Eosin

HHT Hereditary Hemorrhagic Telangiectasia

LSI Laser Speckle Imaging

OCT Optical Coherence Tomography

PAT Photoacoustic Tomography

PDT Photodynamic Therapy

PSF Point Spread Function

ROI Region of Interest

SD-OCT Spectral Domain Optical Coherence Tomography

SMF Single Mode Fiber

SNR Signal to Noise Ratio

SS-OCT Swept Source Optical Coherence Tomography

TD-OCT Time Domain Optical Coherence Tomography

VV Vasa Vasorum

VVI Vasa Vasorum Interna

VVE Vasa Vasorum Externa

VVV Venous Vasa Vasorum

Chapter 1

Introduction

1.1 Principle of Optical Coherence Tomography (OCT)

Optical microscopy has been utilized extensively in the study of biological tissues for over four hundred years. The short wavelength nature of visible light enabled scientists to construct simple wide field optical microscopes that can observe biological samples down to the cellular level by mere human eyes.

The foremost problem of such simple visible light optical microscopes is that the penetration depth of light is limited. Multiple scattering in tissues further complicates the issue, since the random scattering would further reduce the accessible tissue depth. The second problem is that optical sectioning is poor with the common wide field configuration. Since what the human eye can see in optical microscopy is a projection of the back-scattered light, the images from these simple microscopes include tissue signals from a large depth of field.

With the advent of laser scanning confocal microscopes, fluorescence imaging became much more sophisticated, since optical sectioning gained much higher axial resolution with the introduction of the pinhole. However, the pinhole also blocks out a considerable amount of power and thus a smaller pinhole would mean longer image acquisition time

and higher noise in the acquired confocal images. The problem of photobleaching and cytotoxicity of fluorophores are other issues that limit the use of confocal microscopy for *in vivo* scenarios.

The invention of optical coherence tomography (OCT) emerges as a solution which gives both higher optical sectioning resolution and higher penetration depth [2].

The first generation OCT was based on low coherence interferometry. Fig. 1.1 shows the setup of the first OCT design [3]. A Michelson interferometer served as the core element, although other types of interferometers, such as Mach-Zehnder interferometer and common-path interferometer could also be used. Theory and working principles in all OCT variants are the same. Light waves from a low coherence (or high bandwidth) source such as a super luminescence diode or ultrafast laser are directed to the beam splitter. One beam will be directed to the “sample arm” where it would typically consist of the focusing optics and a 2D galvanometer scanner for raster scanning as in typical laser scanning confocal microscopes for spatial mapping. The other beam would be directed towards the “reference arm”. The reference arm typically consists of a single reflection mirror as well as dispersion matching elements. The mirror is dynamically moved back and forth to coherently gate the depth at which the OCT system detects back-scattered photons. Upon reflection from both arms, the returning light would be combined at the beam splitter again. This time, the recombined light would be directed towards the detector for interferogram measurements. Actually, the setup might be slightly more complicated than that. An additional circulator might be in place in order to enable balanced detection, which can improve the signal-to-noise ratio (SNR) by over 10dB.

A sample detected interferogram is shown in Fig. 1.2 where a single mirror is placed at the sample arm with the sample arm length matching the reference arm length. The envelope of this function is called the axial point spread function (PSF) of the OCT system. It represents the detection of a single back-scatterer at any given depth at the sample arm. In general, the deeper it is in the tissue, the lower the signal since the

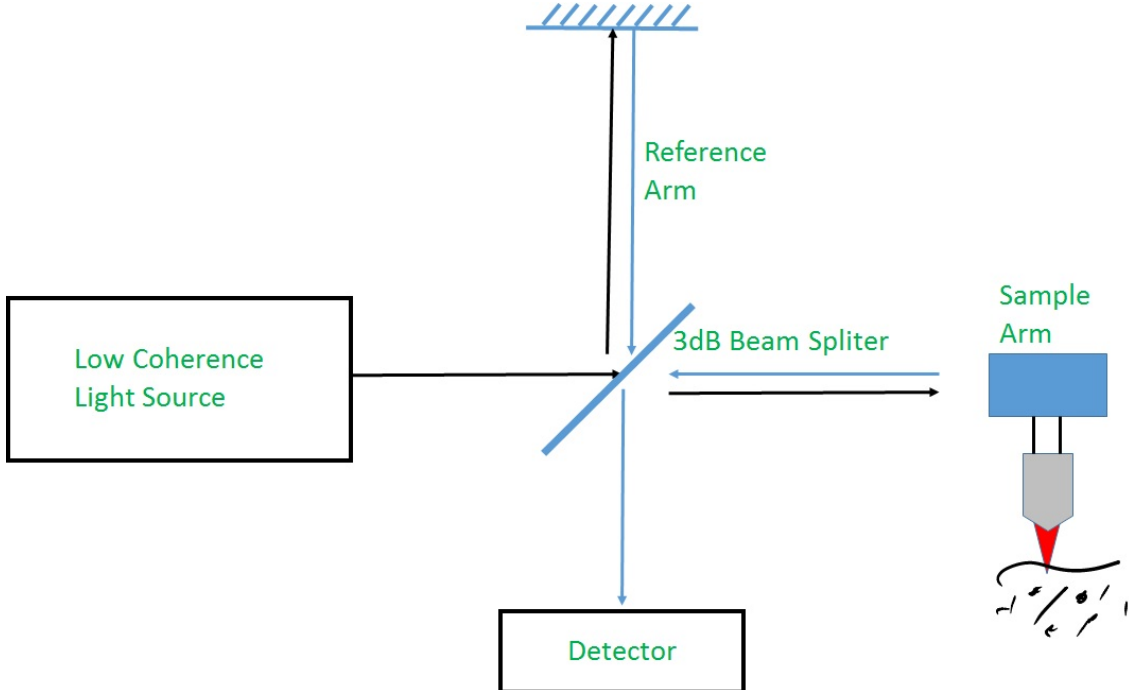


Figure 1.1: First generation OCT design, which is essentially a free space Michelson interferometer.

penetration depth is still limited by tissue absorption and multiple scattering. The full width at half maximum of this envelope function is generally used to describe the axial resolution of the OCT system. Unlike other microscopy techniques though, the axial resolution in general differs from the lateral resolution which is the resolution in the general sense in microscopy. Axial and lateral resolutions are governed by completely different processes and should not be confused with one another. The axial resolution depends on the bandwidth of the imaging light source according to Eq. 1.1:

$$\Delta z = \frac{2\ln 2}{\pi n} \frac{\lambda_0^2}{\Delta\lambda} \quad (1.1)$$

where Δz depicts the axial resolution of the OCT system, n is the refractive index of the biological tissue sample (~ 1.3 - 1.4 in most cases), λ_0 is the center wavelength of the light source and $\Delta\lambda$ is the bandwidth of the light source. For the first generation OCT system, the time-domain OCT (TD-OCT) system, Eq. 1.1 is equivalent to the coherence length

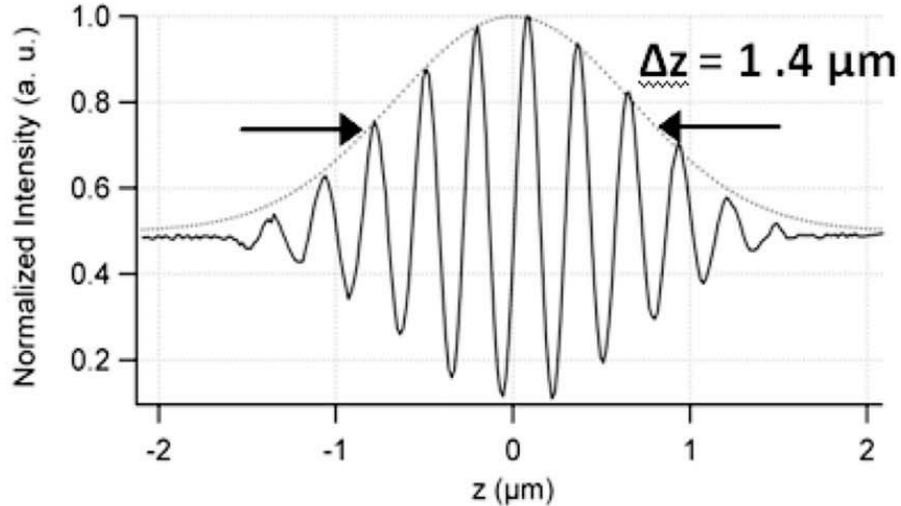


Figure 1.2: Exemplary OCT interferogram when a single reflector is placed on the sample arm beam path. The resolution of the OCT system is characterized by the full width at half maximum of the envelope of this function. Reproduced with permission from [4].

of the light source and therefore, with shorter coherence length, higher axial resolution can be attained for the OCT imaging system. As dictated in conventional microscopy systems, the lateral resolution of OCT is the diffraction limited spot size according to Eq. 1.2:

$$\Delta x \approx 1.22 \frac{\lambda_0 f}{D} \quad (1.2)$$

where Δx is the lateral resolution of the OCT system, f is the focal length of the focusing system and D is the aperture size of the focusing lens in the sample arm beam path.

For any raster scanning modalities, the image acquisition process always suffer time lapses between sample points. These time lapses can be mitigated by increasing the imaging speed and thereby reducing the time the beam stays at one point. For TD-OCT, faster imaging speed can be achieved by more rapid movement of the reference mirror. But even with the application of the rapidly scanning optical delay line in the reference arm, scanning rate can only reach about $\sim 8\text{kHz}$. At this speed, sample scanning takes considerable amount of time and would suffer from severe motion artefact especially

in *in vivo* scenarios. To achieve higher scanning speeds, it is necessary to switch to the more advanced Fourier domain OCT systems.

Fourier domain OCT systems are subdivided into spectral domain OCT (SD-OCT) and swept source OCT (SS-OCT). Each system has its own advantages and both are equally widely used in both research and clinical settings. SD-OCT uses a CCD camera or spectrometer which are more expensive than the detectors employed in SS-OCT. However, SD-OCT offers more phase stability and can be beneficial in phase sensitive flow imaging. SS-OCT in general has higher scan speed, which can benefit OCT imaging in many ways described in subsequent chapters. Theoretical description is very similar between these two categories and in this thesis, the SS-OCT system will be the focus.

An exemplary schematic of the SS-OCT is depicted in Fig. 1.3. Instead of a low coherence light source, a wavelength swept laser is employed. The axial resolution of SS-OCT is equivalent to that of the TD-OCT systems, obeying the same equation as Eq. 1.1. Here in SS-OCT, $\Delta\lambda$ is the wavelength swept range of the wavelength swept laser. Note that although SS-OCT obeys the same axial resolution relationship with the light source as TD-OCT, this equation describes the coherence length of the light source in TD-OCT whilst this is not true for SS-OCT. In SS-OCT, the coherence length is governed by the instantaneous linewidth of the wavelength swept laser. Instead of preferably being short in TD-OCT, longer coherence length is preferred in SS-OCT, since this also means better ranging depth for the OCT system.

Axial scan (A-scan) refers to one line in an OCT tomogram (image) and is obtained by one OCT laser swept in SS-OCT. The interference fringe obtained is Fourier transformed to get the A-scan. Multiple A-scans form a B-frame (a tomogram or an image).

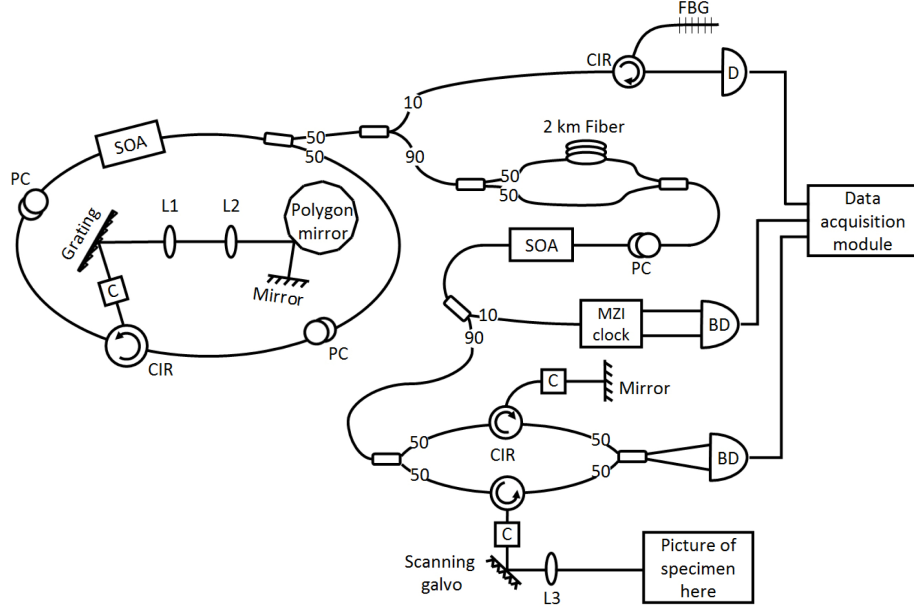


Figure 1.3: Schematics of an exemplary SS-OCT, BD: Balanced Detector, C: Collimator, FBG: Fiber Bragg Grating, MZI: Mach-Zehnder Interferometer, L1-L3: Lenses, PC: Polarization Controller, SOA: Semiconductor Optical Amplifier, reproduced with permission from [5].

1.2 Functional imaging using OCT

Anatomical OCT gives morphological information on the layered structure of biological tissues *in vivo*, where any anomaly can be distinguished easily since the distortion would be clearly visible under near submicron resolution. Furthermore, sophisticated 3D renderings of healthy and diseased tissues can be generated with ease for detailed diagnosis. Although anatomical OCT is powerful, such simple back-reflectivity mapping cannot decipher functional information.

Functional information refers to information regarding the physiological state of the tissue with or without conscious control. An example would be the differentiation between active and necrotic tissues. In anatomical images, their differences are very subtle in terms of pixel amplitude. And moreover, since OCT is not a fluorescence imaging modality, it cannot map out uptake of fluorophores which can relay functional information. Even though their overall morphology would be different, it would take an

experienced OCT operator to decipher the difference. On the other hand, it is easy to differentiate healthy and necrotic tissue in the perspective of blood flow. Healthy tissues are perfused by microcapillaries extensively, whereas necrotic tissues should not be perfused at all. By mapping out blood vessels with active blood flow, one can indirectly infer the physiological state of tissues, even though we cannot see the actual cellular activites from OCT data. Blood flow imaging is particularly important for cancer monitoring, since they are extensively supplied by newly formed microvessels via a process known as angiogenesis. By resolving the microvessel networks within these lesions, not only can the tumor margins be more accurately distinguished, the activity level of the tumor can also be deciphered for multiple purposes more detailedly described in the next chapter [6].

Other than microvascular imaging, OCT can extract functional information in a variety of other ways. By purposely inducing a minute deformation on the tissue between B-frames (one 2D cross-sectional OCT tomogram), the spatial distribution of the mechanical properties of the tissues can be mapped by optical coherence elastography (OCE) [7]. OCE has important applications in cardiovascular diagnosis as well as many other non-medical areas such as material testing [8] and profilometry [9]. For example, in atherosclerosis, different plaque types on the vessel wall differ significantly in the composition and thus elasticity. By mapping the stress and strain of the plaque itself with endovascular OCT, the composition of the plaque can be more accurately determined and thus more suitable treatment options [10] can be chosen.

Recently, various research groups have demonstrated it is possible to use contrast agents for OCT imaging. Gold nanoparticles have been used for target specific photothermal OCT imaging [11].

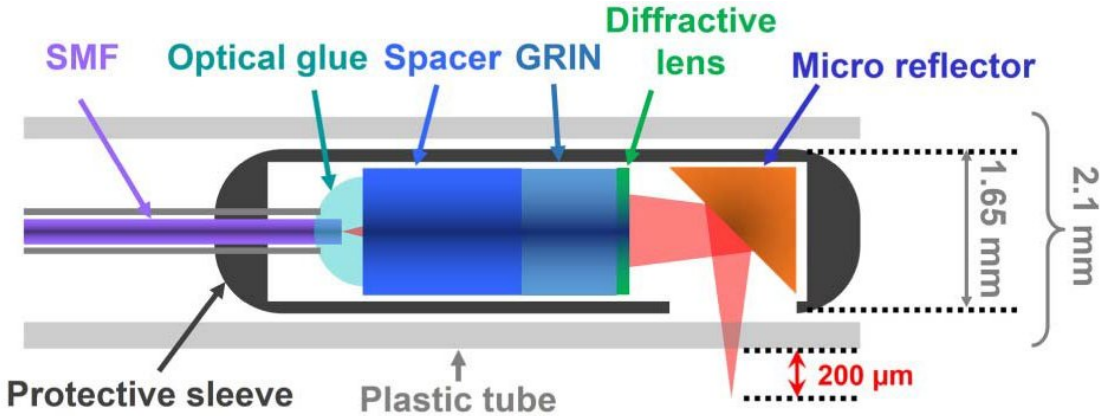


Figure 1.4: Schematic of an ultrahigh-resolution OCT imaging catheter utilizing a diffractive lens to alleviate chromatic aberration. Reproduced with permission from [13].

1.3 Intravascular / Endovascular OCT

Conventional raster scanning based optical imaging is ideal for *ex vivo* tissue samples that can be fixed on a stage; and if the OCT swept source laser sweeps rapidly enough, raster scanning can be suitable for *in vivo* imaging such as the eyes and skin of a patient. However, there are scenarios in which luminal structures are required to be imaged *in vivo*. Examples would be large blood vessels and the gastrointestinal tract [12]. In such scenarios, raster scanning is impossible since no single galvonometer scanner can achieve a 360 degrees angular scanning range. As such another type of optical beam steering probe must be used.

Catheters are a minimally invasive tool used for manipulation in arteries in the heart, neck and brain. Their main uses include aneurysm coiling, balloon angioplasty, stent placement and endarterectomy. Recently, catheters have been modified to be utilized as an imaging device. Fig. 1.4 shows the schematic of an OCT imaging catheter [13].

Endovascular OCT (EV-OCT) catheters typically employ a pullback rotary scanning mechanism. A single mode optical fiber is used to deliver near infrared light through the bulk of the catheter to the targeted region (near the distal end of the catheter). A gradient refractive index (GRIN) lens is then used to focus the light into the blood

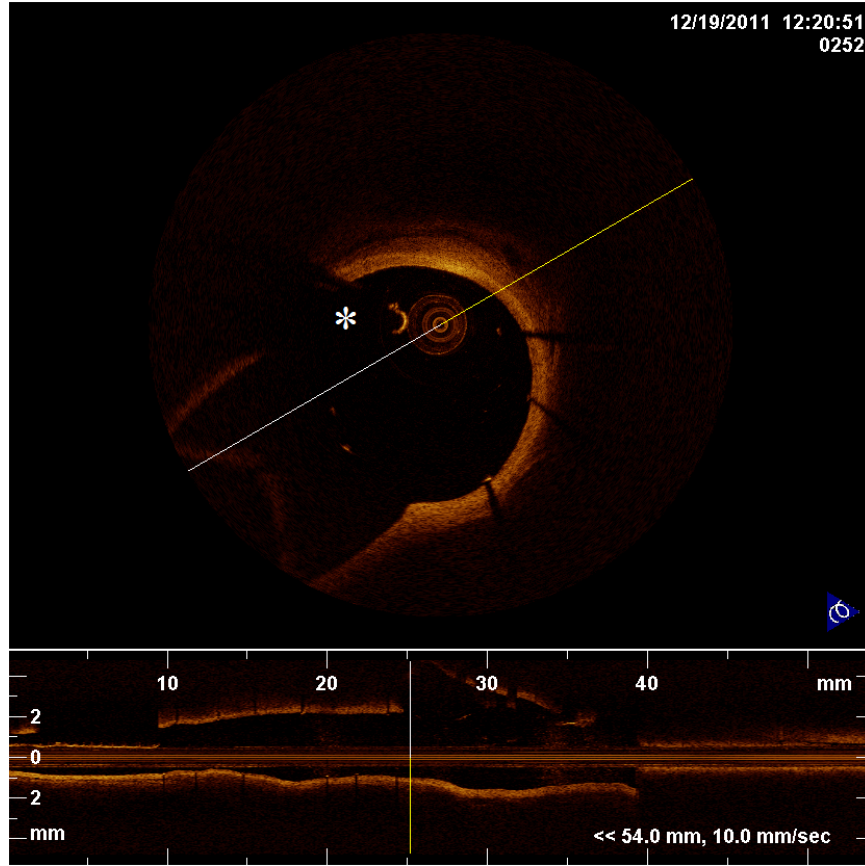


Figure 1.5: Exemplary EV-OCT data set showing a stented porcine artery and one of its projections along the longitudinal direction of the artery. * represents the shadowing artifact caused by the guidewire.

vessel wall tissues. As the imaging session begins, a servo motor begins to pull the whole imaging system back along the blood vessel simultaneously as the imaging beam is continuously and repeatedly rotated 360 degrees. Multiple A-scans from each full 360 degree turn constitute one frame of an EV-OCT image after transformation from the polar coordinates to the Cartesian coordinates. Analogous to spiral CT imaging, these image frames are usually stacked and stitched together to provide a projection at each axis for diagnostic purposes. Fig. 1.5 illustrates the different views of a commercial EV-OCT system:

The projection views are more valuable than individual frames as these projections can give diverse information regarding the atherosclerotic plaque such as size, length,

extent, types and even affected depths of the vessel walls.

1.4 Alternative technologies

Even as OCT has found ample success as a very powerful structural imaging modality, rival optical imaging methods do have their own advantages and specific domains of applications. Resolution is an important factor when considering which methods to use for tissue examination but it is not the only gauge concerning the usability of an imaging modality. Other important factors, some mentioned above, include penetration depth, speed, molecular specificity, tendency to be miniaturized, field of view and most importantly, cost, etc.

Laser scanning confocal microscopy offers the unique ability to map out molecular specific fluorophores to target image a specific type of tissues. Its resolution is typically $\sim 1\mu\text{m}$ or even higher. However, its penetration depth is in general limited ($\sim 300\mu\text{m}$ in skin [14]).

Ultrasound biomicroscopy (UBM) is another rival of OCT. The only difference of UBM versus traditional ultrasound is the use of higher ultrasound frequencies. Its major advantage is that it has $\sim 6\text{mm}$ penetration depth, which is much deeper than that of OCT. However, UBM resolution is on the order of $\sim 25\mu\text{m}$, which is much lower than that of OCT, making depiction of layered structures much more difficult.

Table 1.1 summarizes the resolution and penetration depth of different imaging modalities.

Although EV-OCT has found a unique domain of applications, there are a handful of endovascular technologies that can rival EV-OCT in terms of functionalities [15]. Their working mechanisms are illustrated in Fig. 1.6. Angioscopy can exist as a photographic camera embedded in a catheter or as a laser scanning imaging device [16], taking surface images of the vessel wall as the catheter is advanced. Intravascular ultrasound uses sound

Table 1.1: Resolution and Penetration Depth of different imaging modalities.

	Resolution	Penetration Depth
Confocal Microscopy	$\sim 1\mu\text{m}$	$\sim 300\mu\text{m}$
Optical Coherence Tomography	$\sim 5\mu\text{m}$	$\sim 2\text{mm}$
High Frequency Ultrasound	$\sim 25\mu\text{m}$	$\sim 6\text{mm}$
Low Frequency Ultrasound	$\sim 200\mu\text{m}$	$\sim 5\text{cm}$
Computed Tomography	$\sim 300\mu\text{m}$	Entire Body
Magnetic Resonance Imaging	$\sim 1\text{mm}$	Entire Body

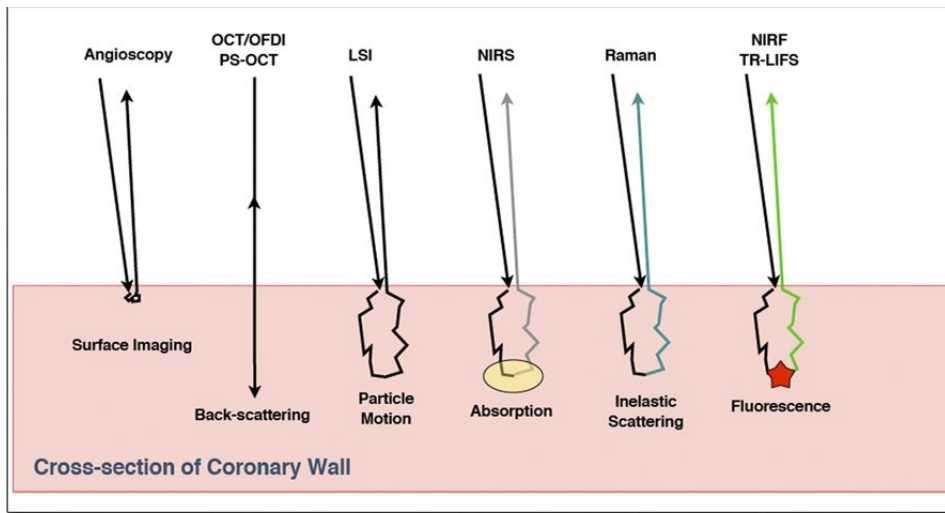


Figure 1.6: The diagram shows the predominant light/tissue interactions that are detected in each of the intravascular optical imaging modalities discussed. LSI: laser speckle imaging; NIRF: near-infrared fluorescence; NIRS: near-infrared spectroscopy; OCT: optical coherence tomography; OFDI: optical frequency domain imaging; PS: polarization sensitive; TR-LIFS: time-resolved laser-induced fluorescence spectroscopy. Reproduced with permission from [15]

wave instead of light to probe the wave back-scattering properties of tissues. Laser speckle imaging rely on the temporal decorrelation of light field amplitude caused by the motion of blood particles (cells) to map out blood vessels. Near infrared imaging techniques rely on the diffuse reflectance or fluorescence of photons from deep tissues and complex reconstruction techniques.

Angioscopy is the earliest intravascular imaging device. Its ability to image the surface of the major vessel walls provides useful information to physicians about the extent of atherosclerotic plaques. However, only surface information is given, which is definitely

not enough to investigate and understand the nature of the plaque. More sophisticated techniques are needed to extract deeper information of the vessel wall, especially areas affected by the deposition of atherosclerotic plaques. Moreover, optical clearing for angioscopy must be carried out very thoroughly, versus that for EV-OCT where a considerable amount of residual blood can be tolerated.

The sound wave counterpart of OCT, ultrasound is a competing technology. Typical ultrasound imaging probes operate at about 5-10MHz [17]. In this region, the typical axial resolution of ultrasound is $\sim 200\mu\text{m}$. Typical domains of ultrasound application include cardiology, neurology and gynecology. In terms of vascular imaging though, $\sim 200\mu\text{m}$ resolution can readily distinguish large vessels like major arteries and veins. Thus ultrasound is frequently used for imaging flow in carotid and cerebral arteries or fetus cardiac action via Doppler ultrasound. Doppler ultrasound is a popular and well established flow imaging method since it has a wide dynamic range well suited for imaging flow speed of major human vessels. However, conventional array based ultrasound probes do not possess adequate resolution to image features on the arterial vessel walls, which is essential for distinguishing different types of atherosclerotic plaques.

In the specific case of imaging atherosclerotic plaques (explained in the next chapter), owing to the higher resolution mandated, intravascular ultrasound (IVUS) usually employs higher frequencies around 20-45MHz [17]. IVUS differs from traditional ultrasound probes by being integrated in an “imaging catheter”, which is equipped with a rotary and pull-back mechanism to achieve 3D azimuthal data acquisition. An exemplary probe is illustrated in Fig. 1.7. Even so the axial resolution would be on the order of $\sim 100\mu\text{m}$ [18], limited by diffraction. Although the resolution is improved and combined with the fact that ultrasound cannot be readily focused in such scenarios, IVUS gives much more inferior image quality than EV-OCT. However, with IVUS, we can see deeper into the tissue ($>5\text{mm}$), although with much deteriorated resolution. The ability of IVUS in distinguishing structure is also weak. For instance IVUS cannot depict fibrous

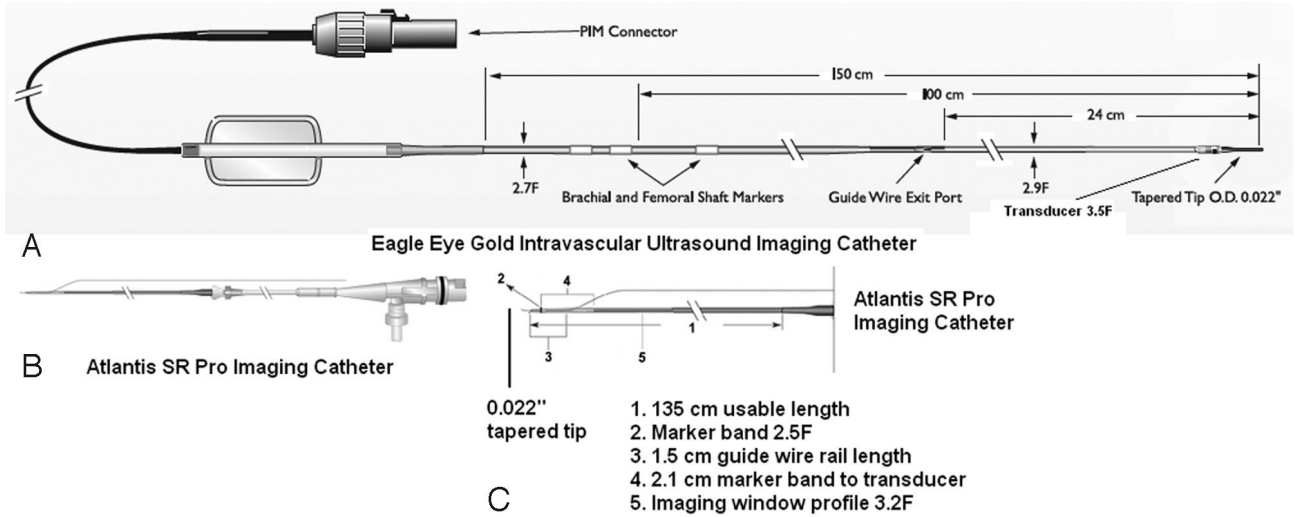


Figure 1.7: Intravascular ultrasound catheters, components, and signal-intensity characteristics. A, Eagle Eye Gold imaging catheter (20 MHz, Volcano Corporation). B and C, Atlantis SR Pro imaging catheter (40 MHz, Boston Scientific). Reproduced with permission from [17]

cap thickness like EV-OCT does.

Laser speckle imaging (LSI) is similar to OCT. However, instead of raster scanning to get cross-sectional tomograms, LSI uses a CCD camera to acquire multiple images of the whole field of view with a specific exposure time (1 to 10ms), very similar to traditional photography except that the light source is a coherent source, i.e. a laser such that speckle patterns can be formed in the acquired images. LSI maps blood vessels by either calculating the spatial or temporal decorrelation of speckle patterns of the acquired image stacks [19]. The laser speckle contrast is first obtained according to Eq. 1.3:

$$K_{S/T} = \frac{\sigma_{S/T}(T)}{\langle I \rangle} \quad (1.3)$$

where $\sigma_{S/T}$ is the spatial/temporal standard deviation of speckle intensity, T is the exposure time of the camera, I represents pixel intensity and the angled brackets indicate time averaging. Eq. 1.3 in turn leads to the following relationship between the laser

speckle contrast and the decorrelation time constant τ_c (Eq. 1.4):

$$K = \beta^{0.5} \left\{ \frac{\tau_c}{T} + \frac{\tau_c^2}{2T^2} [\exp(-\frac{2T}{\tau_c}) - 1] \right\}^{0.5} \quad (1.4)$$

where β is a parameter dependent on the detector resolution of the LSI system.

Laser speckle contrast can be calculated in two different ways. If the spatial decorrelation is calculated, spatial resolution is compromised. If temporal decorrelation is calculated, temporal resolution is compromised. The main advantages of LSI include its simple setup and relatively low cost. A recent low cost implementation has enabled LSI to be utilized in the hospital bedside setting [20]. Fig. 1.8 shows the schematics of a typical LSI setup. Moreover, quantitative perfusion measurement is much easier in LSI, since the speckle decorrelation time is well within the temporal resolution of typical LSI systems. LSI however suffers from the problem of shallow tissue penetration, making its domains of application limited to superficial vessel imaging like the cerebral cortex or skin.

Near infrared imaging, also called diffuse optical tomography (DOT), employs the diffusive nature of light. Several pairs of light sources and detectors of two different wavelengths are typically placed apart on several spatial locations of the tissue surface (e.g. scalp surface or breast surface); by mapping the distance and time of the diffusively backscattered light detected, a 3D mapping of oxy- and deoxy- hemoglobin backscattering strength can be generated. It is typically used to image cerebral cortex activity, the area where neuronal cell bodies are most densely present, with penetration depth of 5-10mm. Resolving to such penetration depths is unprecedented in optical imaging modalities, which are typically limited to a few hundred microns. However, DOT is heavily computationally dependent. Its formulation based on the radiative transfer equation requires complicated linear algebraic methods for solution but at the same time the algorithms must be efficient. In the diffusive regime, it also means that DOT resolution is

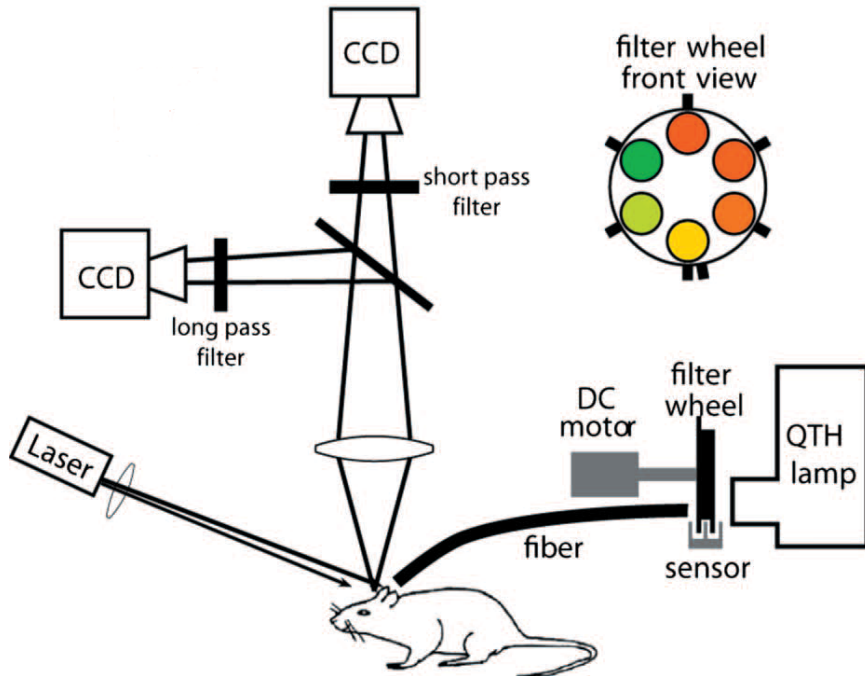


Figure 1.8: Laser speckle imaging and multispectral reflectance imaging can be performed simultaneously to image multiple hemodynamic parameters. Reproduced with permission from [21]

limited, typically to the order of centimeters. Moreover, the inverse problems are often ill-conditioned, making DOT prone to artifacts.

Fluorescence based imaging techniques have also been adapted to endovascular imaging. Confocal fluorescence, near infrared fluorescence and time resolved laser induced fluorescence spectroscopy have been reported in the endovascular catheter setting [15]. Fluorescence based techniques bear the advantage that imaging can be molecular specific, meaning that the fluorophores can be designed to target only one characteristic molecule that is unique to a tissue component in the vessel wall, such that the images acquired only map out the distribution of this specific component. However, the fluorescence signal is typically weak, making it a fundamental challenge to obtain high SNR endovascular fluorescence images. Also, this limits the ability of fluorescence based techniques to achieve high scanning speed, which is essential in endovascular settings because of the unavoidable high motion.

1.5 Current limitations in OCT and their remedies

As OCT technologies and applications continue to develop and diversify, the increasing complexity of imaging scenarios and data acquisition also demands more sophisticated ways of analysis. EV-OCT currently stands as one of the most advanced forms of OCT imaging systems, since both optical beam delivery and optical clearing present significant challenges that are non-existent in conventional bench top microscopic OCT systems.

EV-OCT has so far been cleared by the United States Food and Drug Administration (FDA) for intra-coronary imaging, however very few studies have experimented with EV-OCT on the cerebrovasculature. As such, in this thesis a set of procedures and analytical methods were devised and tested in porcine carotid arteries models, which closely mimic that of human beings. Various anatomical features and artefacts were exhibited in our experiments that serve as a foundation for future analysis of carotid EV-OCT results.

Anatomical features are only one kind of observation in vascular diseases. For some diseases, preventive measures are desirable, especially atherosclerosis. To predict the onset of atherosclerosis, one feasible way is to analyze the physiological characteristics of the vessel wall segment of concern. So far, very few studies have attempted to characterize microvessels of arterial wall using EV-OCT *in vivo*, which possesses the ideal resolution and penetration depth for such purpose. Therefore, part of the thesis will be devoted to formulating a method to detect these microvessels *in vivo* based on higher order statistics. Preliminary results in vessel detection as well as associated limitations will be presented.

To further aid the diagnosis of deeper vessel wall structures, another way is to enhance the clarity of structural EV-OCT images. Due to the relatively long optical beam delivery and miniaturized optical elements in a catheter, EV-OCT images in general are inferior to conventional microscopic OCT systems. Therefore, another part of this thesis will be devoted to the development of a noise reduction algorithm based on an iterative method to make visualization of deeper vessel wall structures more suitable for clinical diagnosis, without adding bulk optics in the already crowded catheter space.

Finally, in OCT microvasculature imaging, various methods are hampered by the SNR dependence on depth. The final part of this thesis is thus devoted to the development of a microangiographic algorithm, which relies on the information from a normalized histogram of amplitude values of each voxel, to mitigate such dependence. *In vivo* human microvascular lesions were imaged using the algorithm and the results demonstrated enhanced clarity of microvessels at deeper depths.

1.6 Thesis outline

Ch. 1 has introduced the principle of OCT and its different configurations and applications. Alternative imaging technologies have also been described. Ch. 2 details the specific applications of OCT and relates these application to the development and goals of this thesis. Ch. 3 describes the theoretical basis of all the algorithms developed in the thesis. Ch. 4 describes the results obtained in EV-OCT using the algorithms described in Ch. 3. Ch. 5 describes imaging results of *in vivo* human skin vasculature rendered using a depth-enhanced method. Ch. 6 discusses the impact and conclude the thesis, and future work will also be suggested.

Chapter 2

OCT Anatomical and Vascular Imaging

2.1 Vascular imaging and its applications

As mentioned in the last chapter, the major advantage of OCT is its deep penetration into biological tissues, which is otherwise unachievable via conventional optical methods. Moreover, traditional methods rely heavily on the Rayleigh range of the focusing lens for “optical sectioning”. Even for laser scanning confocal microscopy or two-photon microscopy, high resolution optical sectioning is achieved by narrowing of the pinhole or tighter focusing for non-linear absorption, respectively. These methods either do not give sufficient axial resolution or severely limit the SNR and speed of the data acquired. With coherence gating of OCT, excellent optical sectioning can be achieved without compromising SNR, speed or tissue viability. Thus, OCT is specifically good at deciphering layered structures of biological tissues, which is why OCT is particularly popular in ophthalmology and dermatology which are dominated by layered structures.

As aforementioned, one of the main application of OCT is microvascular imaging. With the emergence of Doppler OCT, arterioles and venules can be precisely mapped out

with blood flow velocity. However, many diseases are associated with not only arterioles and venules, but more importantly also angiogenesis of capillaries. Neoangiogenesis is the most striking feature of many tumors, wound healing processes and genetic vascular diseases, etc. As such, methods capable of mapping smaller vessels are being developed.

Doppler OCT belongs to the class of phase based vascular imaging methods. For such methods to work, substantial imaging beam overlap between A-scans is required in order to deduce the phase shift induced by the scattering particles movement. The phase shift between A-scans can be found, for example, by the Kasai Autocorrelation (Eq. 2.1) [22, 23]:

$$\Delta\phi = \tan^{-1} \left\{ \frac{\frac{1}{M(N-1)} \sum_{m=1}^M \sum_{n=1}^{N-1} (I_{m,n+1}Q_{m,n} - Q_{m,n+1}I_{m,n})}{\frac{1}{M(N-1)} \sum_{m=1}^M \sum_{n=1}^{N-1} (Q_{m,n+1}Q_{m,n} + I_{m,n+1}I_{m,n})} \right\} \quad (2.1)$$

where M and N are the window size of the phase shift calculation and I and Q are the real and imaginary parts of the complex OCT signal, respectively. Thus, a large number of A-scans are required for each B-frame. Since a large number of B-frames are required to construct 3D vascular map projections, this often results in huge volumetric datasets with Doppler OCT. Moreover, phase noise is directly related to the scan speed of the light source. Thus higher laser sweep rate would actually generate higher phase noise. Such property actually goes against the current state of the art high speed OCT development, since in order to get Doppler signals with low noise, the laser swept rate must be kept low. In addition, aliasing occurrence directly correlates to the laser sweep rate, limiting the dynamic range of Doppler OCT.

To limit motion and reduce patient discomfort, current OCT systems usually employ light sources that allow A-scan rates of around 50kHz. The phase noise in this scenario usually masks the Doppler signal from micro-capillaries, since blood flow velocity in capillaries is typically slow and there is an absolute minimum phase that Doppler OCT can detect above the noise level. Therefore, to image these microvessels, speckle based

vascular imaging must be used. Speckle based imaging does not require a large number of A-scans in a B-frame. In general this class of method only requires a moderate number of B-frames, which is essential for volumetric imaging 3D renderings.

The first OCT speckle based vascular imaging method was demonstrated by Mariampillai et al., termed “Speckle variance optical coherence tomography” [24, 25]. To obtain angiographic data, a stack of B-frames are acquired as volumetric data. At each calculation, ~ 4 frames are taken usually at each voxel, the variance of the amplitude values from these ~ 4 frames is then calculated. Since flowing blood actually induces a strong modulation in speckle amplitude due to the fact that there is a small time lapse between successive B-frames, the variance signal of micro-vessel areas would be large. The speckle variance signal is calculated according to Eq. 2.2:

$$\sigma^2(m, x, y) = \frac{1}{N} \sum_{n=m}^{m+N-1} [I(n, x, y) - \mu_0(m, N, x, y)]^2 \quad (2.2)$$

where σ is the standard deviation at pixel (x, y) , m is the m -th frame of the speckle variance signal, N is the number of frames used to compute the speckle variance, I is the intensity of each frame at pixel (x, y) and μ_0 is the mean between N frames at pixel (x, y) . After each calculation, the generated speckle variance B-frames are stacked together and a projection image is generated for three dimensional evaluation of microvascular structures.

There are 3 main areas of application of OCT microvascular imaging: disease diagnosis, therapeutic monitoring and functional imaging of the central nervous system.

2.2 OCT Imaging for Disease Diagnosis

Various diseases involve a condition known as angiogenesis. Angiogenesis is the formation of new microvessels, usually capillaries in tissue lesion sites. One class of diseases often show pronounced level of angiogenesis: cancers. While wholebody imaging modalities

such as computed tomography and magnetic resonance imaging are capable of obtaining angiographic information, they do not possess adequate resolution to see down to the level of arterioles and even capillaries. Even Doppler ultrasound can only depict major arteries and veins. On the other hand, high resolution modalities such as confocal laser scanning microscopy and structured illumination microscopy typically have long data acquisition time and are very susceptible to noise and motion. As such, these microscopy techniques are not suitable for *in vivo* human imaging.

In various studies, cancer angiogenesis can be clearly depicted in OCT microangiography [25, 26]. As aforementioned, structural images cannot precisely identify tissue types, even though tumor morphologies and speckle properties would be different from normal tissues, precise boundaries cannot be reliably identified. However, since cancer tissues are hypoxic and they must be proximal to microvessels in order to obtain nutrients they demand, by mapping the microvascular network in the tumor area, clinicians can better differentiate the tumor margins than looking at structural renderings alone [27].

The first and foremost area of OCT microvascular diagnosis is ophthalmology. The human retina consists of multiple layers that comprise of different types of cells and tissues. OCT is therefore ideal for optical sectioning of these different layers. To illustrate the excellent ability of optical sectioning by OCT, Fig. 2.1 shows an OCT image of the macula with different layers labeled. Numerous studies have used OCT microangiography to image retinal vasculature for various eye abnormalities [28], for example, age related macular degeneration [29], glaucoma [30], diabetic retinopathy [31], and melanoma [32] (a type of cancer in the eye). OCT can not only decipher retinal conditions. The penetration of OCT also allows physicians to diagnose deep down to the level of the choroid, which is unprecedented before the invention of OCT. The choroid is the layer of the eyeball in which a tremendous amount of blood vessels exist. Recently, it has been demonstrated that various diseases can correlate to changes in the choriocapillaris (choroidal vasculature) depicted in OCT microangiographic images. Owing to the fenestrated nature of

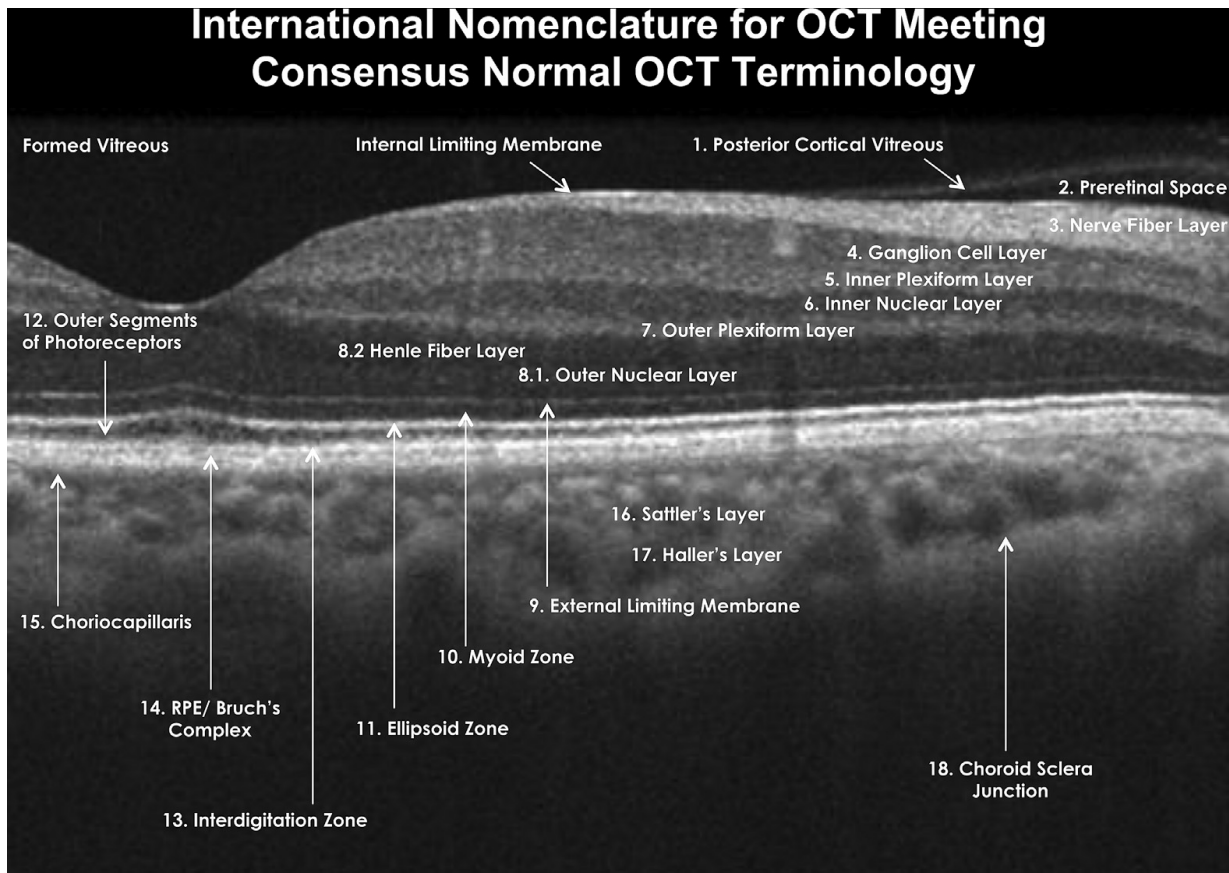


Figure 2.1: Exemplary OCT image of the retina at the macula. Reproduced with permission from [34]

the choriocapillaris, only the recent advancement of high speed OCT systems can enable more reliable microangiography than the conventional standard fluorescein angiography which suffers from fluorophore leakage from the vessels [33]. Commercial ophthalmologic OCT can typically reach A-scan rates of more than 50kHz, making the scan time of one data set to be around 5 seconds. Such high scan speed has ensured minimal motion from the involuntary eye movement of the patients as well as minimized vessel leakage induced speckle decorrelation, allowing choroidal vasculature to be integrally captured in the OCT projection images [33].

Not long after the discoveries in ophthalmic OCT imaging, research studies have since brought OCT into other application domains.

Dermatology is another area in where OCT has found ample applications. Similar

to the retina, skin consists of many layers of tissue structures. These structures are mainly divided into the epidermis, the dermis and subcutaneous tissues. In healthy skin, the epidermis comprises mostly of connective tissues and dead cells, serving as a major barrier against pathogens. The dermis consists of more living cells and blood vessels. Subcutaneous tissues include fat, more arterioles and venules and nerves. OCT can diagnose and monitor the progress of skin tumors and inflammatory disease [35], etc. with anatomical imaging alone. Many commercial OCT systems have been specifically developed for skin imaging. Since then, dermatologic OCT has been moving towards microvascular imaging or even photothermal OCT imaging [36].

Gastroenterology has also found considerable interest in using OCT in the diagnosis of intestinal wall abnormalities [37]. Similar to EV-OCT, OCT gastrointestinal (GI) tract imaging is usually carried out with a rotary probe with pullback mechanism integrated with GI endoscopes. Diseases such as Barrett's esophagus, squamous cell cancer and adenocarcinoma have been imaged extensively with OCT endoscopes in various studies [12, 38].

Lastly, OCT has recently started moving towards optical biopsy applications. Biopsy in the GI tract [39], breast [40, 41] and brain commonly using “needle probe” (OCT imaging probe integrated within thin biopsy needles) has so far been reported. More biopsy applications are expected to be found integrated with OCT technology.

2.3 OCT for Therapeutic Monitoring

OCT can also be used in monitoring of various therapeutic treatments. Photodynamic therapy is an emerging biophotonic method for the treatment of cancerous lesions. It involves the injection of photosensitizers into the cancerous lesions. A diode laser is then commonly used to illuminate the lesion area when the photosensitizer is thoroughly absorbed by the lesion. Once the photosensitizer is activated, vascular shut down would

initiate over the course of several minutes, thereby depleting oxygen supply to the cancerous tissues. Cancerous tissues are hypoxic tissues, meaning that their cells are always short of oxygen, and dense angiogenic microvessels networks are needed to supply them. It is therefore imperative to monitor the extent of their vascular shutdown, so as to confirm the area where treatments are expected to be effective and decide whether or not additional therapy is needed by PDT or by other means. OCT has been previously utilized for *in vivo* PDT monitoring of macular degeneration [42], skin cancer lesions [43], prostate gland [6] and esophagus [44].

Other than PDT monitoring, OCT has also been used for monitoring tissue changes during laser thermal therapy [45] and open knee surgery [46].

2.4 OCT for Functional Imaging

In MRI studies, functional imaging can be achieved by exploiting the fact that neuronal activation requires more oxygen and therefore more blood supply. By mapping out the blood oxygenation level in the brain, MRI can localize the activity area of the brain corresponding to the stimulant or the motor function concerned.

OCT can also be used for functional imaging, particularly for the cerebral cortex in the brain. The simplest way to localize activity area in small animals is microvascular imaging. Although high speed quantitative blood flow imaging is very difficult to achieve in OCT, and blood oxygenation information cannot be easily obtained in OCT, to localize activity areas, vessel dilation is nonetheless the most obvious feature of neuronal activation. When neurons become activated, a large amount of energy and therefore oxygen is needed at the foci. As such, vasodilation occurs at the local vicinity. Thus by mapping the vascular map precisely before and after stimulant activation, the activated areas can be directly mapped out by comparing the microvessel sizes at each location.

Various studies have attempted to image vessel size changes during neuronal acti-

vation [47, 48]. Doppler OCT was also attempted to be used for cerebral hyperemia imaging [49]. This yielded quantitative flow information in addition to vessel size and density changes, but at the expense of lower axial scan rate and more A-lines per image, thus making three dimensional evaluation more challenging.

2.5 Atherosclerosis

Apart from cancers, stroke is another major cause of fatality worldwide. About 20%–30% of cerebral infarction is related to carotid atherosclerosis or stenosis [50]. Ultrasound, MRI and CT imaging have in the past been utilized to diagnose plaque characteristics in order to evaluate the progress of plaque formation and make a better decision on plaque treatment.

Atherosclerosis is a disease where atheroma is deposited within the vessel wall. The atheroma is composed of variable amounts of macrophages, lipids, fibrous tissue and calcium. Depending on the composition of the lesion, the American Heart Association has classified atherosclerosis from I to VI with V and VI being considered to be high-risk lesions [51–53]. Carotid artery atherosclerosis is an important cause of ischemic stroke [54, 55]. Patients with symptomatic high grade carotid stenosis benefit from revascularization [56, 57]. Treatment modalities include surgical intervention, such as the resection of diseased tissue called carotid endarterectomy, or endovascular treatment such as carotid angioplasty and stenting (CAS) [58]. Fig. 2.2 lists the different types of atherosclerotic plaques.

The coronary artery has been successfully imaged by OCT in various studies [59]. Carotid arteries, however, having large diameters and high blood flow rate, are not easily imaged with conventional TD-OCT systems owing to their slow imaging speed. There were only a handful of studies attempting to image the carotid artery *in vivo* [60, 61]. Recently, a new state-of-the-art OCT system (Lightlab Imaging, St. Jude Medical Inc.,

Histologic Classification of Atherosclerosis		Characteristics
Initial lesions		
Type I		Increase in the number of macrophages and appearance of foam cells distributed at random, present in 45% of children younger than 8 months of age
Type II (fatty streak)		First visible lesion; layers of foam cells and drops of fat inside the smooth muscle cells and in the extracellular space; minute lipid particles with round and heterogeneous aspect, present in 65% of teenagers
Type IIa		Intimal thickening, lesions tending to progress
Type IIb		Intimal tunica intima thinner and few smooth muscle cells
Intermediary lesions		
Type III		Lesions similar to those of type II, with extracellular lipid collections
Advanced lesions		
Type IV (atheroma)		Confluence of lipid collections of type II lesions creates an extracellular dense accumulation of fat in a well-defined area of the tunica intima, the lipid nucleus; no marked fibrous tissue or presence of complications such as flaws on the surface of the plaque or thrombosis; between lipid nucleus and endothelial surface, there is the extracellular matrix rich in proteoglycans and cells, such as lymphocytes, macrophages, and foam cells; these are not usually associated with the lumen stenosis of the vessel; on the contrary, there may be an increase in diameter when measured from the adventitia
Type V		When fibrous capsule develops, it usually causes lumen stenosis and can have fissures, hematomas, or thrombosis
Type Va (fibroatheroma)		Fibrous tissue containing lipid nucleus; new lipid nuclei can appear in different locations and planes, creating asymmetric lesion
Type Vb		Calcification of fibrous nucleus or of other parts of lesion
Type Vc		Absence or minimal presence of lipid nucleus
Complicated lesions		
Type VI		Usually type IV or V lesions presenting rupture on surface, hematoma or hemorrhage, and also thrombus.
Type VIa		Surface rupture
Type VIb		Hematoma or hemorrhage
Type VIc		Thrombosis
Type VIabc		Rupture, hemorrhage, and thrombosis

Figure 2.2: Phases of the formation of atherosclerotic plaque according to the American Heart Association, reproduced with permission from [50]

St. Paul, Minnesota, USA) has been cleared by the FDA for clinical use in coronary imaging. With this high speed OCT system, a pilot study has been conducted on human to image stented carotid arteries after their carotid artery stenting (CAS) procedures [62]. Images obtained could clearly show the vessel wall anatomy and could delineate the degree of stent apposition to the vessel wall, plaque prolapse through the stent tines and the presence of a dissection flap (i.e., a tear in one of the layers of the vessel wall) or mural thrombus. These are promising results. At the time of this work, however, no animal studies on OCT imaging of carotid arteries using a state-of-the-art high speed OCT system have been conducted and experimental details have not been fully optimized. In the study described above, un-occluded saline or contrast injection was quickly ruled out because of several unsuccessful attempts and the images were obtained using two occlusion balloons in the common and external carotid arteries. Our study reported in this thesis therefore, was in part to define the blood clearing technique to improve OCT imaging [63]. If a proper blood flushing protocol is not developed there are side effects such as stroke, aneurysm, and poor image quality.

2.6 Current capabilities of EV-OCT

EV-OCT is a very powerful tool in interventional cardiology because of its ability to detect the following atherosclerotic plaque features [64].

1. Blood appears as a region of high backscattering and huge attenuation below the surface layer of that region.
2. Calcification is depicted as a large area of signal-poor or heterogeneous region with sharply delineated borders (Fig. 2.3).
3. Lipid pools are represented in EV-OCT as signal-poor regions with poorly defined or diffuse borders (Fig. 2.3). Lipid pools can histopathologically be found as necrotic cores (dead cells) or a region with intimal thickening that contains extracellular lipid of

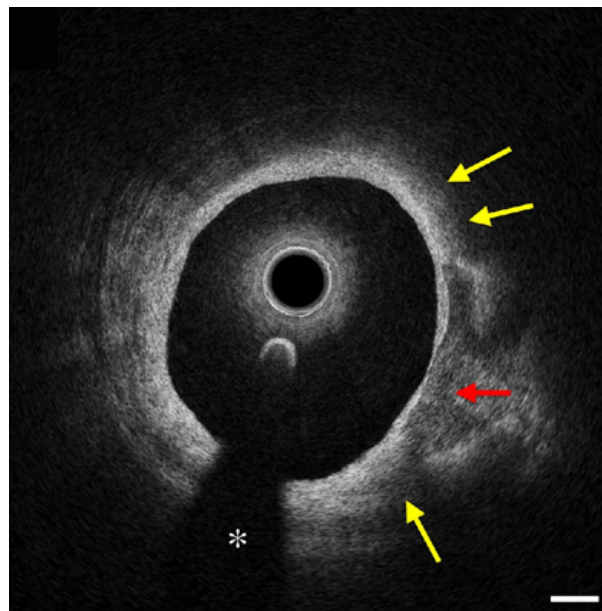


Figure 2.3: Fibrocalcific plaque (red arrow) with lipid pools (yellow arrows), reproduced with permission from [64]. * represents the shadowing artifact caused by the guidewire. Scale bar represents $500\mu\text{m}$.

proteoglycans.

4. Fibrous caps are a signal-rich tissue layer overlying a signal-poor region. Thin capped fibroatheroma is defined as necrotic core with an overlying fibrous cap with the minimum thickness less than a certain value.
5. Macrophage accumulations can be seen in EV-OCT as a signal-rich and distinct region and less linear than the external elastic membrane.
6. Intimal vasculation are hypothesized to be distinct voids that are continuous over several frames.
7. Cholesterol crystals are delineated as thin, linear regions of high intensity in the vicinity of fibrous caps or necrotic cores.
8. Red blood cell-rich thrombus is seen in EV-OCT as high intensity regions with high attenuation and white platelet-rich thrombus appears with lower intensity and is more homogeneous (Fig. 2.4).

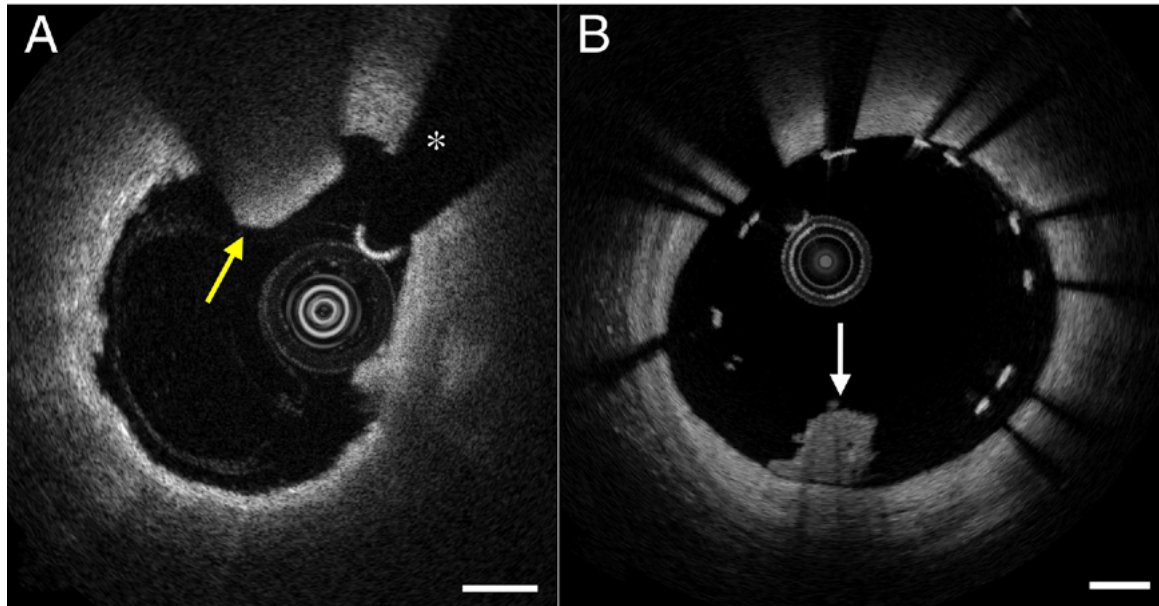


Figure 2.4: Red thrombus (yellow arrow in A) and white thrombus (white arrow in B), reproduced with permission from [64]. Scale bars represent $500\mu\text{m}$.

2.7 Hereditary vascular diseases

Hereditary diseases are passed from parents to children, and possibly through many generations. Diseases involving blood vessels, vascular diseases, can also be hereditary.

The known hereditary diseases include Hereditary Hemorrhagic Telangiectasia (HHT, also known as Osler-Weber-Rendu syndrome), peripheral artery disease (PAD) and Moyamoya disease.

PAD tends to increase the tendency of atherosclerosis of the patients. EV-OCT has been used to evaluate the diseased arteries of PAD patients [65, 66].

Moyamoya disease involves the thickening of blood vessel walls near the brain [67]. Cerebrovascular imaging using OCT is just at its infancy which will be described in subsequent chapters. To our knowledge, there is not yet any attempt to evaluate this disease using EV-OCT.

HHT is a disease characterized by arterial venous malformations, which are blood vessel networks that directly connect arteries to veins without passing through a capillary bed. Part of the thesis involves the detection of these malformed microvascular networks,

which are related to angiogenesis of atherosclerotic plaques. Details will be discussed in Ch. 5.

The field of hereditary vascular diseases are not well understood partly because of the resources that need to be devoted to understand them versus the actual number of patients. Even though people suffering from these diseases are far fewer than those suffering from cancer or diabetes, adequate treatment opportunities should still be given to these patients. Traditional whole body imaging modalities may not possess the resolution needed to image the vessel irregularities, and they can be costly too. Due to the versatility of OCT in that it can either be in a microscopic configuration or in a catheter configuration and with its penetration depth and high resolution, it presents an excellent opportunity for studying these rare genetic vascular disorders.

2.8 Conclusion to Introduction: Motivation of the Thesis

To date, EV-OCT has been extensively proven to be clinically important and valuable for the diagnosis of cardiac atherosclerosis. Its ability to differentiate fibroid tissues, calcification and lipid deposits from each other has provided cardiovascular surgeons and researchers with unique insights regarding the nature and progression of atherosclerotic plaques. In our research, we seek to extend the utility of EV-OCT to the cerebrovascular domain. Fig. 2.5 shows a gross depiction of the cerebrovasculature of concern in this thesis.

The first conduit to the cerebrovasculature is the common carotid artery (CCA) which is directly connected to the aortic arch. At the end of the CCA connects the internal and external carotid arteries (ICA and ECA). From the ICA to the cerebral artery spawns the complete cerebrovasculature that supply oxygen and nutrients to the brain. For human adults, the CCA is about 6mm in diameter and the ICA is about 4mm in diameter.

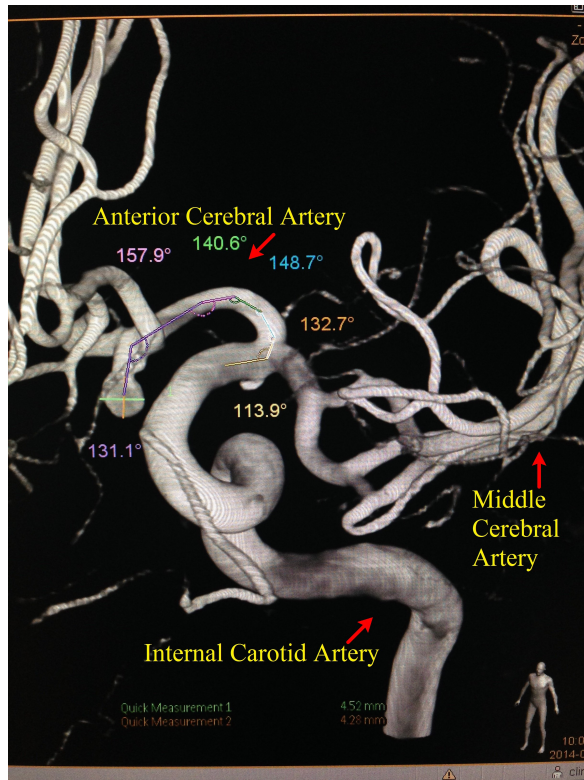


Figure 2.5: Cerebrovasculature in the skull base region.

Thus, their sizes are much larger than the coronary artery which is typically about 2mm in diameter. This poses a challenge for EV-OCT imaging for the following reasons: The much larger diameter means a longer focus of the imaging catheter for optimal imaging quality (i.e. optimal lateral resolution); in addition, the much thicker tissue structure also mandate a longer Rayleigh range of the imaging catheter. Unfortunately, due to the limited size of typical cerebrovascular catheters, these aspects cannot be fulfilled easily via resign of the catheter.

From the cost effectiveness of healthcare, consider the net cost of performing an endovascular imaging session of $\sim \$2000$. Adding more sophisticated optical components with very marginal benefits does not justify the steeply increasing cost. Such deficiencies, therefore, can and should be mitigated by digital means.

Digital image processing employed in the medical imaging scenario poses several advantages. First, computer hardware required to carry out digital image processing is

relatively much cheaper than what could be achieved with additional optical components. Further, these components are not readily integrable into catheter settings. Second, digital image processing makes the most efficient use of all the information in the data available, and thereby makes more effective use of resources. Third, digital imaging methods can be re-used across different OCT platforms with only slight adjustment and without complicated optical alignments. And last but not least, digital image processing is fundamentally inseparable from any imaging modalities. Only the extent varies, and modern medical imaging modalities often utilize digital image processing as extensively as possible to facilitate disease diagnosis as well as minimize doctors' interpretation time.

In this thesis, as aforementioned in Ch. 1, a set of digital methods are developed for OCT vascular imaging both in the EV configuration and in the raster scanning configuration. They serve to improve doctors' interpretation on OCT data, and even help them gain more insight to the physiological status of tissues via functional means. It is my ultimate hope in this thesis to improve the overall diagnostic efficiency and fundamental understandings on different kinds of vascular diseases, such as atherosclerosis and hereditary hemorrhagic telangiectasia.

Chapter 3

Theoretical Basis and Algorithm Development

3.1 Candidate Contribution

The theoretical basics and implementation of the two algorithms described at the end of the chapter are devised by the candidate.

3.2 Image Formation

The most basic form of image formation in an optical imaging system can be described by Eq. 3.1:

$$\mathbf{y} = \mathbf{P} \otimes \mathbf{x} \quad (3.1)$$

where \mathbf{y} is the observed image, \mathbf{x} is the supposed original sample structure and \mathbf{P} is the point spread function of the imaging system. \otimes denotes a convolution operation. This constitutes an inverse problem in which what we have is \mathbf{y} , the acquired image data, and we would like to obtain \mathbf{x} which is the sample structure, with the information from the PSF of the imaging system. The following formulation follows that of [68] for example.

Since images can be vectorized ($x = \text{vec}(\mathbf{x})$) and solved with linear algebraic methods, Equation 3.1 can be rewritten directly as matrix operations:

$$y = \mathbf{P}x \quad (3.2)$$

Since \mathbf{P} is not necessarily square and invertible, for this simple problem, the solution to this is (Eq. 3.3):

$$x = (\mathbf{P}^\dagger \mathbf{P})^{-1} \mathbf{P}^\dagger y \quad (3.3)$$

where \mathbf{P}^\dagger represents the adjoint of \mathbf{P} .

With speckle noise and additive Gaussian noise, however, the problem becomes more complicated (3.4):

$$y = e\mathbf{P}x + n \quad (3.4)$$

where e represents multiplicative noise such as speckle and n represents additive noise. If Eq. 3.4 is solved as in Eq. 3.3, a problem arises:

$$\hat{x} = (\mathbf{P}^\dagger \mathbf{P})^{-1} \mathbf{P}^\dagger (e\mathbf{P}x + n) = (\mathbf{P}^\dagger \mathbf{P})^{-1} \mathbf{P}^\dagger e\mathbf{P}x + (\mathbf{P}^\dagger \mathbf{P})^{-1} \mathbf{P}^\dagger n \quad (3.5)$$

As a result, the noises (whether additive or multiplicative) would be amplified and the original image cannot be restored. Therefore, regularization methods are often used to circumvent the problem of noises, processes that introduce additional constraints in order to solve ill-posed problems such as image restoration. Regularization problems can be solved by iterative methods. Details of the methods used in this study are described in the following sections.

3.3 Basic Common Image Processing Techniques

Basic image processing methods are given below:

Thresholding: Every pixel with intensity lower than a specific value will be set to 0. The purpose of thresholding is to get rid of constant background intensities.

Mean filtering: Every pixel is recomputed as the average of the nearby neighborhood of $N \times N$ pixels and itself. Mean filtering is a low pass filtering operation and thus significant blurring would occur as the kernel size gets larger.

Median filtering: For a neighborhood of $N \times N$ pixels, pixel values are sorted and the median value is taken as the pixel value. Median filtering is a low pass filtering operation and thus significant blurring would occur as the kernel size gets larger. It belongs to the class of order filters.

Difference filtering: The difference is taken between adjacent pixels and the average is taken. This is equivalent to the first derivative. This technique is mainly for edge detection.

Second derivative filtering: The second order difference is taken between adjacent pixels. This is mainly for smooth edge detection.

The Laplace operator is the second derivative filtering in multiple dimensions.

3.4 Information Divergence

Divergence is a measure of the “distance” of two statistical distributions. In the context of this thesis, the distribution means the collection of intensity values of an image. In terms of image restoration, by minimizing the divergence between two images implies rendering them as similar as possible. β -divergence was used for blind source separation [69] (separation of two sources of signal mixed in a non-trivial way) and is defined as [70]:

$$d_\beta(x, u) = \frac{1}{\beta(\beta - 1)}[x^\beta + (\beta - 1)u^\beta - \beta xu^{\beta-1}] \quad (3.6)$$

where x equals, in our case, the desired restored image, and u denotes a reference image which is excessively filtered. In this equation, β is a scalar parameter to be chosen. The

β -divergence has the important property, where only when $x = u$ would the divergence measure vanish. When $\beta = 0$, the divergence measure converges to:

$$d_{\beta=0}(x, u) = -\log \frac{x}{u} + \frac{x}{u} - 1 \quad (3.7)$$

which is known as the Itakura-Saito divergence. And when $\beta = 1$, the divergence measure converges to:

$$d_{\beta=1}(x, u) = x \log \frac{x}{u} - x + u \quad (3.8)$$

which is known as the Kullback-Leibler divergence or I-divergence. The I-divergence has been used in the past for astronomical image restoration [71]. Finally when $\beta = 2$, the β -divergence is reduced to the Euclidean distance.

From the above equations, it is clear that the β -divergence is a generalized class of divergence. To see why generalization is needed, one obvious advantage is that it does not subject the image restoration process to error by generating undefined pixels since there are no reciprocal or logarithmic terms of x or u for $\beta \neq 0, 1$. In numeric iterations, when division-by-zero or logarithm-of-negative is encountered, the pixel incurred would typically be designated as *NaN* (Not a Number) and iteration for that pixel would become a dead-end and visualized as intensity equals to 0. In another study, the β -divergence measure was also shown to be robust against outliers [69], which is an advantage because outliers would typically severely affect the image contrast.

3.5 Speckle, Origin and Characteristics in OCT

Optical scientists discovered a strange phenomena when they worked with coherent light illuminations. They observed a grainy pattern from the reflections of laser coherent illuminations on many sample material surfaces [72]. These patterns were not due to any fault in the optical components in the optical beam path. These patterns were later

confirmed to be the result of random interference of back scattered photons reflected from sample surfaces (Specular reflection) or volumes (Diffuse reflection).

In the realm of optical imaging, speckle is an inherent characteristic of any coherent modality, also known as coherent imaging. Coherent imaging modalities refer to imaging methods which carry both amplitude and phase information. The interference nature of speckle fields implies the importance of the phase information and therefore coherent imaging modalities. OCT is a coherent imaging modality because the complex amplitude tomographic information implicitly contains phase information. Recall that each A-scan data is collected by interference of light in the sample arm and reference arm, the resultant interference pattern can be viewed in another way as the phase differences between the sample arm light and reference arm light.

The resultant speckle field formed in a coherent imaging modality like OCT cannot be deterministically calculated owing to the random nature of tissue structure, molecular orientations and multiple scattering, etc. Instead, speckle characteristics in speckle fields can be described by using statistical distributions. The light amplitude or phase backscattered from a particular spatial location can be described as a random walk consisting of individual phasors, vectors defined by both amplitude and phase. The overall summation of these phasors to infinity in each OCT image voxel results in the statistical distributions of particular scenarios, described in the next section.

3.6 Motion in OCT and its Relationship with OCT Speckle

Current state-of-the-art OCT technologies enable A-scan rates of tens of kHz . At this scan rate, most biological tissues can be regarded as static tissues. If multiple B-scans are acquired over time at the same region of interest (ROI), not only does the shape of the static tissues remains constant, their speckle pattern also remains the same.

At this scan speed ($\sim 50\text{kHz}$), there is one type of observable non-static tissue: blood. Blood consists of blood cells and platelets. Typical blood cells travel with a velocity on the order of $\mu\text{m/s}$. Compared to the typical OCT frame rate of ~ 100 fps and spot size of $\sim 20\mu\text{m}$, such translational motion causes the speckle to be rapidly modulated.

Owing to the fact that the OCT signal is detected by balanced detection and then Fourier transformed, the resultant statistical distribution of detected amplitude from completely randomly flowing scatterers is the Rayleigh distribution (Eq. 3.9) [72], since the resultant amplitude distribution from two Gaussian quadratures is Rayleigh in nature. This includes voxels falling within the vicinity of major arterioles and venules.

$$p_{Rayleigh}(A) = \frac{A}{\sigma^2} \exp\left(-\frac{A^2}{2\sigma^2}\right) \quad (3.9)$$

where A is the speckle amplitude and σ is the standard deviation of the underlying quadratures. For voxels occupied partially by static tissues and micro-capillaries, the amplitude distribution would be Rician, which is just a generalization of the Rayleigh distribution with the introduction of the non-centrality parameter ν , as in Eq. 3.10:

$$p_{Rician}(A) = \frac{A}{\sigma^2} \exp\left(-\frac{A^2 + \nu^2}{2\sigma^2}\right) I_0\left(\frac{A\nu}{\sigma^2}\right) \quad (3.10)$$

where ν is the non-centrality parameter representing the portion of static tissue and I_0 is the 0^{th} order modified Bessel function of the first kind. Static tissues are in general corrupted by additive Gaussian noise. With a high specular reflection component and thus large ν , the corresponding amplitude statistics would converge from Rician to Gaussian distributions (as $\nu \gg \sigma$) in Eq. 3.11 [73]:

$$p_{Gaussian}(A) = \frac{1}{\sigma\sqrt{2\pi}} \exp\left(-\frac{A - (\sqrt{\nu^2 + \sigma^2})^2}{2\sigma^2}\right) \quad (3.11)$$

3.7 Application I: Detection of Vasa Vasorum using Higher Order Statistics

Numerous studies have demonstrated the ability of OCT to distinguish the intima, media and adventitia layers of normal coronary arteries. EV-OCT is also able to image intra coronary atherosclerotic plaques and can identify multiple tissue structures such as fibrous cap, intra-plaque lipid deposition, and intra-plaque calcification nodules. In addition, various research studies have reported the imaging of intra-plaque neovascularization [74, 75]. Imaging of these features is important in determining the stage and progress of atherosclerosis and their mapping techniques can readily be extended to the carotid artery, in which the rupture of vulnerable plaques can lead to thrombosis and consequently stroke occurrence. Moreover, OCT has been shown to image coronary stenting and evaluate the occurrence of improper stent apposition, thrombosis and restenosis [76, 77].

However, all the studies have only been devoted to imaging the inner layers of the arteries close to the lumen. Different layers have been distinguished in normal arteries including the intima, the media, the external elastic lamina and the adventitia [59, 60]. To our knowledge, no attempts have yet been made to characterize finer features that are present in the arterial wall as detected by EV-OCT. In particular, there are various morphological features present in the adventitia, albeit with a significantly lower intensity due to the intrinsic optical absorption and scattering properties of tissue. Furthermore, the thicker vessel wall and larger diameter of the carotid artery add to the challenge of EV-OCT due to limited penetration depth and reduced lateral resolution.

One particular anatomical structure of considerable interest in the adventitia is the vasa vasorum (Fig. 3.1), the blood vessels of blood vessels. A number of physiological studies have elucidated the importance of the vasa vasorum and their roles in the supply of nutrients and the removal of waste from endothelial cells and tissues, in their blockage

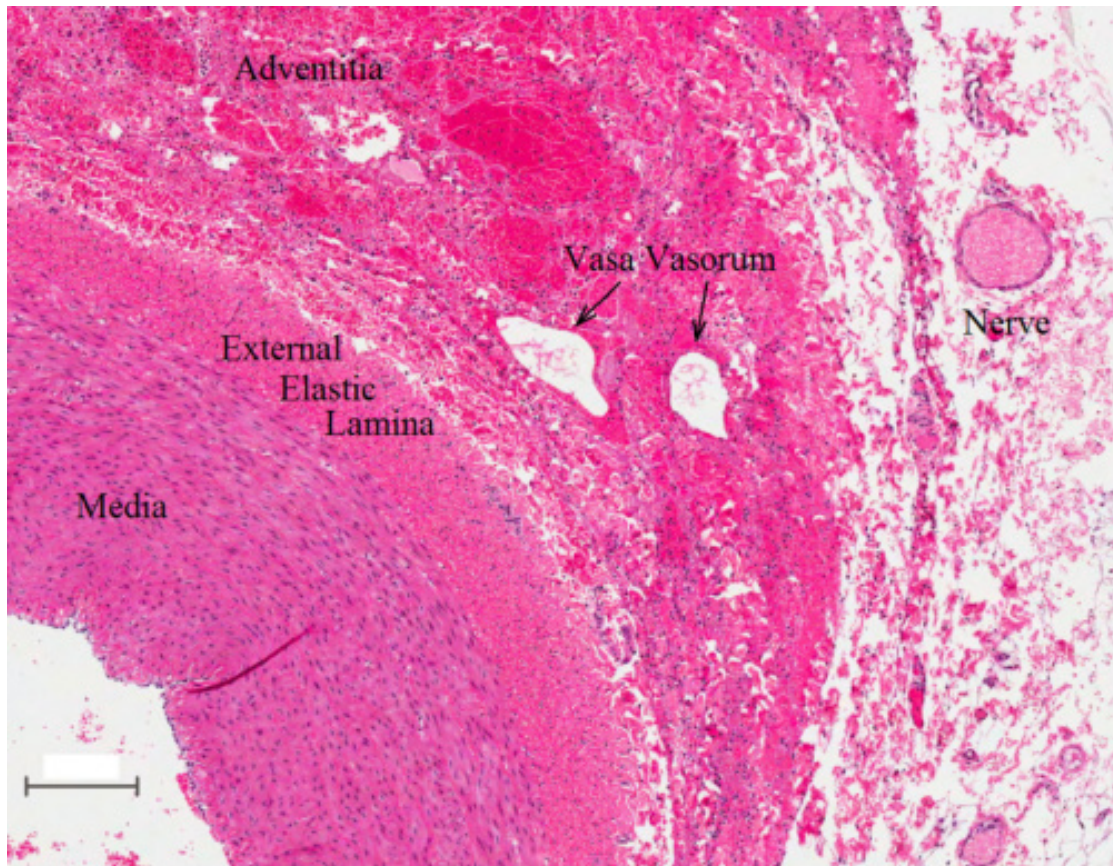


Figure 3.1: H&E staining of porcine carotid artery. The black arrows point to vasa vasorum at the adventitia. Scale bar represents $200\mu\text{m}$.

or damage leading to atherosclerotic plaque formation and in their reduction or increase in number in correlation to the vulnerability of vessel walls [78] or the degree of occlusion of the artery [79]. Additional studies have also imaged the vasa vasorum of the aorta, coronary artery and carotid artery of humans and pigs using micro-computed tomography (Micro-CT) [78]. However, most of these studies to date have used either *ex vivo* cadaveric vessel samples or *in situ* euthanized animals to obtain the Micro-CT vascular maps, where the technique encounters significant difficulty in obtaining *in vivo* patient data. Intravascular ultrasound (IVUS) has also been shown to map out areas perfused by vasa vasorum but it relies on the injection of micro-bubble contrast agent [80]. Moreover, IVUS does not possess sufficient resolution to map out individual vasa vasorum clearly. Another novel imaging modality, namely photoacoustic tomography (PAT), has been used to map out microvasculature [81,82]. PAT works by directing laser pulses towards target tissues, the absorbed laser light is then converted to phonons, in turn being emitted as ultrasound, detected by ultrasonic transducers. Different configurations of PAT differ significantly in both time and spatial resolution. For endoscopic configuration, PAT has a spatial resolution in the range of $47\text{-}65\mu\text{m}$ and a temporal resolution of $\sim 2.6\text{Hz}$ [81]. Thus, in this and similar configurations, with the present resolution, PAT may still be insufficient for vasa vasorum detection. When the future development of PAT allows a resolution and temporal measurements similar to that of EV-OCT, we believe the same algorithm could then be applied to PAT images. Therefore, there exists an unique opportunity for EV-OCT to offer the combination of *in vivo* imaging with a resolution suitable to clearly identify this important vascular structure. Initial results have been presented where several morphological features of the carotid artery were visible in the adventitial layer via EV-OCT [62]. However, few studies have investigated vascular components of the adventitial layer as it can be difficult to clearly identify the presence of the vasa vasorum due to the high motion artifacts associated with carotid imaging. Therefore, in this pilot study, EV-OCT images of *in vivo* porcine carotid arteries were imaged and

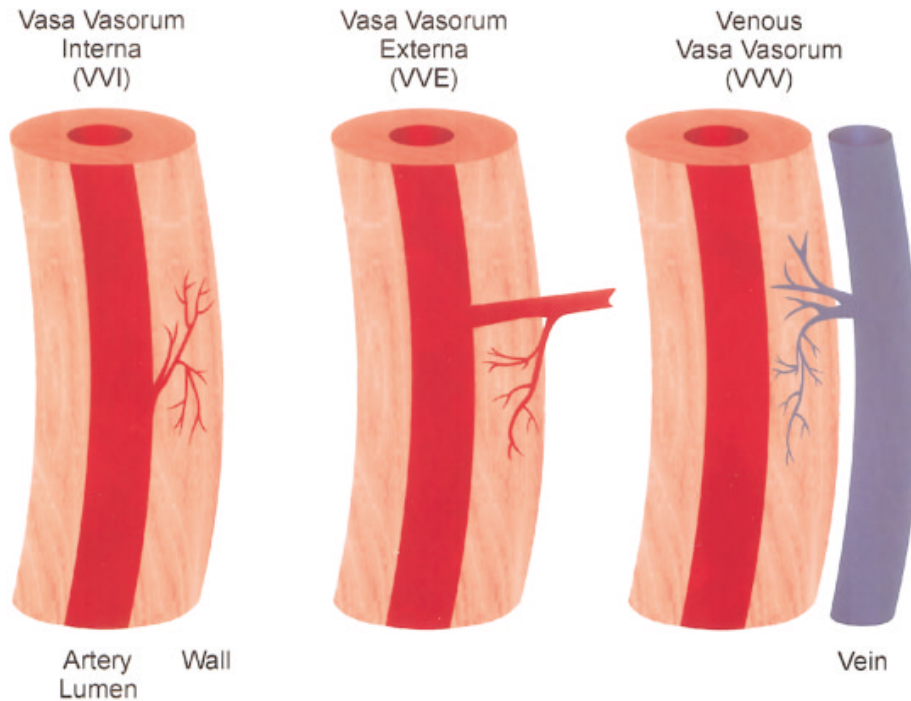


Figure 3.2: Different types of vasa vasorum. Reproduced with permission from [83]

analyzed to detect the presence of dynamic vasa vasorum and a method was developed to distinguish these important features from their surrounding structures with histological comparison.

The vasa vasorum is divided into 3 classes: the vasa vasorum interna (VVI), the arterial vasa vasorum externa (VVE), and the venous vasa vasorum (VVV) [83]. VVI refers to the vasa vasorum that directly stems from the lumen of the major vessel to which they belong. VVE represents the vasa vasorum that stems from a major branch from the major vessel lumen. VVV refers to the vasa vasorum that drain into veins. Fig. 3.2 shows the depiction of different types of vasa vasorum.

During endovascular imaging, multiple factors degrade structural EV-OCT with respect to motion artifacts, due to saline or contrast agent flushing, movement of the imaging and guide catheters, a beating heart, aortic and arterial pulsations, and breathing motion. Therefore, significant bulk motion-induced speckle modulation was detected during the imaging procedures and resulted in poor results when attempting to derive

vascular maps through standard techniques such as color-Doppler or speckle variance detection of blood flow [24, 25, 72]. In addition, optical clearing is indispensable in endovascular OCT, since blood is photon-opaque material. Optical clearing however has significant chances of collectively clearing the vasa vasorum too. Thus, conventional vascular mapping methods relying on blood scattering would not work in this scenario, nor does the low SNR in endovascular OCT permit such analysis. Other algorithms are needed to map out these elusive vessels.

In various research studies employing other imaging modalities before, the vasa vasorum has been shown to be dynamic, in the sense that the blood flow responds to changes in cardiovascular conditions, i.e. open or shut down during systole or diastole in the cardiac cycle. This corresponds to a kind of bulk motion as in the previous section. Therefore, vasa vasorum should be able to be mapped out by motion analysis methods.

Variance is the second moment of a random variable about the mean, (i.e. second order statistic). Speckle variance measures the spread of intensity values between frames such that blood vessels can be detected via the induced time varying speckle field pattern. Therefore, when this technique failed to distinguish the microvasculature from surrounding tissues, a higher order statistical moment was applied to detect these high intensity modulations due to blood flow and the dynamics of the vasa vasorum. Excess Kurtosis, K [84] is defined as

$$K = \frac{\mu_4}{\sigma^4} - 3 \quad (3.12)$$

$$\mu_4(m, x, y) = \frac{1}{N} \sum_{n=m}^{m+N-1} [I(n, x, y) - \mu_0(m, N, x, y)]^4 \quad (3.13)$$

$$\sigma^4(m, x, y) = \left(\frac{1}{N} \sum_{n=m}^{m+N-1} [I(n, x, y) - \mu_0(m, N, x, y)]^2 \right)^2 \quad (3.14)$$

$$\mu_0(m, x, y) = \frac{1}{N} \sum_{n=m}^{m+N-1} I(n, x, y) \quad (3.15)$$

where μ_4 is the fourth order moment about the mean intensity recorded at pixel (x, y) , σ

is the standard deviation at pixel (x,y) , m is the m -th frame of kurtosis signal, N is the number of frames used to compute the kurtosis, I is the intensity of each frame at pixel (x,y) and μ_0 is the mean between N frames at pixel (x,y) . Kurtosis is a fourth order statistical measure normalized by σ^4 to identify the deviation of a statistical distribution from the normal distribution. It can also be interpreted as measuring the “peakedness” of a distribution. The minus 3 in the definition is to subtract the kurtosis of the normal distribution ($\mu_4 = 3$, $\sigma = 1$), and hence K is coined as “excess kurtosis”. It has been shown that other biomedical imaging modalities have taken advantage of this metric to quantify non-Gaussian diffusion [85]. In another study, kurtosis was used for motion detection in general video analysis [86]. In EV-OCT, the kurtosis between sequential frames of a stationary target evaluates the distribution of intensity along the time axis. Any area of the tissue with significant changes over time will manifest as a high kurtosis signal value. Moreover, since from Eq. 3.12 the fourth moment about the mean is normalized by the fourth power of standard deviation of the structural OCT intensity, kurtosis values result from areas with weak intensity signal are not overwhelmed by strong SNR regions such as the pulsating vessel wall or the guidewire.

3.8 Application II: Speckle Reduction by a Parametric Iterative Algorithm

As mentioned in the last section, one main problem of EV-OCT is its relatively low SNR. Combined with the effect of the grainy appearance of speckle patterns, anatomical features and boundaries are severely degraded and obscured in the images. Current state of the art EV-OCT systems do not possess enough speed to utilize speckle information. Thus, there is a need to attenuate speckle patterns commonly seen in EV-OCT images.

The most simple technique for image restoration for blurred images is the least-square deconvolution as aforementioned. With a known point spread function of the

imaging system, there is a simple analytical solution to the problem. This works when the imaging system can be characterized by a simple point spread function without ANY noise. However, OCT has both multiplicative and additive noises. Therefore there is no simple solution to its noise problem. Theoretically, multiplicative noises can be transformed to additive noise via logarithmic compression and then they can be filtered in conventional ways, but it does not yield satisfactory results in reality since it would require a low pass filter with large kernel size and would severely obscure the edges.

Common hardware based approaches include frequency [87] and angular compounding [88], which are techniques involving averaging of different optical bands and different imaging angles, respectively. They are robust ways of speckle suppression as speckle properties vary across wavelengths or different illumination angles [72]. However, since they require additional optical components, and thus they may not be applicable to existing commercial EV-OCT systems.

Various studies have been devoted to speckle reduction using digital image processing techniques. Many of these are based on integral transforms and the manipulation of the associated coefficients [89–91]. Others rely on various algebraic iterations [92,93]. Optical beam divergence, nonuniform spatial sampling of the rotary scanning mechanism, and the subsequent interpolation all contribute to the speckle pattern shape and orientation variation in different parts of the image. These represent challenges to coefficient based speckle reduction methods. Since a typical EV-OCT pullback image sequence consists of several hundred images, algorithms with complex algebraic operations may not be efficient to tackle the large amounts of data.

In this study, we propose a simple, fast converging iterative algorithm modified from [94]. It is demonstrated that by optimizing the image during each iteration of a regularization method using a generalized divergence measure, β -divergence, speckle suppression and edge preservation can be achieved simultaneously. Moreover, one can freely adjust the trade-off between speckle suppression and edge preservation by adjusting

a single parameter.

The β -divergence algorithm was developed to first enforce least-square consistency of the despeckled image with the measured data, and then focus on the matching of details between the image and a reference image u using the β -divergence regularization measure, where u was constructed by median filtering of the original image with a 12×12 kernel and then filtered by a 5×5 averaging filter. To achieve this, using the β divergence (Eq. 3.6), the following inverse optimization problem was solved:

$$\hat{x} = \arg_x \min \|y - \mathbf{P}x\|^2 + \lambda \sum_i \frac{1}{\beta(\beta-1)} [x_i^{2\beta} + (\beta-1)u_i^{2\beta} - \beta x_i^2 u_i^{2(\beta-1)}] \quad (3.16)$$

where y is the measured image, \mathbf{P} is a point spread function, and the subscript i indicates the i th pixel of the image. The first term ensures the least-square consistency with the original image and the second term introduces the constraint (penalty term) for similarity matching between x and u . The image pixel values are squared to avoid negative values of x . By taking the derivative of Eq. 3.16 with respect to x , we arrive at the iterative scheme:

$$\hat{x}_i^{(n+1)} = \hat{x}_i^{(n)} - \varepsilon \left\{ 2(\mathbf{P}^\dagger \mathbf{P} \hat{x}^{(n)} - \mathbf{P}^\dagger y)_i + \frac{\lambda}{\beta(\beta-1)} [2\beta|\hat{x}_i^{(n)}|^{2\beta-1} - 2\beta|\hat{x}_i^{(n)}||u_i|^{2(\beta-1)}] \right\} \quad (3.17)$$

where \mathbf{P}^\dagger is the adjoint of \mathbf{P} , ε is the iteration constant, λ is the regularization constant and the superscript (n) represents the n th iteration. The image was normalized at each iteration to confine its gray scale value.

3.9 Summary of Chapter 3

In this chapter, in-depth description of the theoretical foundations of the work in this thesis is presented. Two OCT specific image manipulation methods are derived. The results in Ch. 4 will mainly be based on the theories and methods described here. For Ch. 5, the physical formation and statistical interpretation of speckle is described in this chapter but detailed formulation of the algorithm will be left for Ch. 5.

Chapter 4

Feasibility of Endovascular OCT in Carotid Artery of Large Mammals

4.1 Candidate Contribution

The candidate took a major role in the organization of the animal experiments. Substantial manipulation of devices during the experiments was also performed. All the data analysis presented in this chapter was done by the candidate. Publications resulting from these studies were prepared by the candidate.

4.2 Endovascular Imaging Protocol

Animal experiments were conducted in an animal facility of Saint Michael's Hospital. All animal experiments were conducted in operating rooms specifically designed for large mammals. Fig. 4.1 shows the setting of the operating room before the experiments. All of the procedures were done with anesthesia using ketamine and continued heart rate and blood pressure monitoring. In addition, a fluoroscopic X-Ray machine was used for all catheterization procedures with guiding purpose. All personnel involved with the experiments were mandated to be equipped with lead protective gowns to prevent X-Ray



Figure 4.1: Operating room setting for porcine experiments, showing the fluoroscopy machine and the patient table, closely mimicking the operating room scenario.

damage to internal organs.

In the study, six month old 50 kg pigs ($n=4$) were used. Each animal was ordered one week prior to the experiment to allow for acclimatization. A right groin dissection to expose the femoral artery was performed and an 8F short femoral sheath was inserted. Under fluoroscopic guidance a 5F Berenstein diagnostic catheter with a 0.035 inch guidewire was used to catheterize the common carotid artery (CCA). With a standard exchange maneuver a 6F long angiographic sheath (Shuttle, Cook, USA) placed in the mid CCA. A power injector was used for injection of saline or saline mixed with

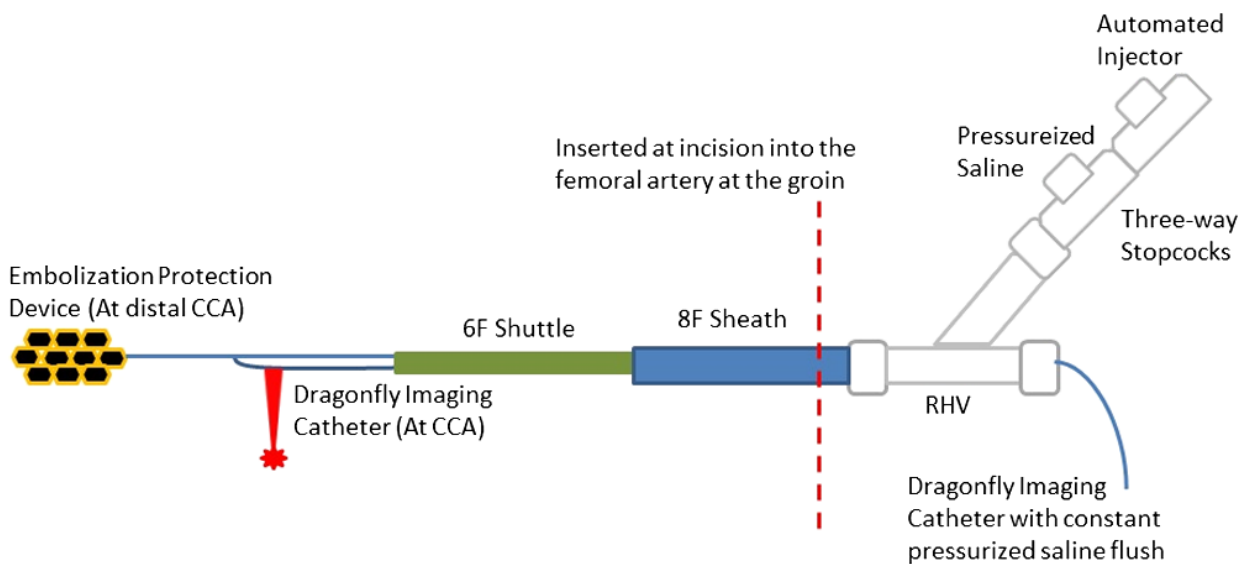


Figure 4.2: Schematics of the catheter system setup.

contrast for blood clearance during OCT image acquisition. An embolization protection device (AngioGuard, Cordis, USA) was then advanced through the 6F sheath and successfully deployed in the distal CCA, to protect the downstream blood vessels from thrombo-embolism. The monorail OCT imaging catheter was advanced over the AngioGuard wire into the desired position. After image acquisition, the OCT catheter was removed and a monorail system vascular stent was advanced and successfully deployed. The OCT imaging probe was then re-inserted to acquire volumetric data sets of the stent after deployment. Fig. 4.2 shows the schematics of the catheter system setup.

OCT imaging was performed by the FDA approved Fourier Domain OCT system with the use of the monorail imaging catheter Dragonfly (Lightlab Imaging, St. Jude Medical Inc. St. Paul, Minnesota, USA) that employs a rotary scanning mechanism in the radial direction and a pull-back scanning mechanism in the axial direction along the artery. The Fourier Domain OCT system employs a swept-source laser with center wavelength of $\sim 1300\text{nm}$ that is capable of 50,000 sweeps per second, has an axial resolution of $15\mu\text{m}$ and can perform 3D rotary imaging up to 100 frames per second. An automated injector was used to inject saline or saline with contrast (Omnipaq) via a three-way stopcock to

flush and clear blood during OCT imaging. Different injection schemes were tested to ensure optimized image quality for a typical 30mm carotid atherosclerotic plaque length.

The data obtained were then processed, where visual comparison between data sets would allow for the determination of the best injection scheme. Criteria for evaluation include the presence of residual blood in the images, the presence of motion artefacts such as jittering in the resultant images and the signal quality of the arterial wall tissues. For instance, these criteria are not mutually exclusive and a compromise needs to be reached by the physician and the EV-OCT operator. Due to the pulsation of the heart beat cycle and the finite duration of the pullback, the position of the carotid artery would fluctuate between each frame. The frames can be co-registered by rigid translation using cross correlation analysis between each frame [95], maximizing the correlation coefficient according to Eq. 4.1 by translating the next image frames by the optimal Δx and Δy :

$$\rho(\Delta x, \Delta y) = \frac{\Sigma^{x,y}(I_{n+1|x,y} - \bar{I}_{n+1|x,y})(I_{n|x,y} - \bar{I}_{n|x,y})}{\sqrt{\Sigma^{x,y}(I_{n+1|x,y} - \bar{I}_{n+1|x,y})^2} \sqrt{\Sigma^{x,y}(I_{n|x,y} - \bar{I}_{n|x,y})^2}} \quad (4.1)$$

After the frames were co-registered, the data were imported into a DICOM image viewer (OsiriX, The OsiriX Foundation, Geneva, Switzerland), to construct 3D views of the carotid artery with or without stenting.

The study was approved by Animal Care Committee of Saint Michaels Hospital, Toronto, Ontario, Canada. (Protocol ID: ACC 307) and follows the guidelines of Canada Council on Animal Cares (CCAC) Ethics of Animal Investigation.

4.3 OCT Imaging of Healthy and Thrombi Filled Carotid Artery

Different imaging catheter pullback speeds and contrast/saline injection rates were tested. In general, no noticeable difference was observed between pure saline and saline with

contrast and pullback speed equal to or below 6mm/s. Contrast/saline injection rate of 5-8cc/s would give the best results. Therefore, normal carotid artery imaging was optimized at \sim 6cc/s contrast/saline injection rate at a pullback speed of \sim 5mm/s. The consequence of using higher injection speed or pullback rate will be presented in the discussion section.

Fig. 4.3 shows the OCT image of normal porcine carotid artery. Figures 4.4 and 4.5 show a representative hematoxylin and eosin (H & E) staining and elastin trichrome staining of the porcine carotid artery wall, respectively. The OCT image clearly delineates the media, the external elastic lamina and the adventitia. In the next sections, it will also be demonstrated that EV-OCT can potentially detect vasa vasorum *in vivo* [96]. Fig. 4.6 shows a representative image of vasospasm of porcine carotid artery. A 3D reconstruction of the spasm segment is shown in Fig. 4.7. Note that the EV-OCT provides 2D cross-section views of the endovascular structures of pig carotid artery, where the data obtained by the pullback can also help form 3D rendering visualization of the carotid artery, allowing physicians to evaluate the size, morphology and distinctive features of the vessel wall for clearer and more efficient diagnosis. To demonstrate the ample amount of information contained in a 3D data set of EV-OCT data, Fig. 4.8 shows the 3D rendering view of a flattened adventitia layer of the porcine carotid artery obtained by vessel wall surface detection and alignment. From the flattened view, a distinctive network of channels is very clearly present in the image, which otherwise would not be visible in a cross-sectional rotary view of carotid artery EV-OCT. Fig. 4.9 also shows the side view of the flattened adventitia.

4.4 OCT Guidance in Carotid Stenting

Upon the optimized protocol for EV-OCT imaging, CAS was performed using standard carotid artery stents. Fig. 4.10 shows a representative stent image using pullback speed

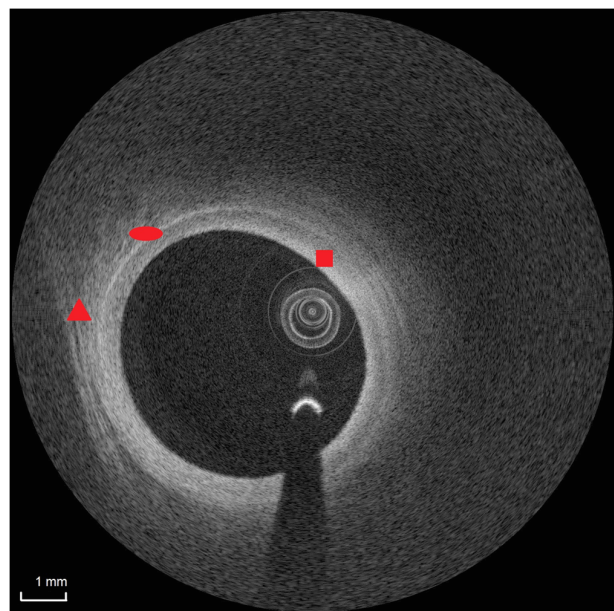


Figure 4.3: EV-OCT images of normal porcine carotid artery. Square: media; ellipse: external elastic lamina; triangle: adventitia.



Figure 4.4: H&E staining of normal porcine carotid artery.

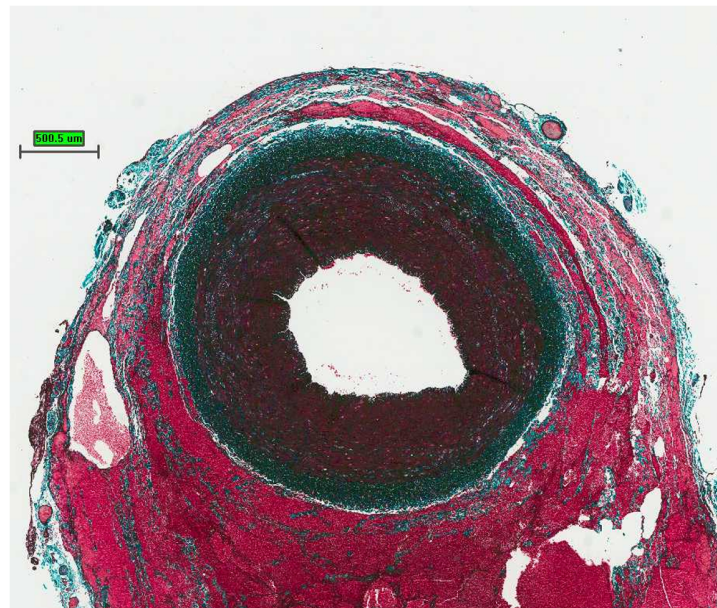


Figure 4.5: Elastin trichrome staining of normal porcine carotid artery.

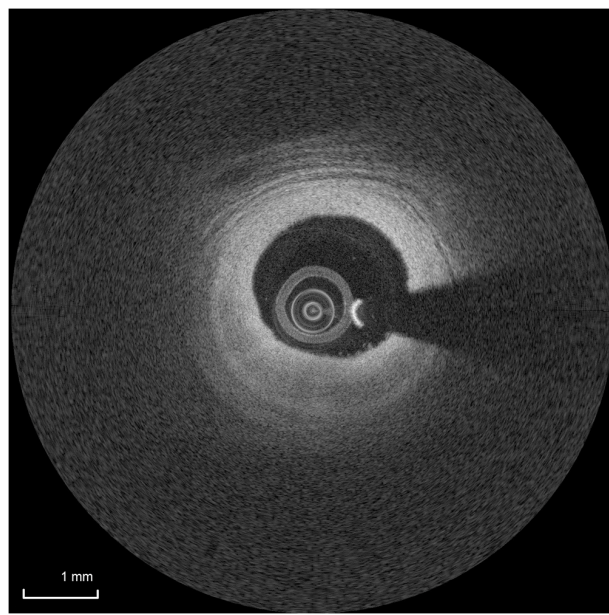


Figure 4.6: EV-OCT image of porcine carotid artery undergoing vasospasm.

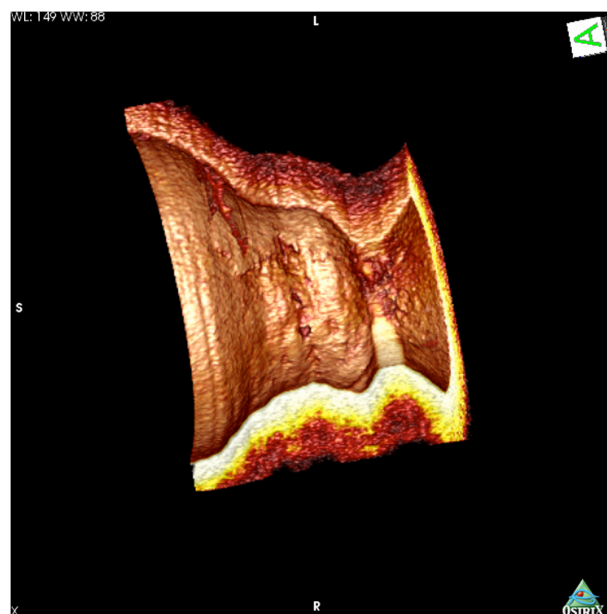


Figure 4.7: 3D view of vasospasm.

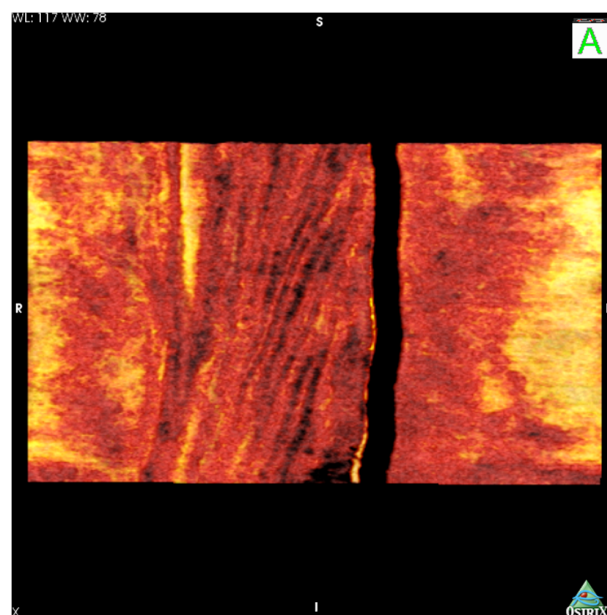


Figure 4.8: Flattened view of porcine carotid artery adventitia.

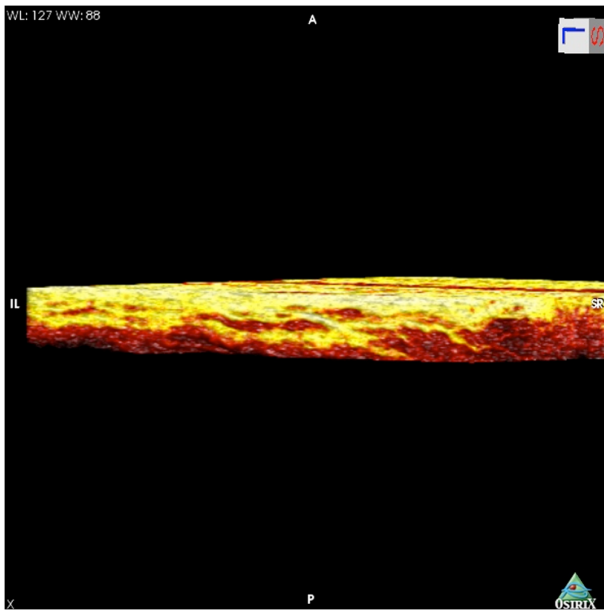


Figure 4.9: Side view of flattened adventitia.

of 5mm/s and flush injection rate of 5cc/s. From the image, the stent apposition can be clearly discerned. The image sequence was used to construct a 3D rendering of the stent. A representative rendering is shown in Fig. 4.11. Not only can a 3D rendering of OCT images visualize stent apposition, but it can also visualize complications such as blood clot and fibrin formation over the stent. A representative image is shown in Fig. 4.12, with a representative 3D rendering shown in Fig. 4.13.

4.5 Impact of EV-OCT on Neurovascular Interventional Procedures

Atherosclerotic plaque characterization in the coronary arteries has been extensively studied with intravascular ultrasound, and OCT has emerged more recently as a valuable tool in predicting the risk of potential rupture [97, 98]. On the other hand, carotid plaques have been mainly studied with ultrasound, computed tomography angiography or MRI [99–101]. OCT has the potential to expand our understanding of the individual

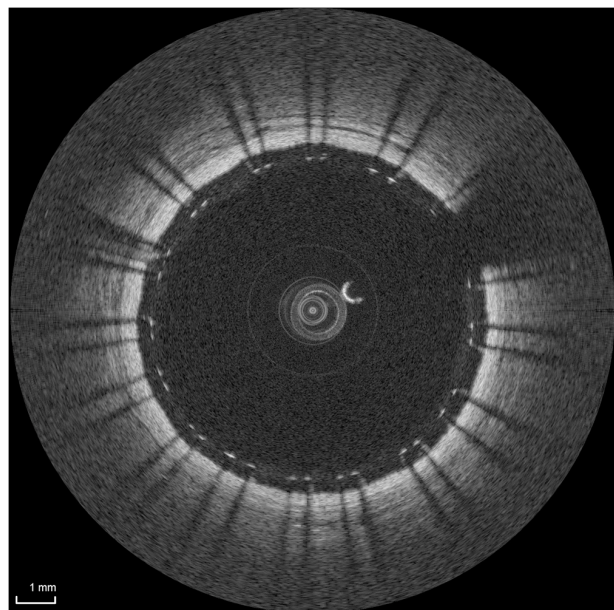


Figure 4.10: EV-OCT image of stented porcine carotid artery.

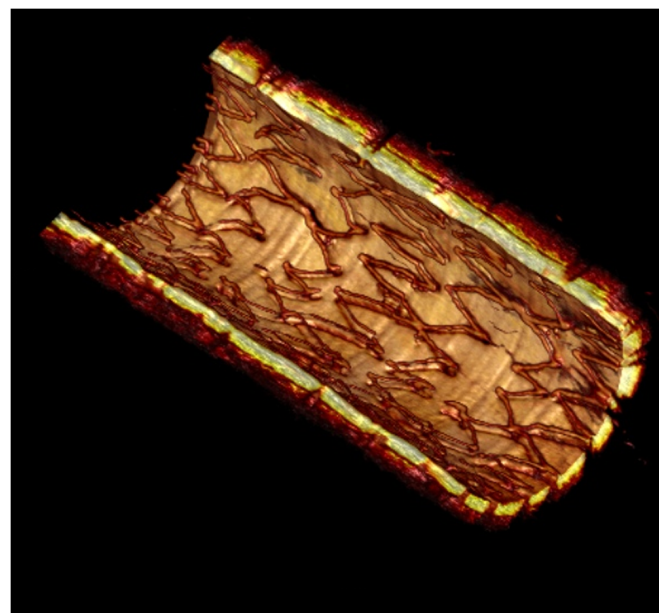


Figure 4.11: 3D rendering of properly stented pig carotid artery

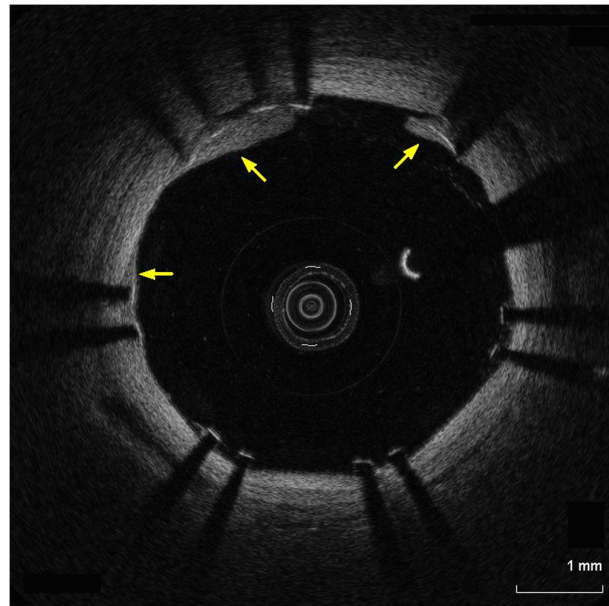


Figure 4.12: Stented porcine carotid artery with clots formed over the stent, arrows indicate clot locations.



Figure 4.13: 3D rendering of stented porcine carotid artery with blood clots forming over the stent.

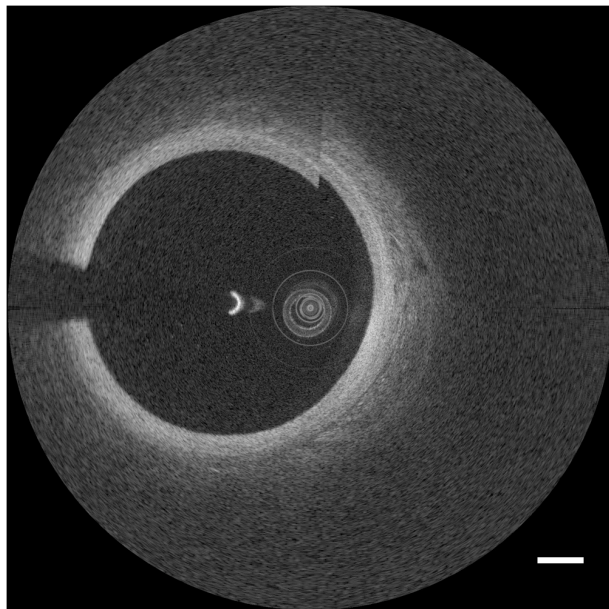


Figure 4.14: Image jittering resulting from excessive contrast injection or high imaging catheter pull-back speed. Scale bar represents 1mm.

risk of stroke from a carotid plaque.

During the experiments, the pullback speed of the imaging catheter was limited to 6mm/s and the injection rate of the saline/contrast was limited to 5cc/s. Higher contrast injection rate would induce high frequency vibration of the imaging catheter and would result in image jittering as shown in Fig. 4.14. However, there are image artefacts, most noticeably double reflection, that one must beware of (an example is given in Fig. 4.15). These artifacts should not be misinterpreted as features as this can possibly lead to false-positives.

From Fig. 4.3, the image clearly demonstrates that EV-OCT is capable of providing high resolution images in high blood flow vessels such as the carotid artery. This can be further confirmed by the Hematoxylin & Eosin (H & E) and elastin trichrome staining histology in Figs. 4.4 and 4.5. The media, external elastic lamina and the adventitia are well correlated with histology. The difference in thickness between the OCT image and histology can be attributed to tissue shrinkage during histological processing and imprecision in matching their locations. An example of vasospasm, which is a focal

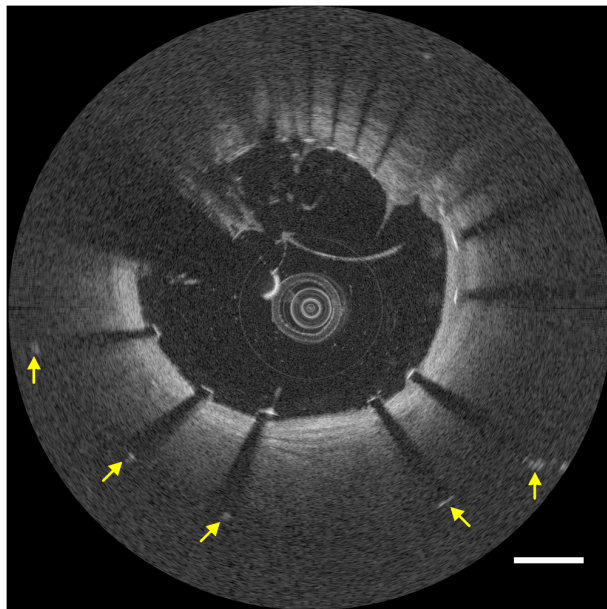


Figure 4.15: EV-OCT image artifacts caused by double reflection. Notice that many stent strut locations are falsified (indicated by arrows), with some displayed inside the lumen and some being displayed all the way into the adventitia. Scale bar represents 1mm.

reduction in the vessel lumen secondary to contraction of the vessel wall smooth muscle, was imaged by EV-OCT and shown in Fig. 4.6. In the wake of rapidly advancing computer speeds and display technologies, manipulation of EV-OCT data in the domain of 3D visualization can prove to be valuable in evaluation of conditions in the carotid artery. Fig. 4.7 shows the 3D rendering of the vasospasm segment. This may allow clinicians to fully appreciate the extent and nature of the luminal narrowing. Further manipulation of EV-OCT data can also bring out interesting information. In Fig. 4.8, the flattened view of the carotid artery adventitia shows distinct channels in half of its surface area. These channels are suspected to be nerves since the water content in peripheral nerves is high and may have a low back scattering coefficient. Therefore, the nerves would appear as dark channels. These channels may also be vasa vasorum. Figure 4.9 shows the side view of the adventitia, in contrast to the view in Fig. 4.8, the other half of the area of the adventitia is comprised mainly of laminar structures. Therefore EV-OCT has the potential to further our understanding of the physiological responses

of the cardiovascular system in correlation to its anatomical features.

In order to enhance diagnostic efficiency and evaluate the overall apposition of the carotid stent, a 3D view of a stented vessel is indispensable. Tearney *et al.* have previously accomplished a considerable body of research on this aspect in a previous study using OCT systems [102]. However, for the carotid artery, a faster and more robust OCT system is needed for 3D reconstructions due to the high blood flow rate and larger vessel diameter. With the Fourier Domain OCT system, complete 3D views of the stent after CAS using intensity thresholding were obtained (Fig. 4.11). The degree of apposition of the stent to the vessel wall is clearly depicted. This was due to the fact that metal stents pose a much lower probability of direct back reflection of light into the imaging catheter (due to surface curvature) than the vessel lumen surface. Thus, when mapping to colors corresponding to lower intensity values, they can be clearly distinguished from the vessel wall tissues. Not only can the stent be clearly visualized, but stent associated thrombus formation can also be clearly identified (Fig. 4.13). This is possible as blood and thrombus are highly scattering media.

The ability of EV-OCT to image the carotid artery and to generate 3D visualization of the stented artery was demonstrated in this study. The optimal flushing and imaging protocols were also developed. Further study should be carried out in pig models of different stages of carotid atherosclerosis to generate an atlas to provide a complete description of the disease progress, as well as on stenting in diseased artery to evaluate possible complications of CAS.

4.6 Preliminary Study on Vasa Vasorum Detection

The kurtosis algorithm was first verified using a flow phantom. A pulsatile flow was mimicked manually using titanium dioxide solution in a 30 gauge plastic tube, so that the intensity inside the tube imaged by OCT (Thorlabs Inc.) underwent sudden and

large changes. The image data obtained were then processed with the kurtosis algorithm (Eq. 3.12). Yorkshire pigs weighing $\sim 50\text{kg}$ were housed in animal vivarium for one week prior to the experiment. Upon sedation with intramuscular injection of ketamine, the pig was anesthetized with continuous inhalation of isoflurane and monitored by a physiologic monitor for any potential complications. A surgical incision exposing the groin of the pig to gain access to the femoral artery and 8-French (8F) sheath were established with subsequent heparinization at 100U per kg. A 5-Fr diagnostic catheter was then inserted into the femoral artery with guidewire to select the common carotid artery. The 5-Fr catheter was then exchanged with a 6F Shuttle guide catheter, allowing placement of an embolic protection device (AngioGuard, Cordis) distally in the carotid artery. The AngioGuard contained a proximal monorail guidewire upon which the EV-OCT imaging catheter (Dragonfly, LightLab Imaging) was installed. Variable mixtures of saline and contrast agent (Omnipag) using an automated pump were injected during EV-OCT imaging using a SS-OCT system (LightLab C7-XR, LightLab Imaging), with customized high-speed data acquisition. All animal procedures were approved by St. Michaels Hospital (Toronto, ON) Animal Care Committee.

For the detection of pulsating vasa vasorum using intensity kurtosis, the resolution of the OCT system must be sufficient to detect the actual vessels from the surrounding structures. In addition, the frame rate of the system must be of a greater value than the inherent pulsation rate such that the kurtosis algorithm can capture sudden intensity changes. The C7-XR SS-OCT system provided an axial resolution of $15\mu\text{m}$ where images were acquired at 100Hz frame rate. The spot size was $\sim 25\mu\text{m}$. For the vasa vasorum, which typically are $\sim 40\mu\text{m}$ in size [83], a $15\mu\text{m}$ axial resolution was adequate to detect their presence. The frame rate of the system was also much higher than the heart rate and, therefore, the pulsation rate of the vasa vasorum.

Both the speckle variance and the kurtosis algorithms were applied to EV-OCT images acquired at 100 frames per second. A particular scenario occurs when the contrast/saline

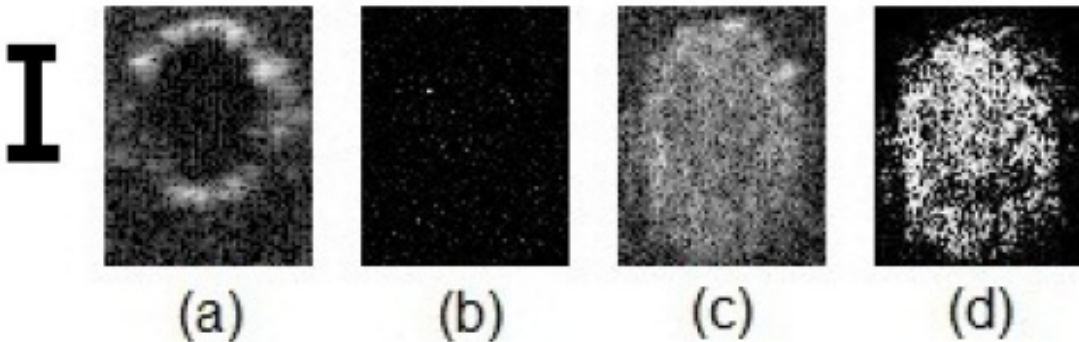


Figure 4.16: 30 gauge flow phantom results: (a) Phantom with air inside; (b) Kurtosis signal corresponding to (a); (c) Flow phantom with sudden injection of titanium oxide solution; (d) Kurtosis signal corresponding to (c). Scale bar represents 0.2mm. The tube appeared larger when titanium oxide solution was imaged due to refractive index changes.

mixture injection partially flushes the pulsatile blood flow in a time varying manner, during which boluses of blood enters the imaging field of view, causing large intensity variations throughout the image, especially from the vessel wall. This is chosen as an extreme scenario to test the kurtosis algorithm, specifically the ability to suppress such artifacts. From a clinical perspective, this is the threshold condition for determining the minimal contrast/saline flush injection rate for a particular blood vessel and its associated flow rate, to achieve optical clearing condition for imaging while maintaining flow.

With full displacement of blood during imaging, the imaging catheter is maneuvered close to the vessel wall to improve lateral resolution and OCT intensity. Identification of vasa vasorum is performed by searching for areas of reduced image intensity in the adventitia and verified with kurtosis signal processing, for temporal variation in synchrony with heart beat yet distinct from vessel wall pulsations.

Figure 4.16 demonstrates the result from the flow phantom experiment using SS-OCT in the raster scanning configuration. In Fig. 4.16a, there is no flow in the flow phantom tube and as a consequence there is no kurtosis signal (Fig. 4.16b). However, when titanium oxide solution is injected into the phantom (Fig. 4.16c), a strong kurtosis signal shows up due to the sudden surge in intensity inside the flow phantom (Fig. 4.16d).

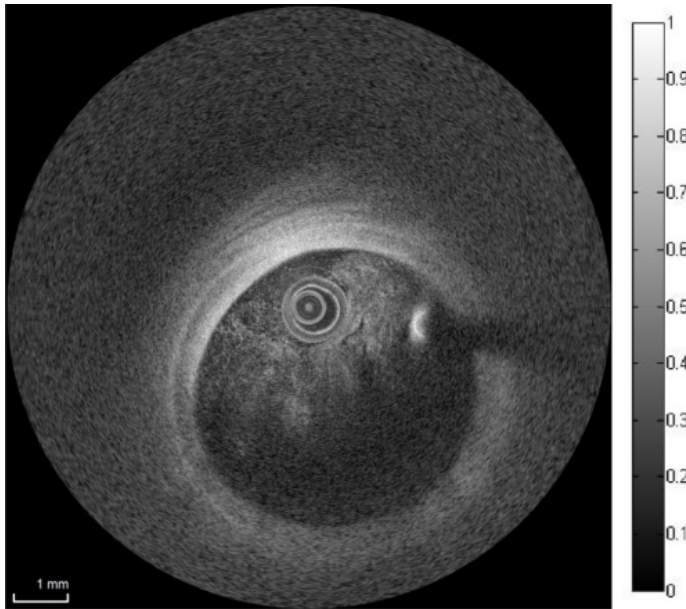


Figure 4.17: EV-OCT image of the blood-saline flush experiment.

During *in vivo* porcine experiments when investigating the threshold condition of appropriate flush injection rate, EV-OCT signal intensity varied significantly depending on completeness of blood displacement by flushing fluid pump injections (contrast/saline mixture). Fig. 4.17 shows one frame of the EV-OCT image sequence obtained with the blood-saline flush experiment. Figure 4.18 shows a speckle variance OCT (svOCT) map computed with the blood-saline flushing EV-OCT image sequence. Figure 4.19 demonstrates a normalized kurtosis map computed with 32 frames of the blood-saline flushing EV-OCT image sequence. The kurtosis motion analysis algorithm clearly gives strong kurtosis signal whenever the blood flushed in. It also demonstrates that the algorithm is extremely sensitive to outliers. If even one of the 32 frames takes on a major difference with the other 31 frames, this difference would manifest as a strong kurtosis signal in the vicinity as seen in Fig. 4.19.

Figure 4.20 shows one frame of a porcine carotid EV-OCT image sequence. The imaging catheter was placed close to the artery wall, where the carotid artery abluminal surface was not supported, as evident from the loose structure shown in the image. As the image demonstrates, a number of low intensity regions can be found throughout

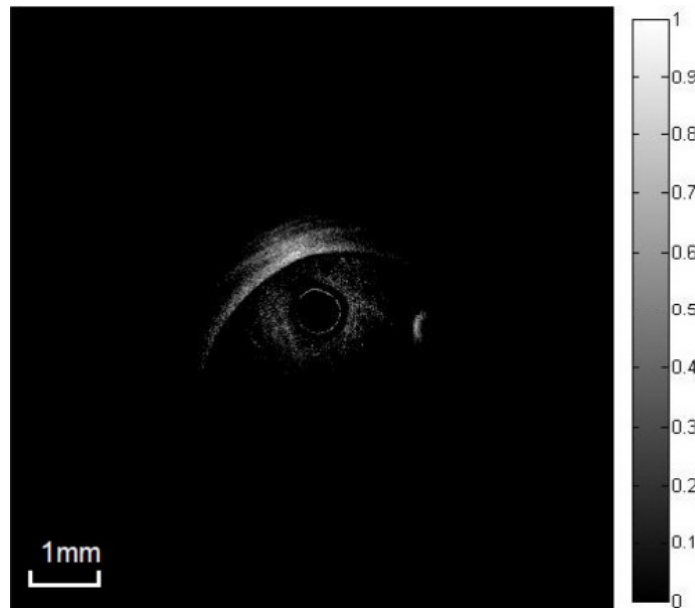


Figure 4.18: svOCT image of the blood-saline flush experiment.

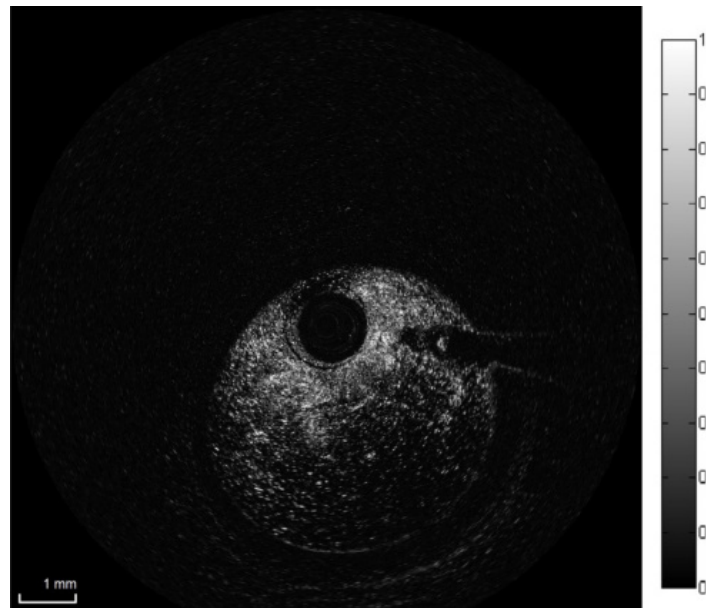


Figure 4.19: One example kurtosis map of the blood-saline flush experiment when the flow took on a sudden change. The signal in the lumen depicts the sudden surge of blood.

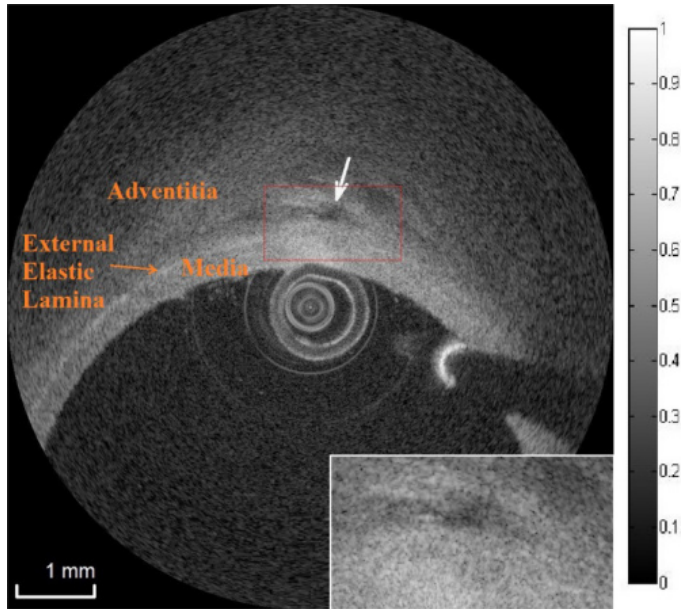


Figure 4.20: Stationary EV-OCT image of porcine carotid artery when the imaging catheter is placed close to the vessel wall. The supposed vasa vasorum is indicated by the white arrow. Scale bar = 1mm. Inset is the zoomed in version of the red box.

the image. Typically, these low-signal areas depict the presence of a blood vessel [75], where the question remains: Are these in fact vasa vasorum vessels or are the dark areas associated with fat deposits (or equivalent low signal tissue structures) as typically imaged by OCT. Speckle variance imaging was also investigated in this part of the experiment, with a typical SV image displayed in Fig. 4.21. This is computed with the same data sequence as previously presented in Fig. 4.20. As seen in Fig. 4.21, large svOCT signals around the vasa vasorum were observed, yet may not be adequately distinguished from bulk tissue movements associated with carotid vessel wall pulsations, especially with the imaging catheter in close proximity of the vessel wall and high backscatter. The brightest region is due to high reflectivity from the guidewire. Figure 4.22 demonstrates a normalized kurtosis map from a sequence of maps each computed with 32 frames of the porcine carotid EV-OCT image sequence.

Neglecting the entire signal caused by motion artefact on the lumen wall and the catheter, a high kurtosis signal region appears right above the arterial wall, and approximately at the luminal side of the adventitia. The location of this high kurtosis signal

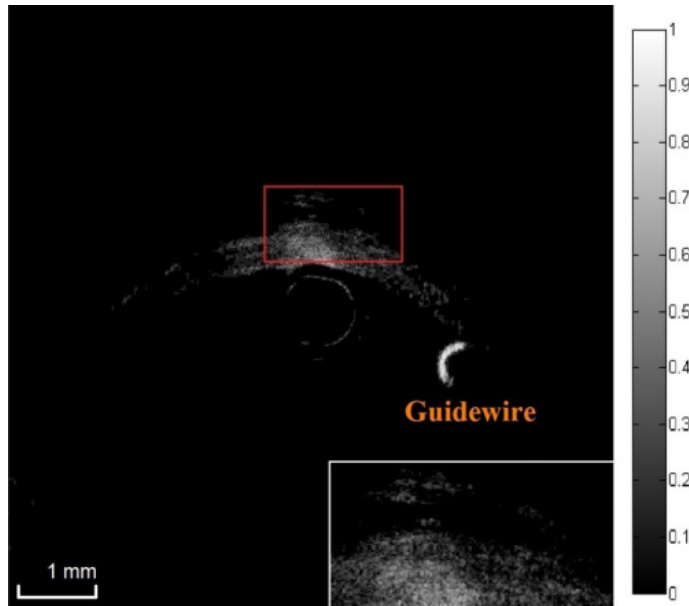


Figure 4.21: svOCT of porcine carotid artery with the catheter parked. Scale bar = 1mm. Inset is the zoomed in version of the red box.

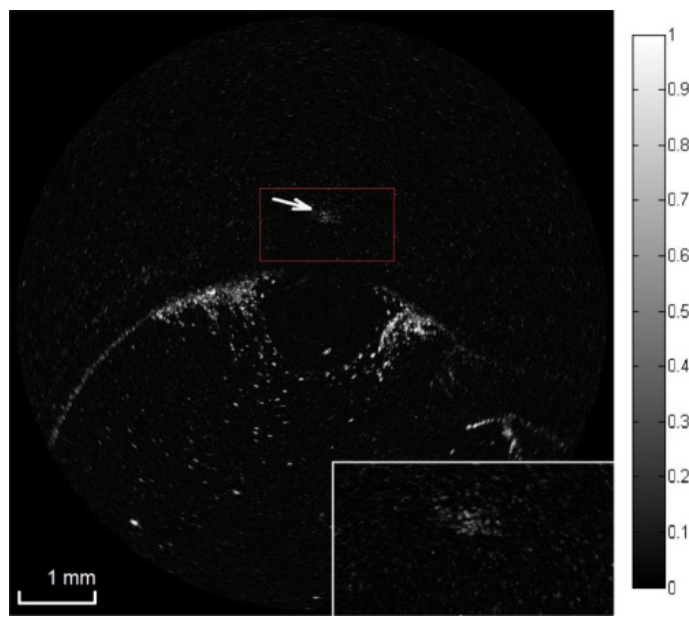


Figure 4.22: Kurtosis signal map of porcine carotid artery when the imaging catheter is placed close to the vessel wall. The vasa vasorum is indicated by the white arrow. The flowing of blood clot debris [64] is also visible near the vessel wall and the lumen. Scale bar = 1mm. Inset is the zoomed in version of the red box.

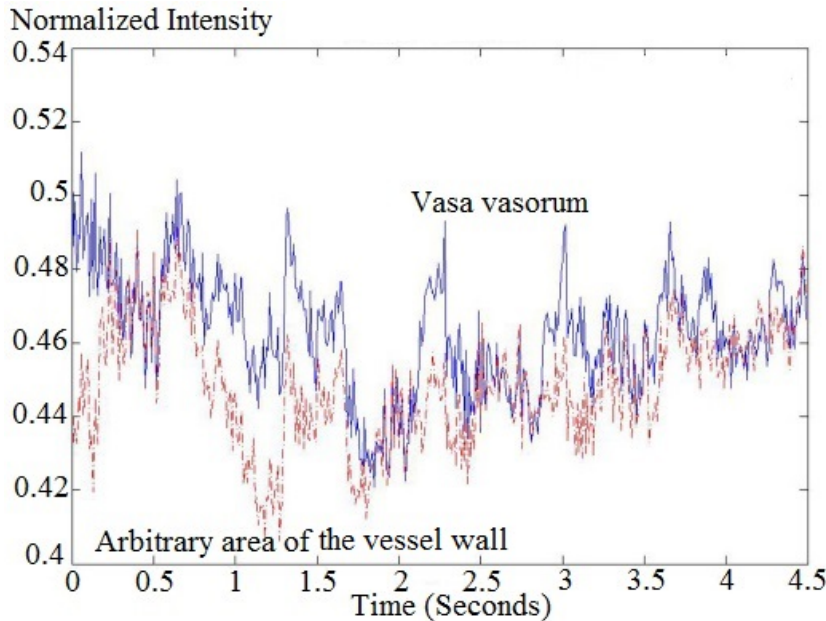


Figure 4.23: Average intensity of a region of interest around the vasa vasorum and an arbitrary section of the vessel wall versus time. Although periodic variation in intensity is also observed in the vasa vasorum, these intensity fluctuations are of the same approximate value, making it extremely difficult to identify vessel wall structures such as the vasa vasorum micro-vessels.

region coincides with one of the low-signal regions appearing in the EV-OCT structural image (Fig. 4.20). However, as can be seen in Fig. 4.22, not all low-intensity regions in the EV-OCT image correspond to high signal intensity in the kurtosis map. A region of interest (ROI) is drawn around the area outlined in Fig. 4.20. The average intensity of EV-OCT images, the average speckle variance and the average kurtosis signal in the ROI are plotted versus time in Fig. 4.23, Fig. 4.24 and Fig. 4.25, respectively. The average speckle variance in the ROI (Fig. 4.24) did not follow any pattern. Speckle variance was much larger in the ROI, misleadingly because of its proximity to the imaging catheter. The average kurtosis signal in the ROI (Fig. 4.25) followed a periodic pattern with respect to time, where the frequency of this modulation correlated to the pig heart rate of ~ 85 beats per minute. Therefore, the continuous EV-OCT data set was processed via the kurtosis algorithm to identify this periodic blood flow, which we believe corresponds to the vasa vasorum.

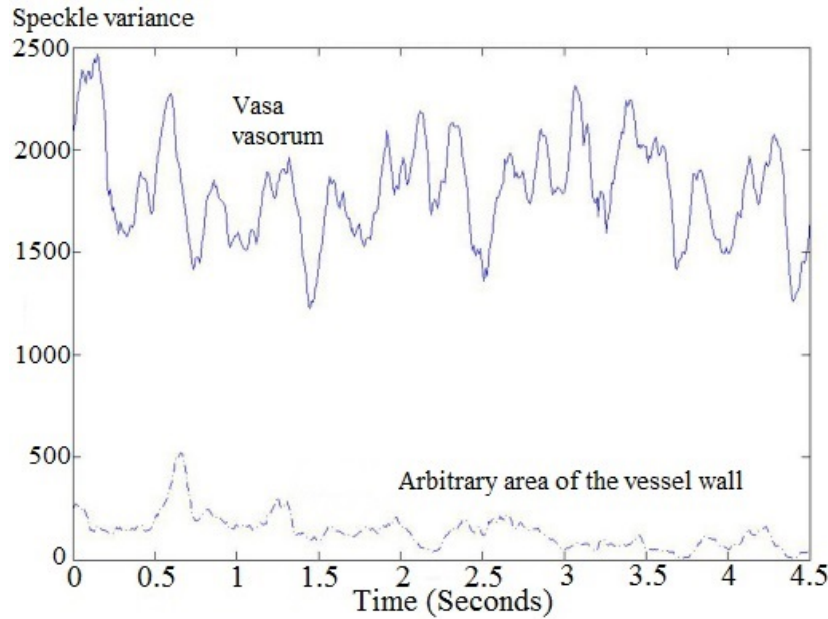


Figure 4.24: Average speckle variance of suspected vasa vasorum region and an arbitrary section of the vessel wall versus time. At the vasa vasorum, misleadingly, the speckle variance is much larger due to its proximity to the imaging catheter. Speckle variance was computed within a moving time window of 8 frames, updated at 100fps.

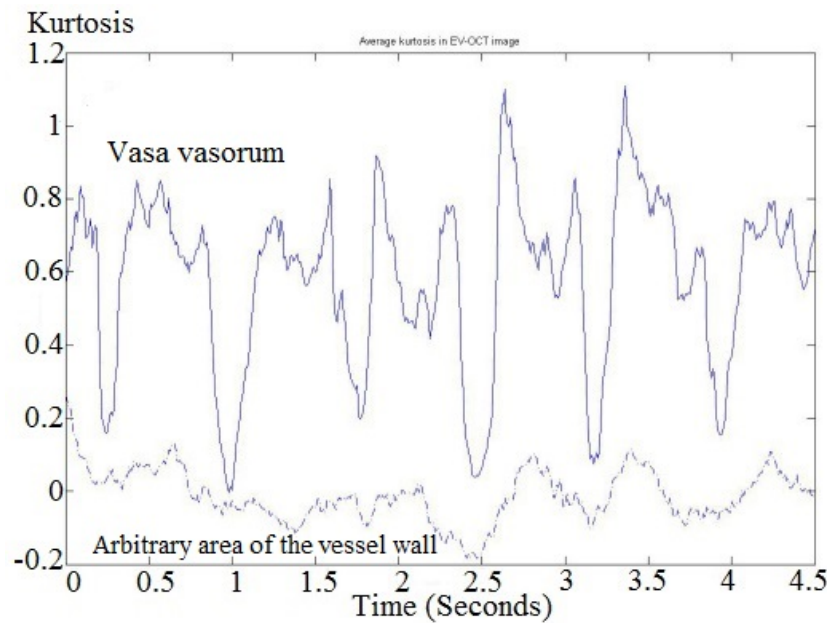


Figure 4.25: Average kurtosis of suspected vasa vasorum region and arbitrary vessel wall region versus time. At the vasa vasorum, the kurtosis is much larger due to pulsation of blood filling and emptying the micro-vessels. Note the increase in pixel intensity of the vasa vasorum region, which acts as a contrast mechanism such that these vessels become visible and stand out when compared to the surrounding tissue. Kurtosis was computed within a moving time window of 32 frames, updated at 100fps.

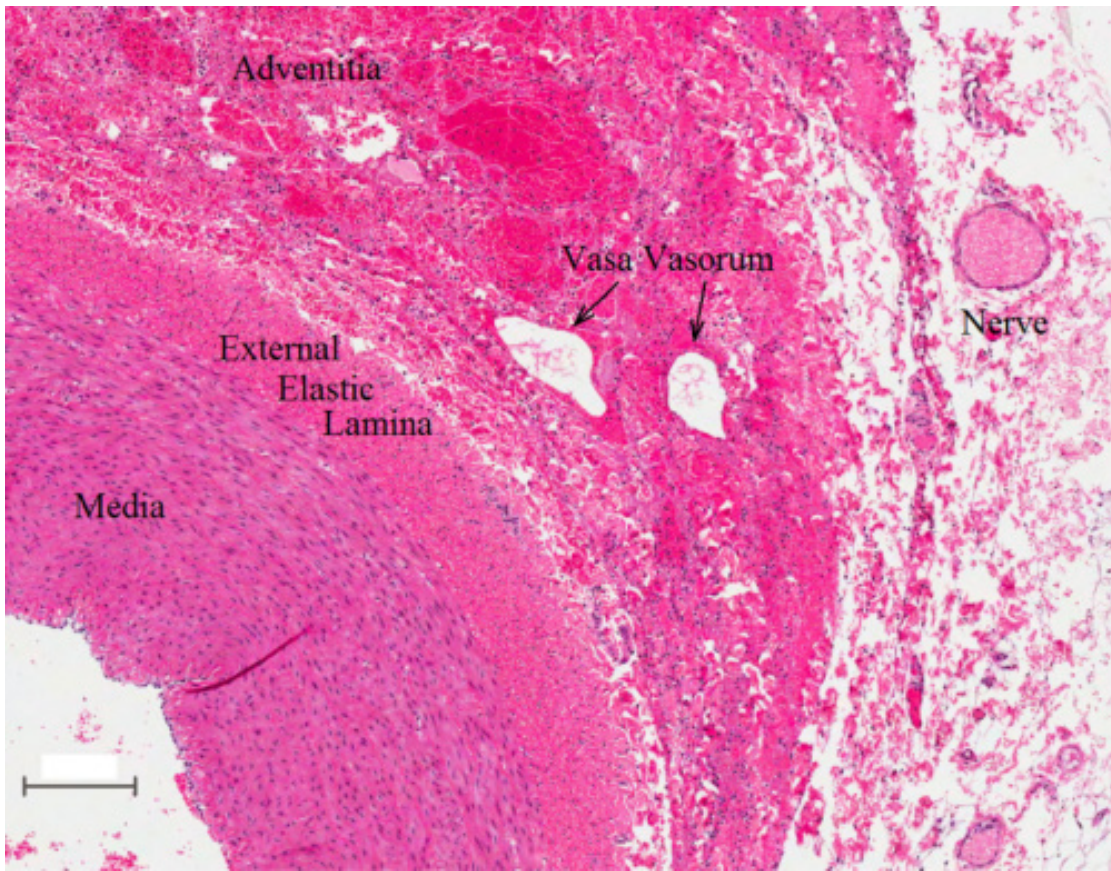


Figure 4.26: H&E staining of porcine carotid artery. The black arrows point to vasa vasorum at the adventitia. Scale bar represents $200\mu\text{m}$.

Figure 4.26 shows an example H&E staining of a representative section of porcine carotid artery. As can be discerned in the image, in the adventitia area, there are a number of blood vessels that correspond to the location of the detected micro-vessel in the adventitia of the kurtosis maps and EV-OCT images. However, there are also a considerable number of void regions (unstained regions or regions filled with blood but without nucleated tissue surrounding them) that do not correspond to micro-vessels. Moreover, nerves are also present in the adventitia area, as seen in Fig. 4.26. Thus, by distinguishing the beating motion of vasa vasorum from other tissues, the intensity kurtosis detection method provides a simple and fairly robust way to identify the dynamic vasa vasorum and analyze their blood flow dynamics.

Figure 4.27 shows another set of EV-OCT data depicting the structural image of

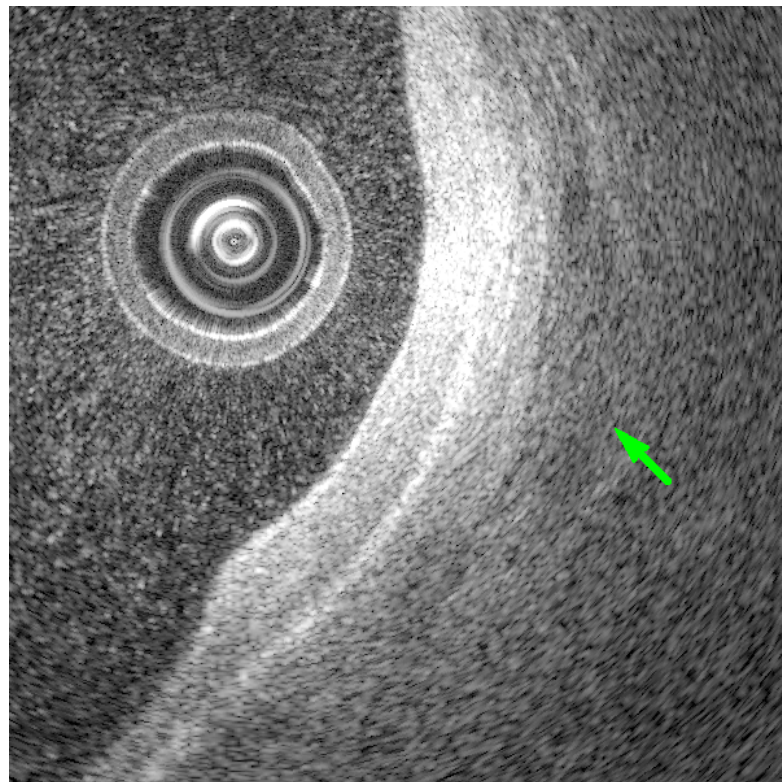


Figure 4.27: Structural image of vasa vasorum data set 2, the green arrow points to the vasa vasorum.

vasa vasorum and Fig. 4.28 shows the corresponding map processed by our proposed kurtosis algorithm. Owing to the difficulty in obtaining parked arterial wall data and resources available, the results shown can at most be rendered as a proof-of-principle study. Further systematic investigations into the dynamics of vasa vasorum should be carried out when the resources and technologies become feasible in the future.

An additional benefit of implementing the intensity kurtosis algorithm is that it could be used to identify the presence of blood clots and thrombus flowing along the lumen of the artery during imaging. The flow of blood clot debris creates a large and sudden jump in intensity. As can be viewed in Fig. 4.22, the clot debris generates very high kurtosis signal in the lumen area. If this algorithm can be displayed in real-time, the technique not only offers additional vessel wall information, but could also be used to identify threats such as the dislodging of thrombi, where the surgeon may have an opportunity to take

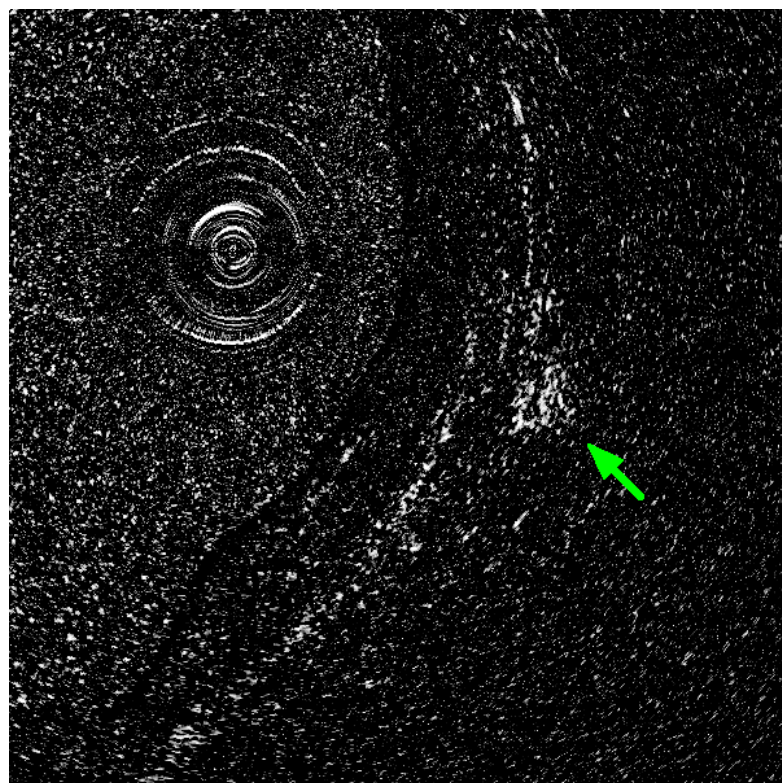


Figure 4.28: Kurtosis map of vasa vasorum data set 2, the green arrow points to the vasa vasorum.

appropriate measures to protect patients in these situations.

From Fig. 4.18, the svOCT signal of the guidewire and of the vessel wall in the vicinity of the imaging catheter masks out all the blood-saline flush signal in the lumen. In Fig. 4.19, however, the blood-saline flush gives out a strong kurtosis signal. Moreover, the kurtosis measurement rejects both the guidewire and quasi-static carotid vessel wall. This shows that the kurtosis algorithm clearly has significant advantage when measuring pulsed flow. It can reject stationary objects even in high clutter scenario, yet giving out strong signal in areas corresponding to changes in intensity.

From Fig. 4.21. It can be clearly seen that the speckle pattern fluctuates randomly, throughout the image. This is due to the fact that speckle depends on the interference of randomly scattered photons throughout the volume of interrogated tissue [24]. Therefore, any induced tissue motion such as the smooth muscle tone, flushing that vibrates the catheters, and the vibration of the catheter itself can alter the coherence of the photons. When these artefacts add up together, a bulk overall time varying speckle pattern results, rendering speckle variance detection of microvasculature, via our current hardware setup, impossible.

The kurtosis measurement, on the other hand, does not depend on speckle. The metric measures the deviation from a Gaussian distribution. It is sensitive to outliers, and therefore, only sensitive to sudden, major changes of intensity between imaging frames. As shown in Fig. 4.25, the cycle of the kurtosis signal consist of two peaks with a dip in the middle. The first peak corresponds to the blood filling the vasa vasorum and therefore induces a sudden increase in intensity in the EV-OCT image. The second peak corresponds to the blood emptying the vasa vasorum and thereby induces a sudden decrease in intensity in EV-OCT image.

Various studies have been devoted to the understanding of the vasa vasorum. It is believed to play an important role in atherosclerosis [78]. One very important aspect is that vasa vasorum is dynamic. The flow in these structures can be transiently obstructed

by the blood pressure of the main vessel wall, can undergo vasodilation or vasoconstriction and most importantly they can undergo angiogenesis in response to external factors. In the presented results, the filling of blood due to the arrival of the systolic pressure pulse into the vasa vasorum was clearly observed. Via our kurtosis detection method, this study has demonstrated to our knowledge, the first OCT technique capable of identifying vasa vasorum *in vivo*. This method may prove to be useful in evaluating the health of the artery as it can clearly delineate a periodic pattern directly correlating to the heart beat rhythm. If there are any abnormalities with the artery, this periodic pattern may be altered to become irregular. For example, in hypertension patients, one could expect that the pressure on the vasa vasorum is higher and therefore, the duration of blood filling in the kurtosis signal pattern may be significantly reduced. Thus the intensity kurtosis could be a useful way to assess the health of the dynamic vasa vasorum, which in turn can be indicative of the risk, the onset or even the progression of atherosclerosis.

The limitations of this study was that since porcine experiments are very costly so that not many data sets can be readily obtained. As a result, this remains a proof of principle study to identify vasa vasorum *in vivo*. Moreover, the method works best when the imaging catheter is parked near the vessel wall in order to obtain the highest SNR and it requires a certain time to capture the beating of these microvessels, thus a pullback scanning to map vasa vasorum is impossible at this moment. Since current atherosclerosis research has not yet focused on the impact of vasa vasorum, a larger scale and more rigorous study should be carried out in the future when more resources are available for this aspect.

4.7 Speckle Reduction of Endovascular OCT

OCT images were obtained using a commercial Lightlab C7-XR Fourier Domain OCT system (Lightlab Imaging). The speckle reduction algorithm was applied to EV-OCT

images in the Cartesian configuration. To demonstrate the speckle suppression effect of the algorithm, an initial test image of human finger skin was obtained by pressing two fingertips against the imaging catheter tip. In vivo endovascular OCT imaging of the porcine carotid arterial wall image was obtained subsequently with eccentric placement of the imaging catheter to demonstrate the versatility of our algorithm to suppress speckle at different parts of the image. All animal procedures were approved by St. Michaels Hospital (Toronto, Ontario) Animal Care Committee.

In the algorithm, \mathbf{P} was chosen as a simple 3×3 Gaussian function for simplicity since the presence of speckle noise makes the genuine PSF not attainable (Eq. 3.5). ε was chosen to be 0.75 and λ was set to 0.6 determined by trial and error interactively by the OCT operator. After ε and *lambda* were chosen, they were fixed for all furhter measurements. The reference image u was generated by passing the unprocessed image to a 12×12 median filter and then filtered by a 5×5 averaging filter. Median filters have been used before for speckle suppression [103], while averaging filters can effectively remove additive noise, since speckle in the EV-OCT image after logarithmic compression becomes additive. The algorithm was set to run for 40 iterations as the result started to converge to ~ 0.002 mean square difference from u . Figure 4.29(a) shows the original finger skin image, and Fig. 4.29(b) demonstrates the despeckled finger skin image processed with our proposed algorithm. Most of the features were preserved in the despeckled image due to the robustness of β -divergence against outliers, while the grainy appearance was mostly smoothed. Figures 4.30 and 4.31 show the original and despeckled ($\beta=3$) carotid arterial wall image, respectively. After speckle suppression, the grainy appearance of the tissue was clearly removed.

To quantitatively evaluate the performance of the algorithm on real endovascular images, a number of metrics were calculated for a region of interest (ROI) encompassing high signal regions (media) and low signal regions (adventitia) versus a noise background as depicted in Fig. 4.30. The signal-to-noise ratio (SNR) was defined as

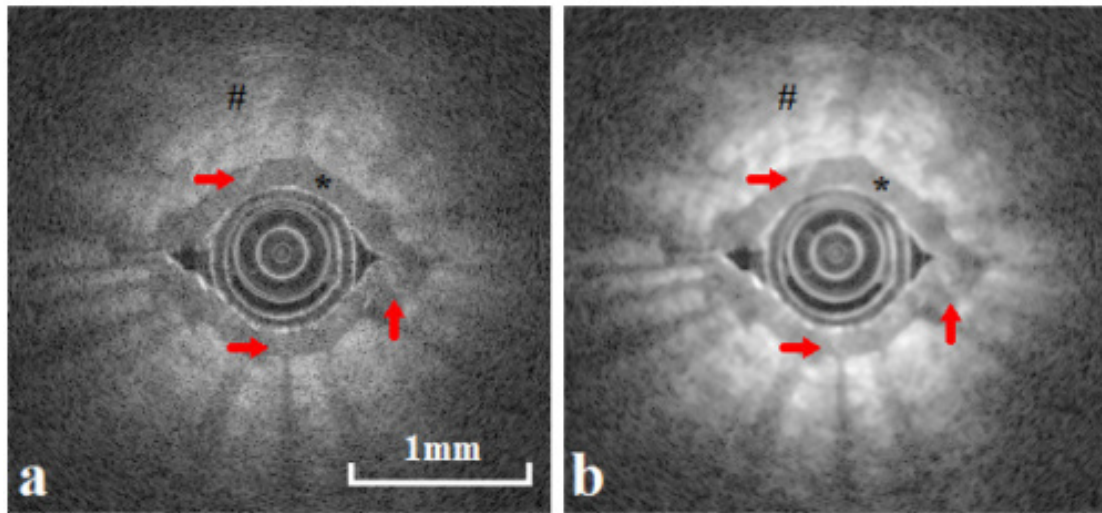


Figure 4.29: (a) Original finger skin image; (b) despeckled finger skin image. (*) indicates the stratus corneum, (#) indicates the dermis, and the red arrows point to the sweat glands.

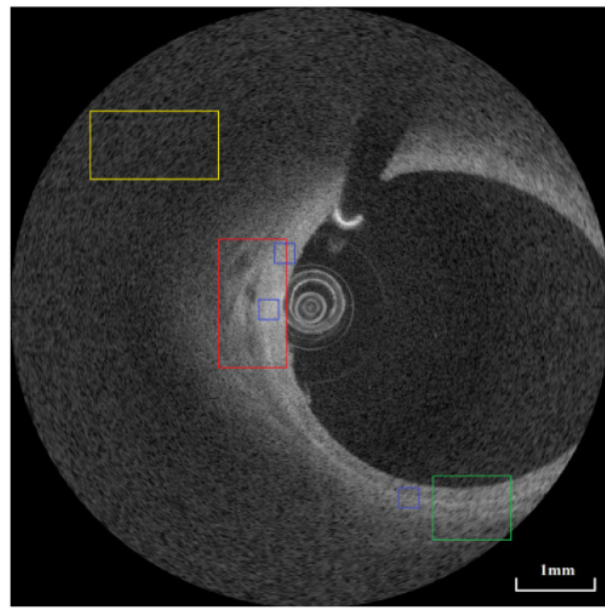


Figure 4.30: Original porcine carotid artery EV-OCT image. The red ROI indicates the signal region and the yellow ROI indicates the noise region used in the metrics calculation. The green ROI indicates the zoomed region in Fig. 4.33. The three blue ROIS are used for ENL calculations.

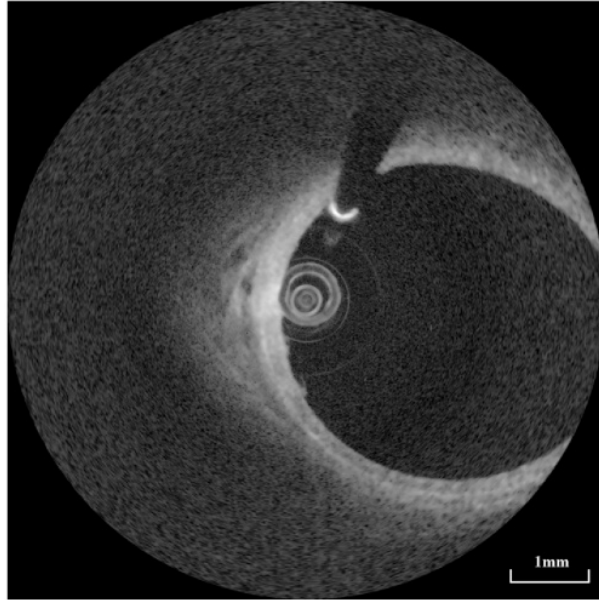


Figure 4.31: Despeckled porcine carotid artery EV-OCT image.

$SNR = 20\log(x_{lin}/\sigma_{lin})$, where x_{lin} is the maximum intensity in the ROI in linear scale. σ_{lin} is the standard deviation of the noise region in linear scale. The contrast-to-noise ratio (CNR) was defined as $CNR = 10\log[(\mu_x - \mu_b)/(\sigma_x^2 - \sigma_b^2)^{0.5}]$, where μ and σ are the mean and standard deviation and subscripts x and b denote the ROI and noise region, respectively. The equivalent number of looks (ENL) was defined as $ENL = \mu_x^2/\sigma_x^2$ and is averaged between three ROIs depicted in Fig. 4.30. An edge preservation parameter is defined previously as in Eq. 4.2 [90].

$$\epsilon = \frac{1}{R} \left(\sum_{r=1}^R \frac{\sum_{(i,j)\in r} (\Delta I - \Delta \bar{I})(\Delta \hat{I} - \Delta \bar{\hat{I}})}{\sqrt{\sum_{(i,j)\in r} (\Delta I - \Delta \bar{I})(\Delta I - \Delta \bar{I}) \sum_{(i,j)\in r} (\Delta \hat{I} - \Delta \bar{\hat{I}})(\Delta \hat{I} - \Delta \bar{\hat{I}})}} \right) \quad (4.2)$$

where ΔI and $\Delta \hat{I}$ are the Laplace edge detection operators performed on the original image I and the filtered image \hat{I} respectively. $\Delta \bar{I}$ and $\Delta \bar{\hat{I}}$ are the mean values in the r th region of interest of ΔI and $\Delta \hat{I}$ respectively. Briefly, the larger the parameter, the more edges are preserved. Figures 4.32(a), 4.32(b), and 4.32(c) show the enlarged views of the ROIs without processing, processed by the I-divergence method [94] and processed by our

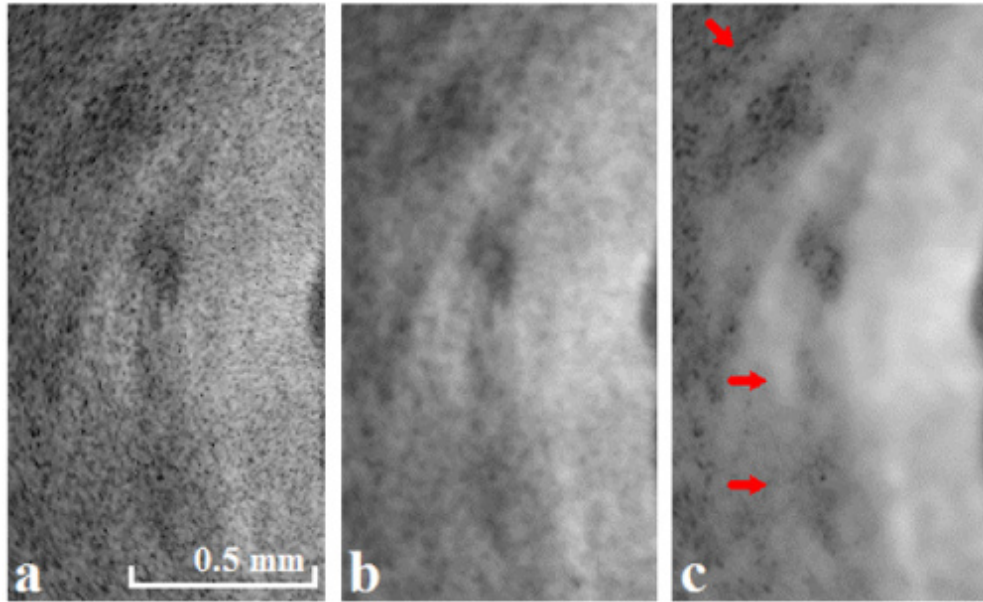


Figure 4.32: (a) Enlarged view of the red ROI in the original porcine arterial wall image; (b) enlarged view of the red signal ROI in the despeckled image processed by I-divergence algorithm; (c) enlarged view of the red signal ROI in the despeckled image processed by our proposed algorithm. The arrows indicate structures that are much less visible in the unprocessed image.

proposed algorithm, respectively. As noted by the arrows in Fig. 4.32(c), visually these structures are very difficult to be discerned in Fig. 4.32(a). Fig. 4.33 shows a region far from the catheter without and with speckle suppression. The result demonstrates that our algorithm can better delineate features, despite the fact that they are located further from the imaging catheter where a diverging optical beam provides less SNR. This also demonstrates our technique is robust against variations in speckle orientation.

Table 4.1 shows the results when $\beta=1.5, 3$, and 4 . In all cases with different β values, the SNR, CNR, and ENL all showed improvement compared to the original image. The result obtained by a 12×12 median filter is also listed. It produces very good SNR, but edges were poorly preserved. To further show how β affects the speckle suppression effect, CNR and edge preservation were plotted against β in Fig. 4.34. When β is less than 3, the CNR is higher but the edge preservation drops, and vice versa when β is larger than 3. Thus, β acts as an adjustable parameter that controls the trade-off between

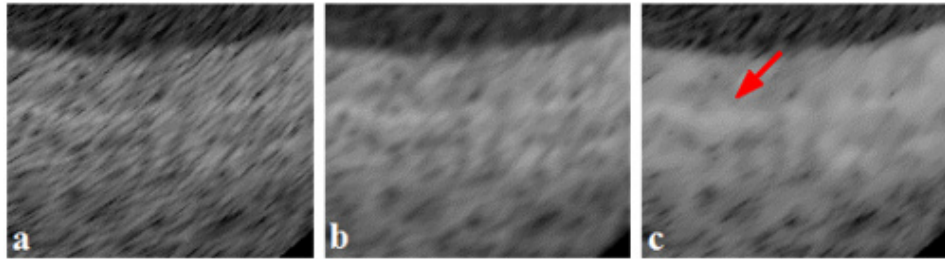


Figure 4.33: (a) Enlarged view of the green ROI in the original image; (b) enlarged view of the green signal ROI in the despeckled image processed by I-divergence algorithm; (c) enlarged view of the green signal ROI in the despeckled image processed by our proposed algorithm. The red arrow indicates the clearer visualization of the external elastic lamina.

	SNR (dB)	CNR (dB)	ENL	Edge Preservation
Original	38.67	2.83	183	N/A
Median (12×12)	45.72	3.91	1211	0.01
$\beta = 1.5$	45.64	3.92	1241	0.28
$\beta = 3$	39.83	3.61	1098	0.54
$\beta = 4$	39.71	3.12	864	0.68

Table 4.1: Metrics Comparison Between the Original Image and Processed Images Using Different β Values

speckle suppression and edge preservation. Such trade-off adjustment is needed when one wants to see different features. For example, when one wants to evaluate large area atherosclerotic plaques, β should be set lower than 3 to apply stronger speckle suppression so as to clearly delineate different parts of the plaque. However, when one wants to see neovascularization, β should be set higher than 3 in order to preserve the vessel edges.

To show that our method does have real benefit in imaging the physiological state of the vessel wall tissues, a set of images taken with the EV-OCT probe in static condition manipulated close to the vessel wall was despeckled and processed with the vasa vasorum detection algorithm listed above. Fig. 4.35 shows the original image, Fig. 4.36 shows the result of speckle reduction. Fig. 4.37 and 4.38 show another set of artery images before and after speckle reduction after blood flows back to the arterial lumen. Fig. 4.39 shows the result processed by our vasa vasorum detection algorithm on Fig. 4.38. When blood flows back to the vasa vasorum in the adventitia after stopping the application of contrast clearing agent, the despeckled image (Fig. 4.38) clearly shows the dynamic

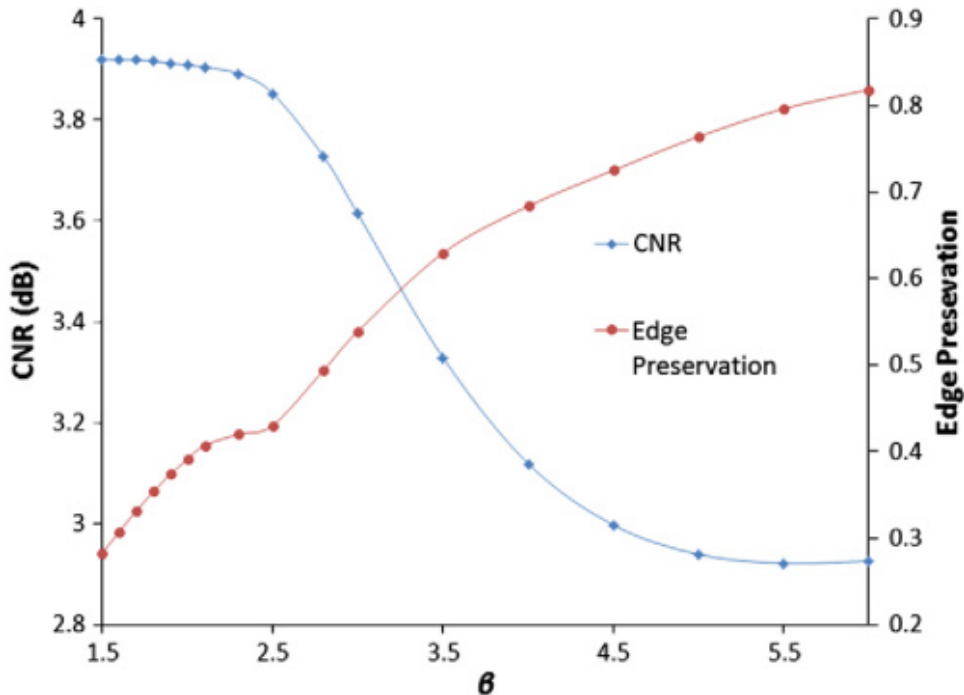


Figure 4.34: Trade-off between CNR and edge preservation by adjustment of β , computed according to Fig. 4.30.

beating and blood flow in response to intravascular pressure change, while in the original image (Fig. 4.37) the dynamic behavior is obscured.

More insight can be drawn with the above results. We observed the interesting phenomenon of vasa vasorum exhibiting either high optical scattering (blood entering the vasa vasorum) or low scattering (complete clearing of blood). High or low scattering translates into high or low OCT image intensity, and in fact the vasa vasorum may exist in these two different states because of the periodic presence of blood, as determined by the saline to blood interface (see Fig. 4.40) in relation to the origin of the vasa vasorum. The interface location dynamically changes as a function of the arterial blood pressure, the vascular resistance, and the injector rate and volume and as a result of the cardiac cycle. In the following images we demonstrate these phenomena as a potential technique to analyze and visualize the vasa vasorum.

Fig. 4.40(a) shows a blood-clearing scheme where a saline flush clears the blood after the opening of a VVI in the vessel wall lumen. Blood could still flow into the VVI and

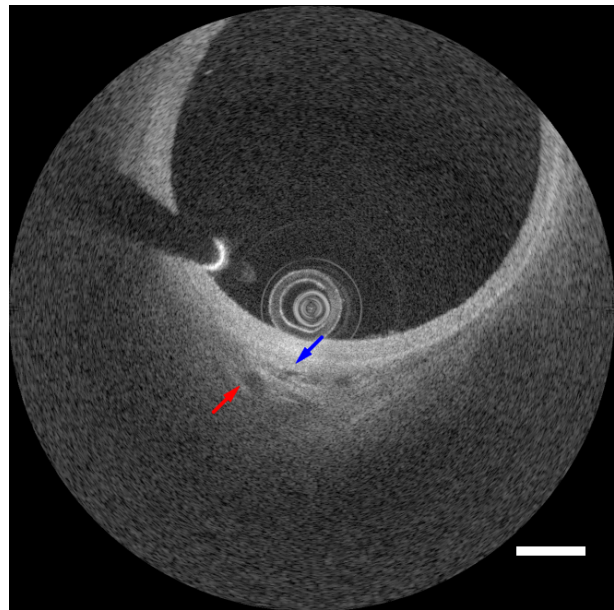


Figure 4.35: Original EV-OCT image of vasa vasorum. Scale bar represents 1mm.

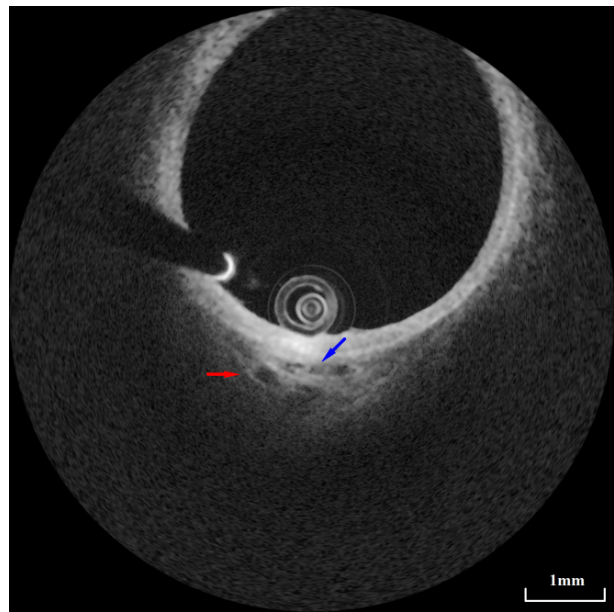


Figure 4.36: EV-OCT image of vasa vasorum after speckle reduction when the major artery was cleared of blood.

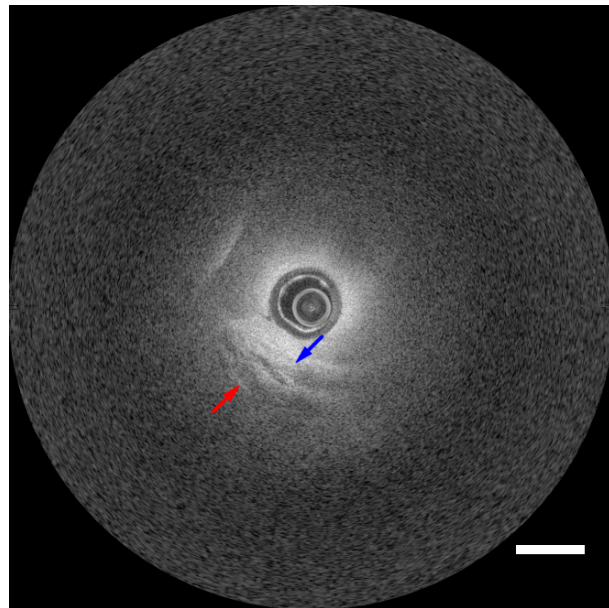


Figure 4.37: EV-OCT image of vasa vasorum before speckle reduction when blood flows back to the major artery lumen. Scale bar represents 1mm.

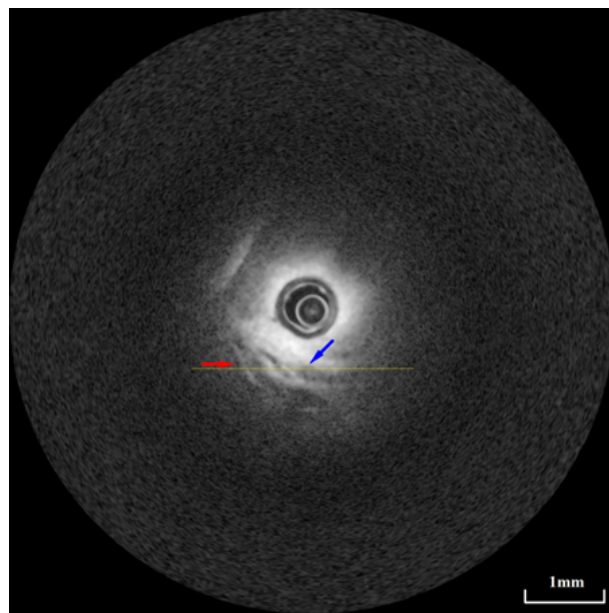


Figure 4.38: EV-OCT image of vasa vasorum after speckle reduction when blood flows back to the major artery lumen.

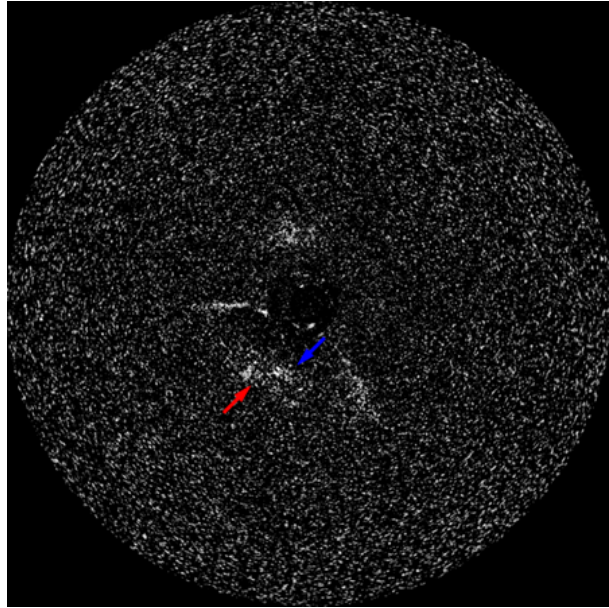


Figure 4.39: Vasa vasorum detection using kurtosis as validation

therefore, when imaged by EV-OCT, blood flow would be present in the image sequence. Fig. 4.40(b) shows a blood-clearing scheme where a saline flush clears the blood before opening of the VVI. This time, only saline can flow into the VVI, therefore, when imaged by EV-OCT, the VVI would appear transparent.

Fig. 4.36 shows one frame of the stationary image sequence when saline flush was injected. As shown in the figure, the blue arrow was a VVI whose blood flow was visualized as in Fig. 4.40(a). The red arrow points to a VVI that was transparent throughout saline flushing, corresponding to Fig. 4.40(b). Fig. 4.38 shows another frame of the stationary image sequence when saline flushing was not enforced. The blue arrow points to the VVI that underwent a surge of blood flow in its lumen. This time, in the VVI pointed by the red arrow, a surge of blood flow in its lumen could readily be observed.

To better visualize the above dynamics, a M-mode (1D intensity change along time) image is shown in Fig. 4.41, taken along the yellow line in Fig. 4.38. The blue and red arrows point correspondingly to those indicated in Fig. 4.36 and Fig. 4.38. The VVI indicated by the blue arrow shows periodic intensity changes throughout the whole

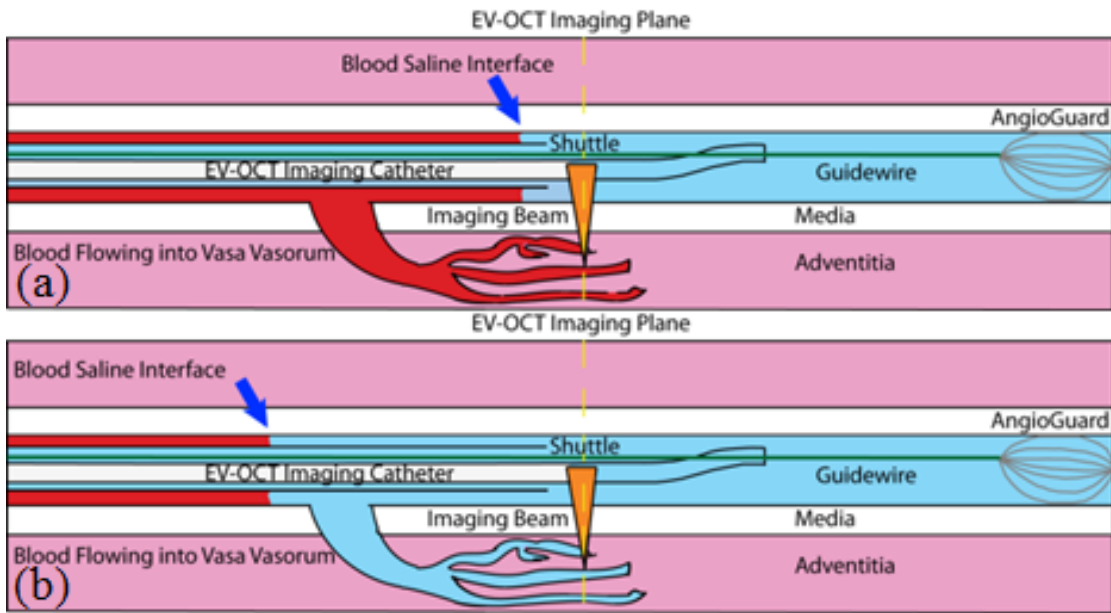


Figure 4.40: EV-OCT vasa vasorum imaging scenario, (a) Scenario of the vasa vasorum indicated by the red arrow in Fig. 4.38; (b) Scenario of the vasa vasorum indicated by the blue arrow in Fig. 4.38.

image sequence, whereas the VVI indicated by the red arrow shows intensity changes only after saline flushing was stopped. The dynamics may play a significant role in the formation of atherosclerosis. Supply to the vasa vasorum may arise from the parent vessel (as shown in Fig. 4.40), or from other blood vessels in the vicinity (which will not be affected by the saline injection process, e.g. VVE) in which case the vasa vasorum OCT signal intensity will remain high. Such difference can allow one to distinguish the arterial supply of the vasa vasorum, which may be beneficial in the study of the origin and impact of vasa vasorum in disease processes such as atherosclerotic plaque or chronic total occlusions [104–106]. EV-OCT with its inherently higher spatial resolution may be complementary to IVUS, especially in the detailed characterization of vasa vasorum, which could be beneficial to the *in vivo* understanding of the atherosclerotic plaques.

Fig. 4.42 and Fig. 4.43 show a human coronary atherosclerotic plaque image before and after speckle reduction respectively (Image from St. Jude Medical).

From the result in Fig. 4.43, the plaque region at 6 o'clock appears much more sharply

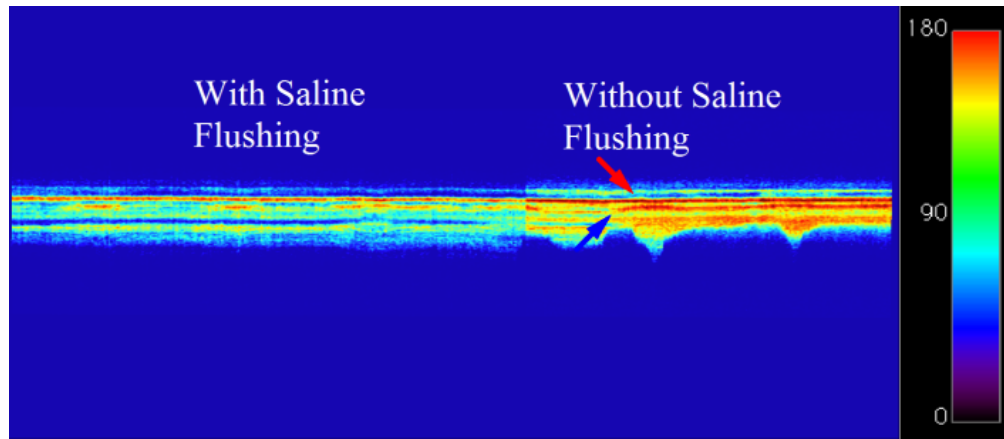


Figure 4.41: M-Mode image of the vasa vasorum as indicated as the yellow line in Fig. 4.38. Please refer to scale of 4.38.

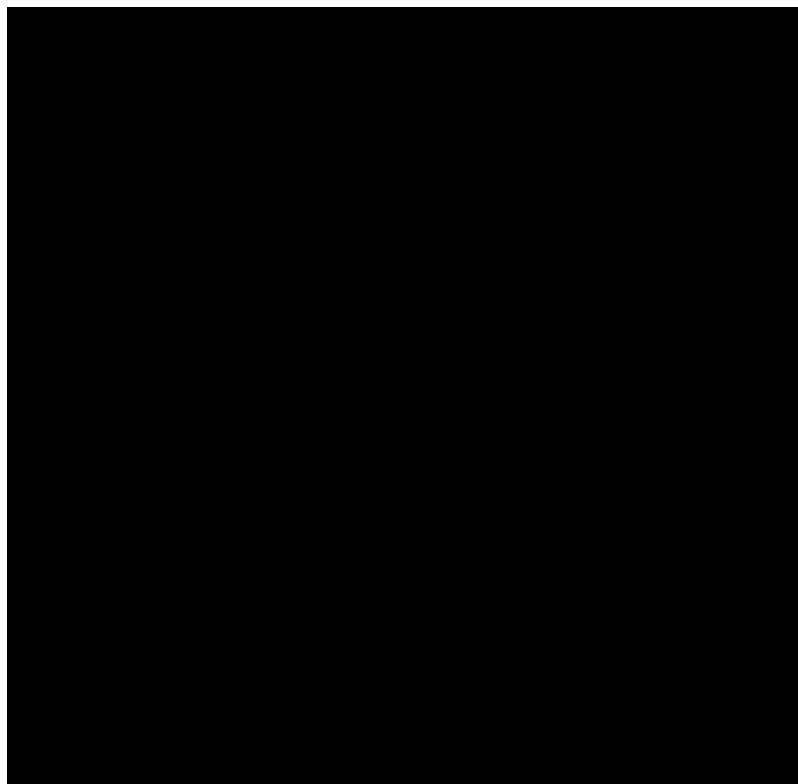


Figure 4.42: Atherosclerotic plaque image before speckle reduction. Scale bar represents 1mm. (Image has been removed due to copyright restrictions.)

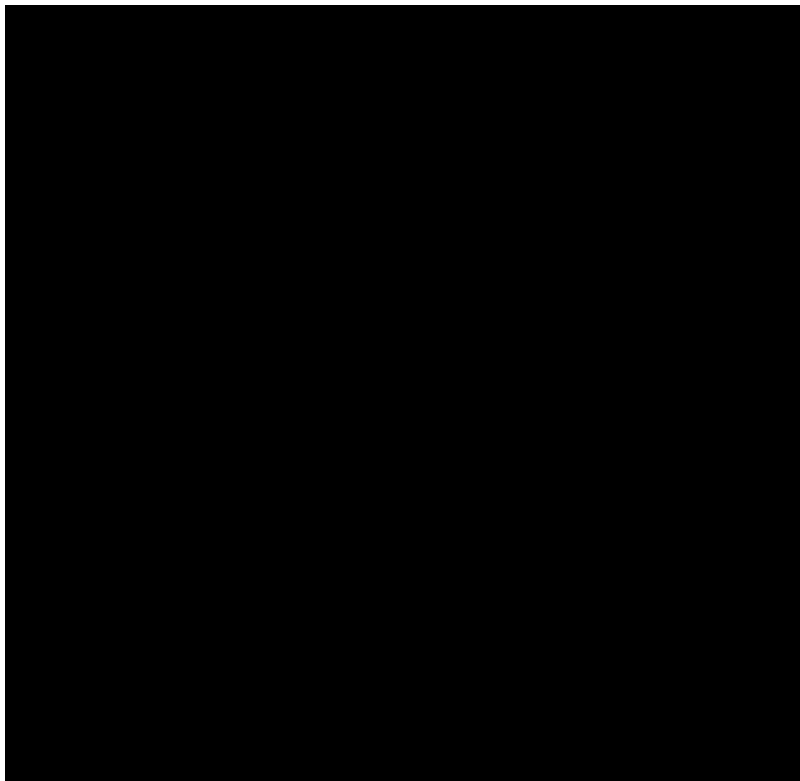


Figure 4.43: Atherosclerotic plaque image post speckle reduction. Scale bar represents 1mm. (Image has been removed due to copyright restrictions.)

delineated and clearer than that in Fig. 4.42. The fibrous cap is much more defined and the details of the micro-calcification region are much more obvious. Although current interpretation of EV-OCT does not entail what these features inside the atherosclerotic plaque are, future research on atherosclerosis may find these results interpretable.

We note that one of the shortcomings is the lack of gold standard reference image u , which is not unique to our technique. Furthermore, the algorithm was run on an Intel Core i5 computer implemented in MATLAB®. Speckle suppression for a 969×969 image took ~ 7 seconds. Future implementation in C++ and/or GPU parallel processing may be required to perform real-time EV-OCT speckle reduction.

We have thus proposed and demonstrated an effective speckle suppression method for EV-OCT images while preserving edge information. Furthermore, to our knowledge, we demonstrated for the first time how speckle reduction can potentially benefit EV-OCT by enhancing visibility of endovascular morphological structures with a computational method.

4.8 Summary of Chapter 4

In this chapter, the feasibility of EV-OCT in the carotid artery of a porcine model was demonstrated. Various scenarios such as vaso spasm, carotid stenting and adventitia microstructure are demonstrated with EV-OCT imaging. Further, a motion mapping algorithm was demonstrated to depict vasa vasorum dynamics in a porcine carotid artery model. Finally, a speckle noise removal algorithm was demonstrated to benefit EV-OCT users in various scenarios such as vasa vasorum inspection and atherosclerotic plaque imaging.

Chapter 5

OCT Micro-Angiography for Hereditary Hemorrhagic Telangiectasia

5.1 Candidate Contribution

The candidate re-aligned the swept source laser of the SS-OCT system. The candidate was involved in the development of nearly 100% of the algorithm. Patient scanning was performed by the candidate. Subsequent publication was prepared by the candidate.

5.2 Depth Enhanced OCT Micro-Angiography

Despite being powerful and simple, one major drawback of svOCT is that the technique is signal strength dependent [107]. Various techniques have been developed to circumvent this drawback, such as logarithmic speckle transformation [107], split-spectrum decorrelation [28], double-decorrelation mapping [108], and so on. Decorrelation techniques, however, require the application of subjectively determined masks. In this study, with the emergence of high speed OCT platforms, a new flow mapping method based on the

time-domain histogram of individual pixels (not to be confused with histogram equalization) is presented. Results demonstrated that this new method can potentially enhance the visualization of deeper blood vessels while being less susceptible to motion and can potentially be employed in skin OCT angiographic study of complex vascular irregularities.

In Ch. 3, various statistical distributions and their corresponding scenarios in OCT microvascular imaging were described (Eq. 3.9, 3.10 and 3.11). To distinguish among these distributions, traditional svOCT calculates the variance estimator to map out the vasculature. Variance for the Rician distribution, however, is dependent on the non-centrality parameter [107], which is one of the contributing factors for svOCT to detect the microvessels. In the Rayleigh regime or low signal regions, however, svOCT signals are substantially weaker. Moreover, svOCT is also sensitive to specular reflection at interfaces. These deficiencies result in nonuniform vessel detection, as is demonstrated in this chapter.

To address these problems, consider normalizing the amplitude axis of the time-domain histogram of each pixel by the minimum and maximum amplitudes with an identical number of bins for every pixel. In this scaleless domain, amplitude distributions can be characterized mainly by their shape but not by the signal strength. To distinguish between different distributions, consider the imaginary parts of the characteristic functions of Rayleigh Eq. 5.1, Rician Eq. 5.2, and Gaussian Eq. 5.3 distributions [109]

$$Im(M(\omega)_{Rayleigh}) = \sigma\omega\sqrt{\frac{\pi}{2}}\exp\left(-\frac{1}{2}\sigma^2\omega^2\right) \quad (5.1)$$

$$\begin{aligned} Im(M(\omega)_{Rician}) &= \sqrt{2}\sigma\omega\exp\left(-\frac{\nu^2}{2\sigma^2}\right) \\ &\times \Psi_2\left(\frac{3}{2}; 1, \frac{3}{2}; \frac{\nu^2}{2\sigma^2}, -\frac{1}{2}\sigma^2\omega^2\right) \end{aligned} \quad (5.2)$$

$$Im(M(\omega)_{Gaussian}) = \exp\left(-\frac{\nu^2}{2\sigma^2}\right)\sin(\mu\omega) \quad (5.3)$$

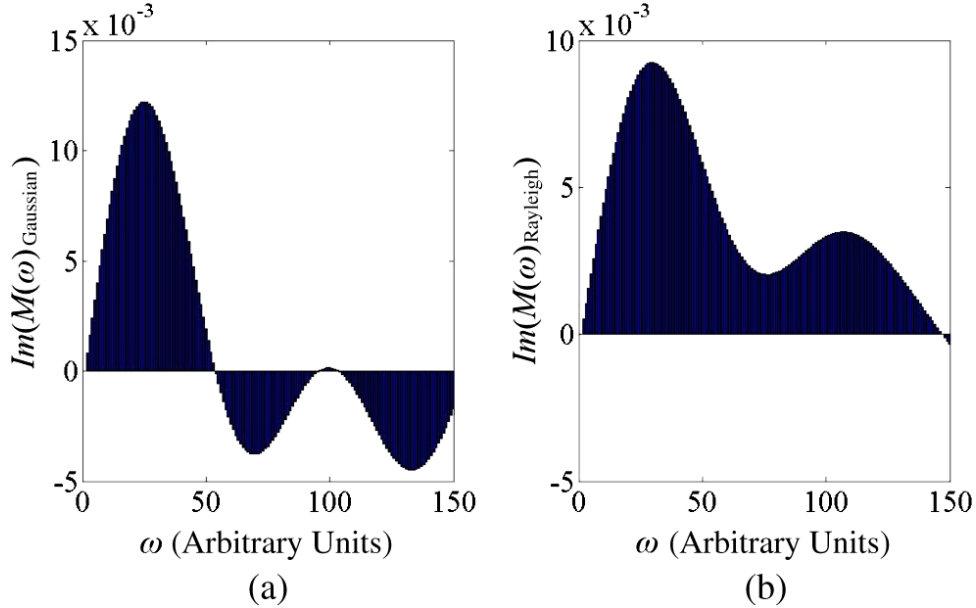


Figure 5.1: (a) $\text{Im}(M)$ of Gaussian distribution; (b) $\text{Im}(M)$ of Rayleigh distribution.

$$\Psi_2(\alpha; \gamma, \gamma'; x, y) = \sum_{n=0}^{\infty} \sum_{m=0}^{\infty} \frac{(\alpha)_{m+n}}{(\gamma)_m (\gamma')_n} \frac{x^m y^n}{m! n!} \quad (5.4)$$

$$(a)_n = a(a+1) \cdots (a+n-1) = \frac{\Gamma(a+n)}{\Gamma(a)} \quad (5.5)$$

where Ψ_2 is one of the Horn's confluent hypergeometric functions, μ is the mean of a Gaussian distribution and Γ is the Gamma function. Notice that Eq. 5.1 and Eq. 5.2 have an exponential decay nature while Eq. 5.3 has an oscillatory nature. In addition, from the form of Eq. 5.1 and Eq. 5.4, the effect of the $\exp\left(-\frac{\nu^2}{2\sigma^2}\right)$ term in Eq. 5.2 can be seen to be partially canceled by the hypergeometric function. Figure 5.1(a) shows a typical $(M(\omega)_{\text{Rayleigh}})$ and Fig. 5.1(b) shows a typical $\text{Im}(M(\omega)_{\text{Gaussian}})$ in sample OCT data. By integrating $\text{Im}(M)$ from $\omega = 1$ to 150 , Rayleigh and Rician distributions can be distinguished from Gaussian distributions.

To test this proposed method, a phantom consisting of both solid and liquid phases of Agarose with 2% titanium dioxide was prepared. The liquid phase was stirred to induce scatterer flow. A Thorlabs (Newton) OCT system in the 1300 nm range with 16 kHz A-scan rate and 100 nm bandwidth was used to acquire the B-mode sequence of the

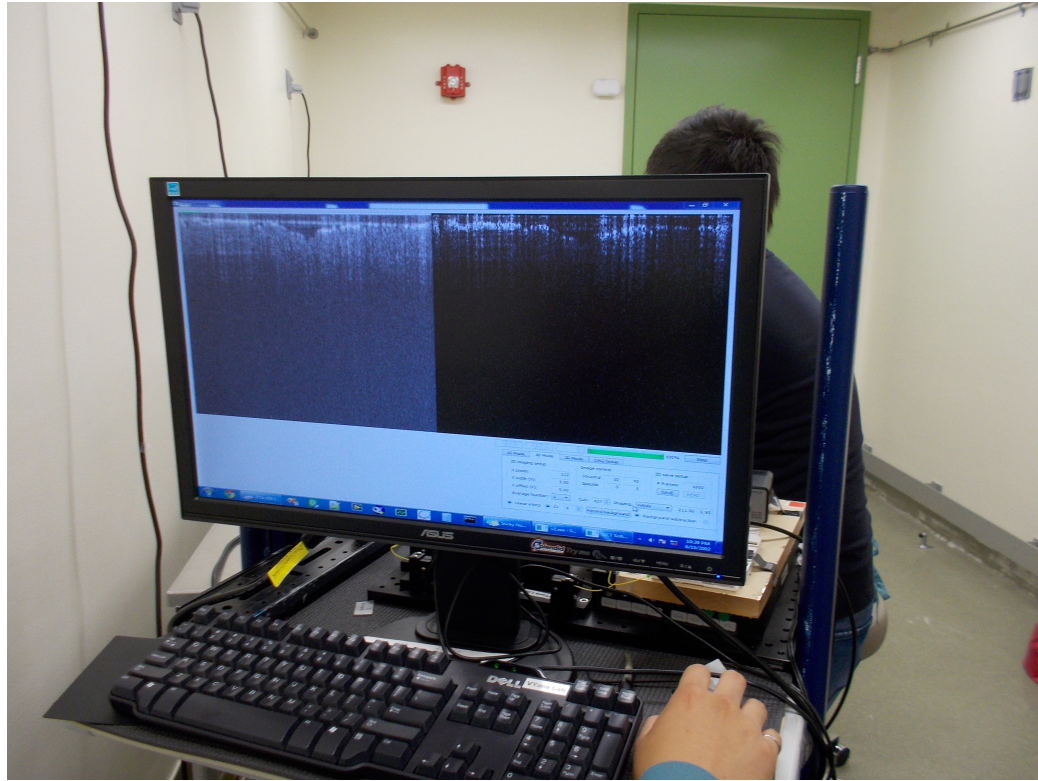


Figure 5.2: Interface used for HHT imaging.

phantom over a 1mm width. For in vivo imaging, human dorsal hand skin regions were imaged by a 1300nm spinning polygon buffered swept source laser system with a 108 kHz A-scan rate and a 95 nm bandwidth over a $3 \times 3\text{mm}^2$ area. Patients' skin was gently pressed against a microscope slide to minimize macro motion, while real-time speckle variance was observed to make sure there was the least possible disturbance to blood flow, the interface of which is depicted in Fig. 5.2. All procedures were approved by the St. Michaels Hospital (Toronto, ON) Research Ethics Review Board.

After image acquisition, the data were imported into MATLAB® for postprocessing. In each B-frame, a 30×30 pixels noise area was first selected, which in essence can be fixed at the bottom part of the image which always consists of noise. The root-mean-square value of this noise area was subtracted from each B-frame and thresholded above zero. $N = 15$ frames were then used to generate a histogram normalized by the minimum and maximum with 15 bins. A 1024 point inverse fast Fourier transform (iFFT) was

then performed on the histogram to obtain the characteristic functions $M(\omega)$. The imaginary part $Im[M(\omega)]$ was then taken out and the following contrast metric $S(x,y)$ was computed:

$$S(x,y) = \int_0^a Im[M(x,y,\omega)]d\omega \quad (5.6)$$

where a was empirically chosen to be 150 to avoid high frequency noise resulting from interpolation performed in 1024 point iFFT and (x,y) represents the spatial location of a B-scan cross section. The resultant map was filtered by a circular disk averaging filter of a radius of 3 pixel and finally thresholded by subtracting the median of the upper half of the map.

5.3 Experimental Setup

A commercial dermatologic OCT system (VivoSight, Michelson Diagnostics) was used for B-mode imaging of a healthy volunteer's fingernail root. The A-scan rate is 10kHz and thus this data set is for trial purpose only.

Fig. 5.3 shows the schematic of the OCT system used for skin angiography. The laser, data acquisition and software were specifically designed to enable continuous real-time processing and display of both structural and speckle variance data while simultaneously saving recalibrated fringe data at an A-scan rate of 108 kHz. The swept source laser design is a buffered polygon telescopic filter ring cavity laser where a 600 lines/mm diffraction grating (GR25-0613, Thorlabs) was used to create the necessary dead time between laser sweeps to enable buffering from 54 kHz to 108 kHz. The analog signals were fed into a data acquisition system and digitized at 250 MS/s (ATS9350, Alazartech), which was transferred to the memory on a video graphics card (GeForce GTX 460 1GB, NVIDIA). Custom-written kernels together with built-in CUDA libraries were used to manipulate and reconstruct structural and speckle variance OCT images on the multiple

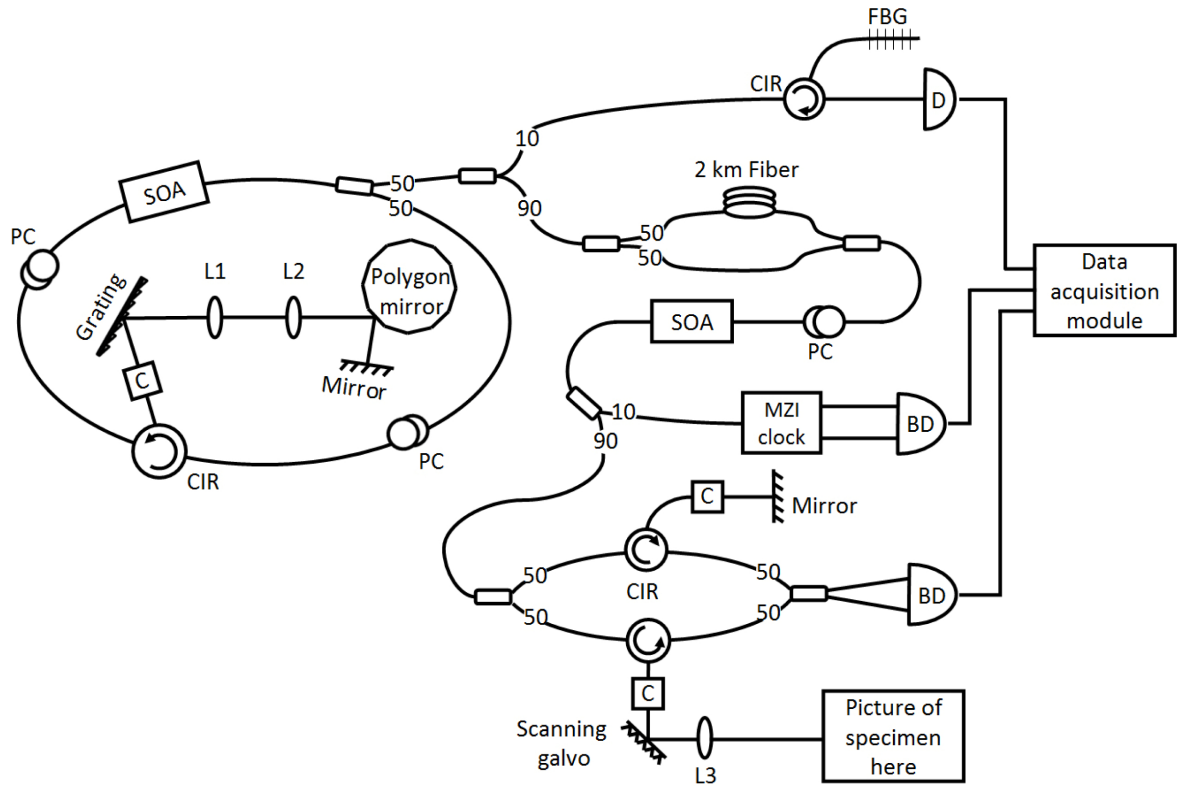


Figure 5.3: Schematic of OCT setup for skin microangiography, BD: Balanced Detector, C: Collimator, FBG: Fiber Bragg Grating, MZI: Mach-Zehnder Interferometer, L1-L3: Lenses, PC: Polarization Controller, SOA: Semiconductor Optical Amplifier, reproduced with permission from [110].

cores of the GPU, which enables massive parallel data processing. The setup allows real-time acquisition, processing, and display, only limited by the A-scan rate of the laser [5]. Real-time display was used to ensure the data acquired was correctly positioned and of sufficient quality.

The advantage of using a polygon filter cavity is that, unlike a traditional Fabry-Perot cavity filter, the laser sweeps are unidirectional, i.e. from shorter to longer wavelength or vice versa. This helps ensure the uniformity between A-scan and minimize the chance of alternating A-scan quality, which can severely degrade the results of our proposed method. However, Polygon swept source lasers in general have a complicated relationship between their coherence length and alignment, thus they tend to have shorter coherence lengths and slightly shorting ranging depth.

5.4 Phantom Results of Depth Enhanced OCT Micro-Angiography

Fig. 5.4(a) shows the structural image of the Agarose phantom. The left side was the solid phase and the right side was the randomly flowing fluid phase, indistinguishable from the structural image. Figure 5.4(b) shows the corresponding svOCT image ($N=4$) and Fig. 5.4(c) shows the image processed by our new proposed algorithm. Figure 5.4(d) shows the plot along the yellow line in Fig. 5.4(b) (svOCT), and Fig. 5.4(e) shows the plot along the yellow line in Fig. 5.4(c) (proposed algorithm). The deeper portion of the TiO_2 suspension movement was clearly enhanced in Fig. 5.4(c). Also, the interface of the two phases (green arrow and Rician zone) in Fig. 5.4(b) is significantly stronger than the central area of the fluid zone, whereas in Fig. 5.4(c), both zones have equal brightness, demonstrating the intensity insensitivity of the new algorithm. Contrast scaling was determined from the phantom results and applied to all subsequent *in vivo* imaging results.

5.5 Hereditary Hemorrhagic Telangiectasia

Hereditary Hemorrhagic Telangiectasia, or Osler-Weber-Rendu syndrome, a type of genetic vascular disease as mentioned in Ch. 2. is a disorder which involves the development of telangiectases and arteriovenous malformations in specific organs. The symptoms are not obvious. The most common features include nosebleeds and telangiectases on the lips, fingers and oral mucosa [111].

Arteriovenous malformations are vascular networks that lack the capillary beds which results in direct connections between arteries and veins. Smaller malformations are called telangiectases ($\sim 1\text{-}2\text{mm}$ in diameter) and they are most often found on the lips, tongue, face, fingers and respiratory and gastrointestinal mucosa. Their vessel walls are thin and

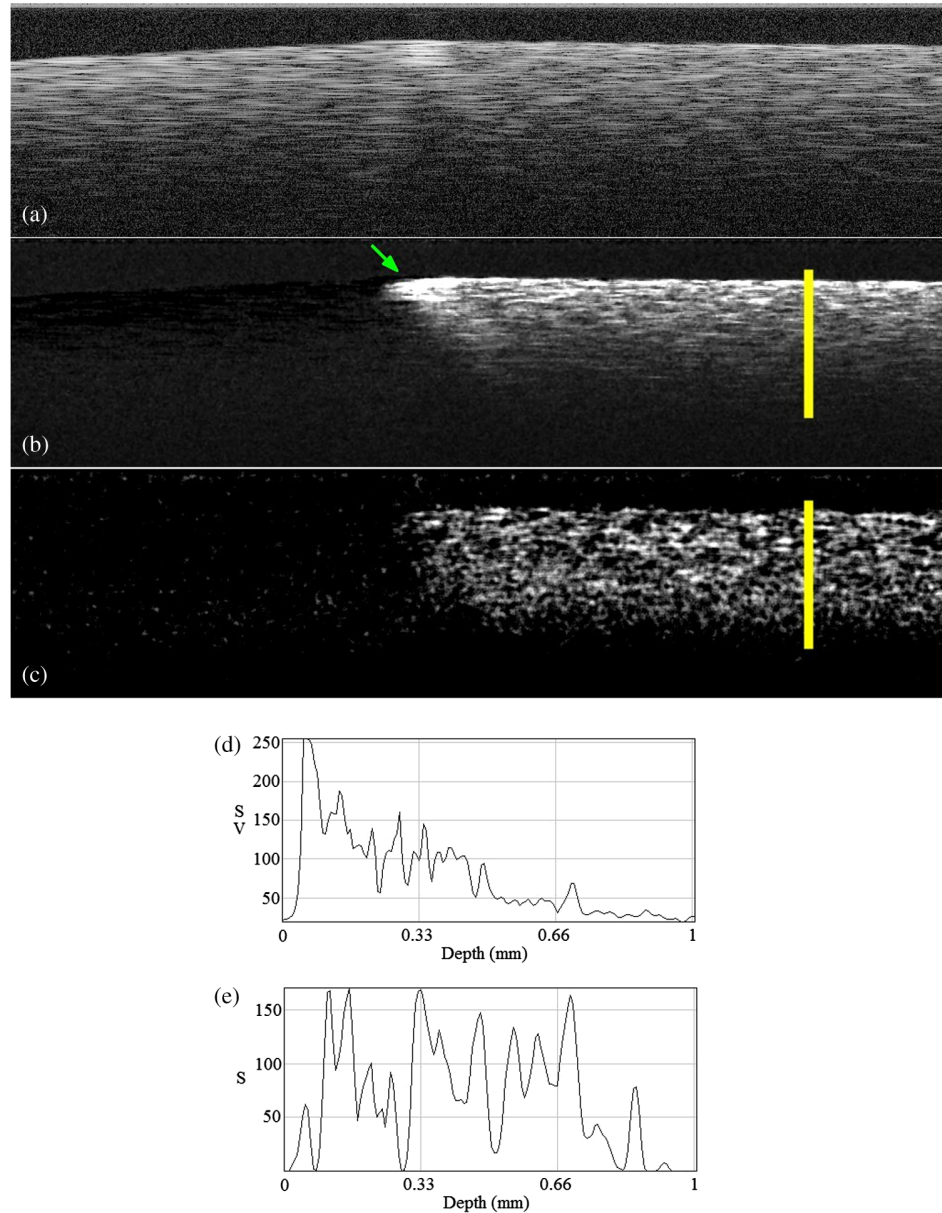


Figure 5.4: (a) Structural image of the Agrose phantom (1 mm by 1 mm); (b) corresponding svOCT image, (c) image calculated by our proposed algorithm, (d) plot of the depth profile along the yellow line in (b), (e) plot of the depth profile along the yellow line in (c).

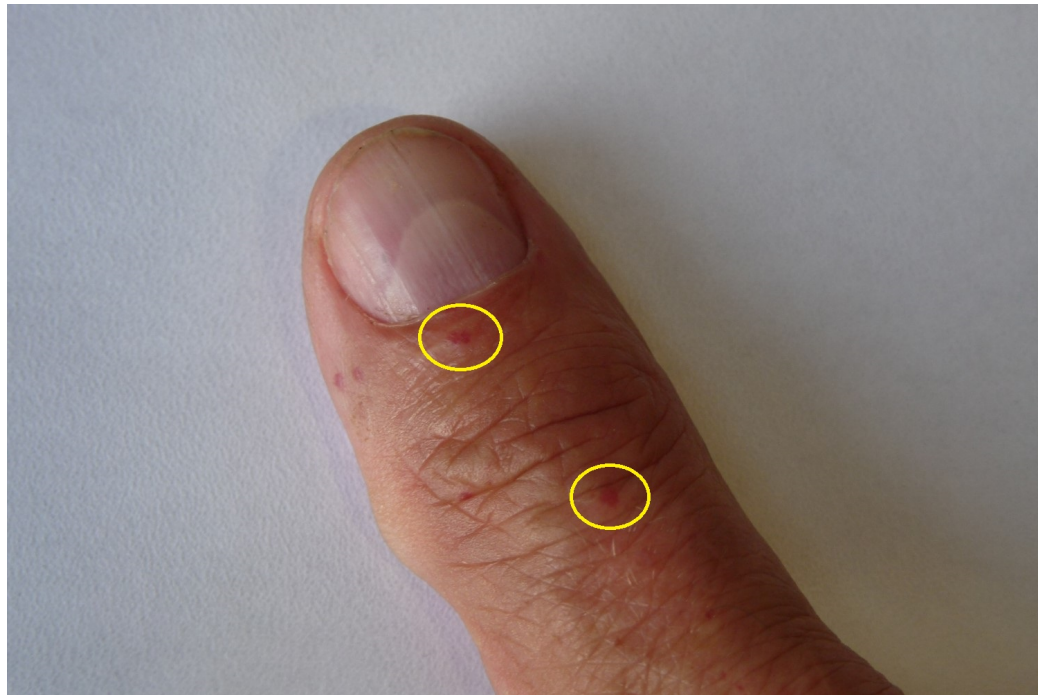


Figure 5.5: Human HHT skin lesion (Circled).

can blanch under pressure. Combined with their proximity to the skin surface and their tortuous nature, they are very easy to bleed and since they are directly connected to arteries, the bleeding can be difficult to quell [111]. An example photograph of human HHT lesion on the fingers is shown in Fig. 5.5.

Larger arteriovenous malformations can typically be found in the brain and lungs. They can be up to several centimeters in diameter. These lesions give rise to complications mainly due to blood shunting directly from arteries to veins, resulting in increased cardiac output and desaturation of blood and venous emboli shunting in the lungs [111].

Current clinical diagnosis includes recurrent nosebleeds, blanchable telangiectases in the aforementioned areas, visceral arteriovenous malformations and family HHT history [111].

Thus, it is key to map out these telangiectases and arteriovenous malformations using non-invasive imaging methods. Currently, these lesions can only be imaged using whole body imaging modalities such as CT and MRI. They are capable of imaging larger arte-

riovenous malformations in the lung and brain but they do not possess enough resolution to map out the details of these malformed vessel networks. Thus OCT presents an opportunity to image the smaller telangiectases *in vivo* to gain more insight into the diagnostic and therapeutic approaches of HHT. Indeed, Doppler OCT has been attempted on HHT lesions, however with only B-mode evaluations [112].

Observation and characterization of the malformed microvessel network of the HHT lesions are important in two ways. Detailed observation of their progression can allow us to understand the factors contributing to their development and the ways with which they can develop. Monitoring their morphologies during their treatment can also allow us to design better strategies that can be used to treat HHT lesions in the other body parts.

5.6 Initial Demonstration of In Vivo Monitoring of Skin Abnormal Vasculature of HHT patient

Fig. 5.6(a) shows a B-mode image of a healthy fingernail root. Fig. 5.6(b) shows the speckle variance processing of the data set. Fig. 5.6(c) shows the microvessel mapping using our proposed algorithm. Comparing Fig. 5.6(b) and 5.6(c), our proposed method clearly generates a better microvessel B-mode map with more uniform signal across different depths below the skin surface and less motion artifacts.

Fig. 5.7(a) shows the structural image of an *in vivo* human fingernail root of a healthy volunteer, where blood vessels are abundant (9000 B-Scans with 512 A-Scans each). Fig. 5.7(b) shows the corresponding vascular map projection using svOCT. Fig. 5.7(c) shows the corresponding vascular map projection calculated by our proposed algorithm. The shadowing line is likely caused by protrusion of the epidermal tissue. Since current state-of-the-art vascular mapping algorithms are mostly sensitive to motion, and svOCT is sensitive to signal degradation, there are frequent appearances of band-like artifacts in

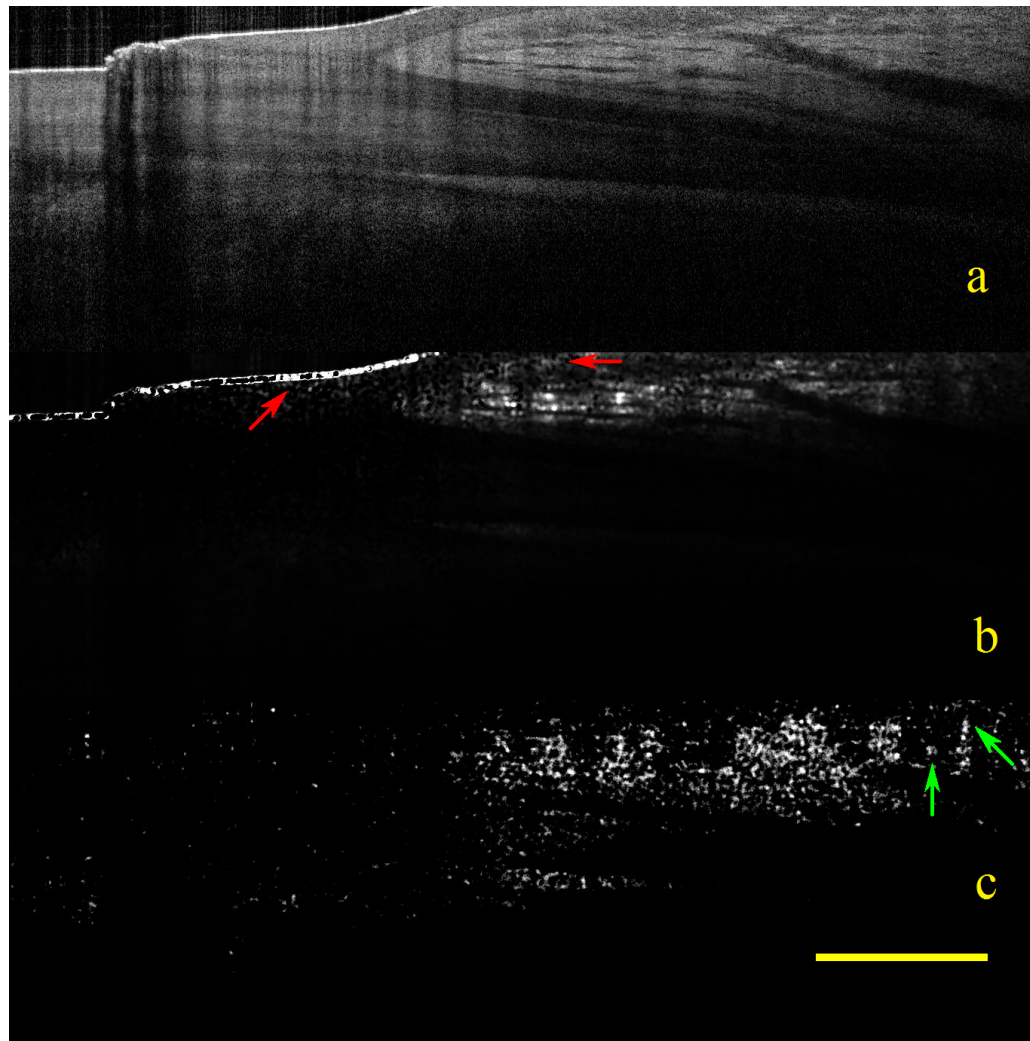


Figure 5.6: B-mode angiography of healthy fingernail root. (a) Structural image; (b) svOCT processing; (c) Depth Enhanced Microangiography; The red arrows point to areas which show motion artifacts. The green arrows point to microvessels which have much higher visibility in (c). Scale bar represents 1mm.

the projection map and some of the small vessels are obscured, despite high speed swept source laser systems. Fig. 5.7(d) shows the structural image of an *in vivo* skin image of a vascular lesion (telangiectasia) in a patient with hereditary hemorrhagic telangiectasia (HHT) (5000 B-Scans with 512 A-Scans each), where the colored boxes indicate the different depths of the projection images created in the subsequent subfigures with matching colors (Figs. 5.7(e), 5.7(g), and 5.7(i) for svOCT and Figs. 5.7(f), 5.7(h), and 5.7(j) for our proposed algorithm). Figs. 5.7(k) and 5.7(l) are the combined projections corresponding to svOCT and our proposed method, respectively. HHT is a genetic disease characterized by the presence of densely packed dilated microvessel networks, including telangiectasia of the skin and mucosa. In Fig. 5.7(l), there is evidence of an increased size of the blood vessels compared to normal ones [Fig. 5.7(c)]. Moreover, the motion artifacts and signal degradation are partially reduced in our proposed algorithm, as shown in Figs. 5.7(c) and 5.7(l), where the blurry effect of the vessels disappears. Figure 5.7(g) shows histopathology of the resected telangiectasia from the same patient, which shows an area of densely packed blood vessels, which are mainly venules together with some larger arterioles as depicted in the OCT projection images. Differences between Figs. 5.7(l) and 5.7(m) can be attributed to the collapse of the microvessel channels in the *ex vivo* state in the absence of arterialized intravascular pressure in these abnormal channels.

Fig. 5.8 shows another HHT lesion (5000 B-scans with 512 A-scans each). Figure 5.8(a) shows the structural image of the HHT lesion and Figs. 5.8(b) and 5.8(c) show the projections of the lesion processed by our proposed algorithm with the colors indicating different depths as depicted in Fig. 5.8(a) at two time points 4 weeks apart. In both of the images, the surrounding normal vessels are shown feeding into the central plexus of the microvessels of the malformation. The plexus of the microvessels is clearly demonstrated at both time points, although the vessel network appears denser and more complex at the later time point.

Fig. 5.9 shows an HHT lesion over the course of 2 months undergoing a certain

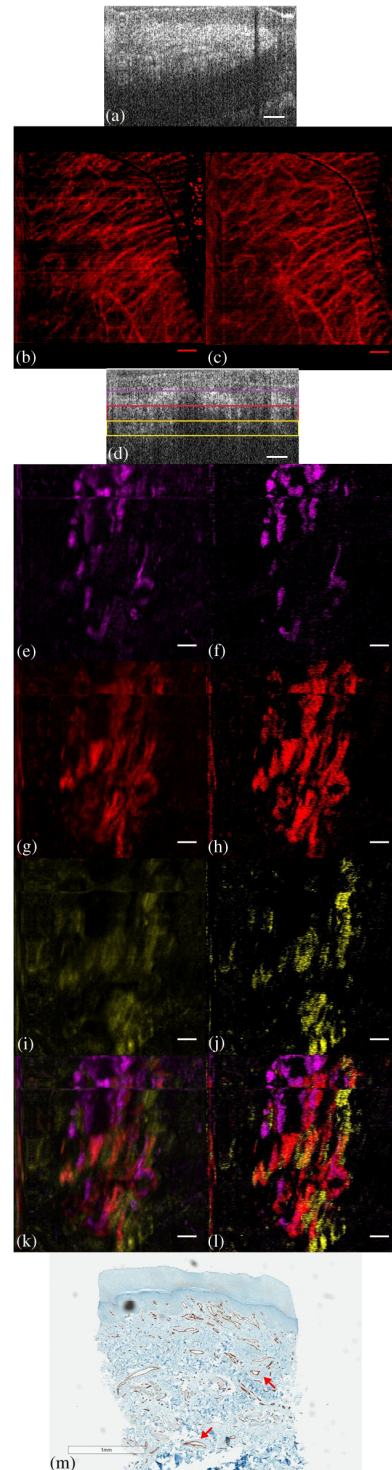


Figure 5.7: (a) Structural image of in vivo healthy human volunteer fingernail root (3 mm lateral by 1.25 mm axial); (b) corresponding svOCT projection of the same area; (c) corresponding projection image of human fingernail root calculated by our proposed algorithm; (d) structural image of in vivo human HHT skin telangiectasia (3 mm lateral by 1 mm axial); (e), (g), (i) projection by svOCT as indicated by the colors in (d); (f), (h), (j) projection by our proposed method as indicated by the colors in (d); (al) scale bars represent 300 μ m; (m) histopathology of the HHT lesion, CD34 staining demonstrating the abundant dilated microvessels. The red arrows point toward an example of dilated arterioles.

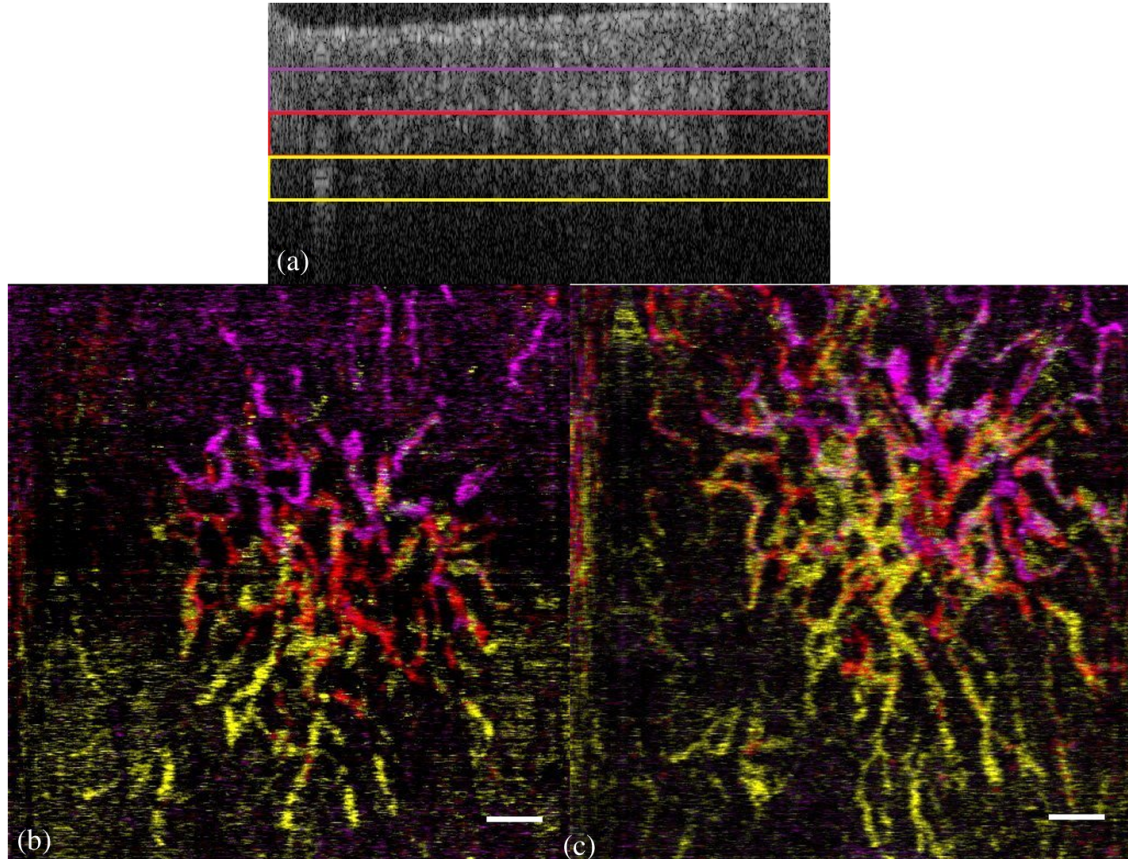


Figure 5.8: (a) Structural image of another HHT lesion (3 mm lateral by 1 mm axial), (b) corresponding projection processed by our proposed algorithm, (c) projection of the lesion 4 weeks after (b). Different colors represent the different depths as depicted in (a). Scale bar represents 300 μm .

treatment. Visible changes are noticeable in the series of images over the course of treatment. Vessel number and sizes have all considerably changed.

Fig. 5.10 shows another treated lesion. It has also shown considerable improvement over the course of treatment.

5.7 Advantages, Limitations and Potentials of Depth-Enhanced OCT Micro-angiography

Our method, as demonstrated in the phantom study, has the potential to map out deeper flow or dynamically moving particles located in regions of low OCT signal strength. Our HHT imaging results also show that our proposed algorithm can potentially map out the morphology of complex diseased microvascular network with higher fidelity and accuracy (Fig. 5.5) due to more uniform mapping in all areas by the normalized nature of the histograms. This allows us to distinguish the shape of the histograms based on their characteristic functions.

Our method also does not require the application of subjectively determined masks, which can vary in a case-by-case basis. However, since background noise also follows the Rayleigh distribution, an additional step to threshold out the background noise needs to be performed. Nevertheless, this subtraction is calculated by the root-mean-square power of the noise region and therefore is not dependent on the judgment at the operator.

Moreover, unlike most other vascular imaging methods in OCT, our method is less sensitive to motion, since for small motions the pixels in the flowing and static regions still correspondingly exhibit the characteristic histogram features. To limit motion, dermatologic OCT data are often acquired with limited physical restriction of the imaging area as in our case. However, patients can still exhibit involuntary tremor, especially internal tissue motion, which is severe in older patients. Moreover, over-restriction will cause the patient discomfort and also prevents blood flow in some of the compressed

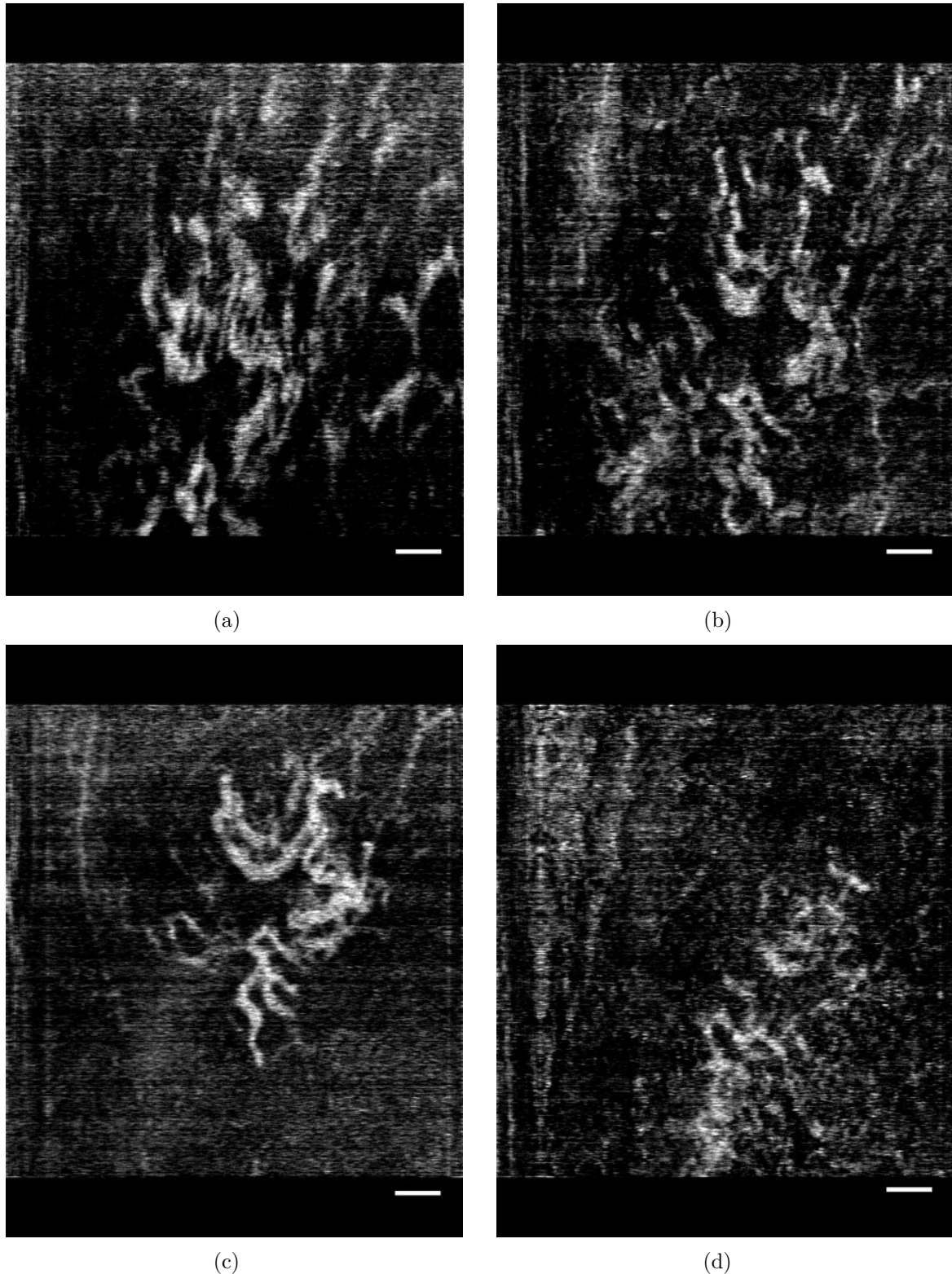


Figure 5.9: a) Treated HHT lesion 1, week 1; b) Treated HHT lesion 1, week 3; c) Treated HHT lesion 1, week 5; d) Treated HHT lesion 1, week 7. Scale bar represents 300 μ m;

vasculature. Sparse and rapid data acquisition is another way to mitigate motion effects; however, this may limit the data available for structural and other methods of analysis. Our method can also mitigate the dependence on sophisticated adaptive optics systems.

One drawback of the method is that more frames are required than with the traditional svOCT or correlation methods. However, these constraints can most likely be mitigated in the near future with the advent of high speed OCT systems which can reach up to 1.6 MHz A-scan rate [113]. Processing can also be dramatically sped up by the use of massively parallel GPU computing [5], which is readily available in many computer systems.

There are alternative ways of imaging microvasculature such as laser speckle imaging. While similar to OCT in nature, laser speckle imaging is simpler and equally effective in microcirculation imaging and the measurement of decorrelation characteristics can even yield quantitative perfusion information regarding the tissue of interest, although it is limited in depth [114]. Thus, while laser speckle imaging can help clinicians perform detailed diagnostics about surface vessels, our OCT technique, designed to give an accurate depiction of deeper microcirculations, can complement laser speckling imaging to enable a more comprehensive overall diagnosis of complex vascular lesions. In addition, a multimodal imaging approach can potentially be an effective way of achieving simultaneous acquisition of functional and molecular information regarding microvasculatures [115], paving the way for one-stop optical diagnosis.

There have been very few studies to date describing the microvascular structure of telangiectasia in HHT. Braverman *et al.* studied the HHT lesions from excised human biopsy tissues [116] and some studies have created HHT animal models and extensively imaged HHT affected mouse brains with intravital microscopy and hyperspectral imaging, in conjunction with immunohistochemistry [117,118]. With our technique, an *in vivo* description of the lesions can hopefully provide noninvasive insight into the structure of the malformations and allow us to carry out a time-lapse study of the lesion dynamics as

well as changes in lesion structure with therapeutic interventions, just as shown in Fig. 5.7 and Fig. 5.8. Studies with larger sample sizes and patient variability can be carried out in the near future with our proposed method in order to give a more accurate picture on the effect of HHT therapeutic intervention.

A previous study has investigated the possibility of analyzing the speckle contrast of time-varying speckle to quantify the flow of scatterers [119]. Further research of our proposed method may enable high fidelity quantitative perfusion microangiography of complex malformed microvessel networks.

5.8 Summary of Chapter 5

A depth enhanced OCT microangiography algorithm was proposed and demonstrated on a genetic vascular disease, HHT. Results show that the proposed method can potentially be used for deciphering the morphologic characteristics of complex malformed microvascular networks, and thus for therapeutic progress monitoring of lesion treatment.

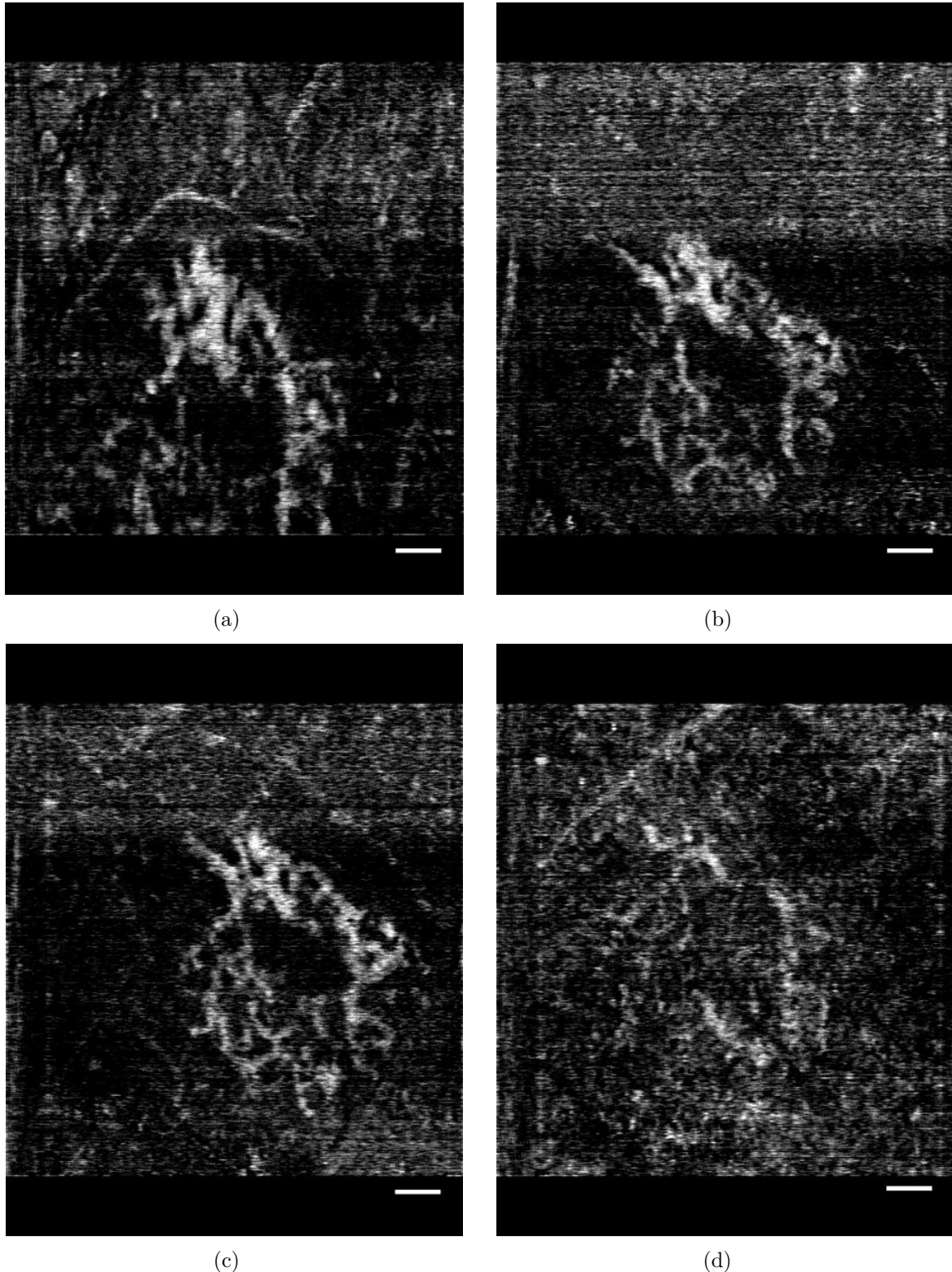


Figure 5.10: a) Treated HHT lesion 2, week 1; b) Treated HHT lesion 2, week 3; c) Treated HHT lesion 2, week 5; d) Treated HHT lesion 2, week 7. Scale bar represents 300 μ m;

Chapter 6

Discussion, Summary and Conclusions

6.1 Discussion and Impact of the Work

As described in Ch. 4, to our knowledge, the first porcine carotid EV-OCT experiment was demonstrated. Along with other endeavors from other research groups around the world, EV-OCT had proven to be safe and effective in cerebrovascular diagnosis and intervention. None of the procedures result in any severe complications. Healthy, diseased and stented arteries were imaged with state-of-the-art EV-OCT. The results have shown that EV-OCT can differentiate the normal layered structures of healthy arteries and vessel conditions/complications during interventional procedures (i.e. clot formation, vaso spasm and stent malapposition, etc.) Such unprecedented work enables a whole new domain of endovascular OCT as it can be extended to the carotid artery imaging market, allowing safer and more accurate evaluation of cerebral stenting and carotid endarterectomy. For instance, we have extensively demonstrated clot formation in the stented carotid artery, which can cause thrombo-embolism in the clinical scenario and can be a fatal condition. EV-OCT imaging immediately after stenting is key to evaluating

the stenting procedure, making prompt remedial actions possible, for example, in the case of clot formation, surgeons can promptly increase heparin (an anti-coagulant agent) loading to the patient to try to mitigate clot deposition on the stented vessel wall. Such evaluation was not possible before in whole-body imaging modalities such as computed tomography and magnetic resonance imaging. Even with IVUS, the resolution is not capable of providing such detailed visualization of the vessel wall conditions.

Other than proving the safety and efficacy of carotid EV-OCT procedures, we took a further step by performing a preliminary attempt of functional imaging using EV-OCT by time-mapping the dynamics of vasa vasorum of porcine carotid arteries. We have utilized a higher order statistics, kurtosis, to map out motion areas in an indirect way to detect the dynamic beating motion of the vasa vasorum in response to changes in intravascular pressure. Although EV-OCT has been restricted to anatomical imaging at the moment, the possibility of other functional utilities cannot be ruled out. Anatomical features such as lipid deposit, fibrous caps and calcification can certainly tell doctors the state of the atherosclerotic plaque. However, more research is still needed in regard to how the disease progresses and what are the factors, both external and internal to the plaque, that contribute to its progression. In particular, the roles of the neoangiogenesis inside the plaque and the vasa vasorum in the adventitia are still poorly understood. By piloting our initial studies on the dynamics of the vasa vasorum, more research can hopefully be done in regard to the functional role of these vessels in the formation and progression of atherosclerotic plaques. For example, the necrotic area and the actively expanding areas maybe indirectly distinguished by the activity and amount of vasa vasorum in the vicinity of the plaque or soon-to-be plaque.

As far as EV-OCT can tell the different layered structures in a normal vessel structure and in atherosclerotic plaques, the structures beneath the external elastic lamina are still obscure in EV-OCT images. The adventitia contains numerous vasa vasorum and are vital to delivering nutrients to the vessel walls and removing waste. The low SNR in

these areas make anatomical interpretation difficult. Moreover, the additional effect of speckle further obscure the structures. We have, therefore, developed an optimized speckle reduction method for EV-OCT images. The major advantage of our method is that while speckle patterns obscuring the structures have been eliminated, the edges between each structure was well preserved. The excellent denoising results can potentially enable physicians to interpret EV-OCT atherosclerotic plaque images beyond the usual depth down to the adventitia area. This is important for both clinical and research scenarios because the deeper we can see into the tissue structure, the more information we can get regarding the physiologic state of the vessel wall tissues. The EV-OCT scenario is unique in the sense that such speckle and noise reduction is impossible via instrumentation manipulation, which leaves digital denoising the only way to improve image quality. We have also shown that our method can run as fast as 7 seconds per image in MATLAB®. Since our method is inherently matrix based, implementation with GPU massively parallel processing can dramatically speed up the algorithm, and thus real time display of the despeckled images is possible, making diagnosis both fast and more reliable.

Finally, we have also developed an algorithm for depth enhanced optical coherence microangiography. In dermatologic OCT, skin lesions can readily be imaged since they are often superficial. However, they are often more than 1mm deep and invade all the way towards the dermis. Although structural OCT can often penetrate up to 2mm deep, at such depths microvessel signals are often very weak. As such traditional Doppler OCT and svOCT, which are SNR dependent, do not generate very good results at such depths. We have developed and demonstrated a new method to mitigate the effect of SNR dependence, enabling clearer visualization of deeper vessels when projection images are rendered. We have thus pushed further towards the limit of OCT microangiography. Moreover, our method upon further development may finally enable quantitative speckle based flow/perfusion imaging.

6.2 Summary

In conclusion, we have developed a set of digital methods for OCT vascular imaging, that can potentially make disease diagnosis, therapeutic monitoring and functional imaging faster, more accurate and more informative. In this thesis, the feasibility of EV-OCT imaging of the carotid artery was first tested and demonstrated in a porcine model. The ability of EV-OCT to resolve different anatomical structures of the carotid artery in different ways was also shown and an efficient speckle reduction method for carotid EV-OCT was also demonstrated. Meanwhile, a depth enhanced OCT micro-angiographic method has been proposed and demonstrated for speckle based flow mapping, which may enable a better understanding of speckle behaviour in different flow conditions.

The results of this thesis has been published in 4 journal papers: 1 journal paper in Biomedical Optics Express, 1 journal paper in Optics Letters and 2 journal papers in Journal of Biomedical Optics. 2 conference papers were also published. Below details the publication list:

Refereed Journals:

1. **Kyle H. Y. Cheng** ; Adrian Mariampillai ; Kenneth K. C. Lee ; Barry Vuong ; Timothy W. H. Luk, et al., "Histogram flow mapping with optical coherence tomography for in vivo skin angiography of hereditary hemorrhagic telangiectasia", *J. Biomed. Opt.* 19(8), 086015 (Aug 20, 2014);

<http://dx.doi.org/10.1117/1.JBO.19.8.086015>

2. Cuiru Sun, Felix Nolte, **Kyle H. Y. Cheng**, Barry Vuong, Kenneth K. C. Lee, Beau A. Standish, Brian Courtney, Thomas R. Marotta, Adrian Mariampillai, and Victor X. D. Yang, "In vivo feasibility of endovascular Doppler optical coherence tomography," *Biomed. Opt. Express* 3, 2600-2610 (2012).

<http://www.opticsinfobase.org/boe/abstract.cfm?URI=boe-3-10-2600>

3. **Kyle H. Y. Cheng**, Edmund Y. Lam, Beau A. Standish, and Victor X. D. Yang, "Speckle reduction of endovascular optical coherence tomography using a generalized divergence measure," Opt. Lett. 37, 2871-2873 (2012).

<http://www.opticsinfobase.org/ol/abstract.cfm?URI=ol-37-14-2871>

4. **Kyle H. Y. Cheng**, Cuiru Sun, Juan P. Cruz, Thomas R. Marotta, Julian Spears, Walter J. Montanera, Aman Thind, Brian Courtney, Beau A. Standish and Victor X. D. Yang, "Comprehensive data visualization for high resolution endovascular carotid arterial wall imaging", J. Biomed. Opt. 17, 056003 (May 04, 2012);

<http://dx.doi.org/10.1117/1.JBO.17.5.056003>

5. **Kyle H. Y. Cheng**, Cuiru Sun, Barry Vuong, Kenneth K. C. Lee, Adrian Mariampillai, Thomas R. Marotta, Julian Spears, Walter J. Montanera, Peter. R. Herman, Tim-Rasmus Kiehl, Beau A. Standish, and Victor X. D. Yang, "Endovascular optical coherence tomography intensity kurtosis: visualization of vasa vasorum in porcine carotid artery," Biomed. Opt. Express 3, 388-399 (2012).

<http://www.opticsinfobase.org/boe/abstract.cfm?URI=boe-3-3-388>

Conference Presentations:

1. **H. Y. Cheng**, J. Grenier, and P. R. Herman, "Femtosecond Laser-Written Couplers in Fused Silica Fiber: Towards Fiber Cladding Optical Circuits," in CLEO: 2013, OSA Technical Digest (online) (Optical Society of America, 2013), paper CM1H.3.

2. **Kyle H. Y. Cheng**, Cuiru Sun, Juan P. Cruz, Thomas R. Marotta, Julian Spears, Walter J. Montanera, Peter R. Herman, Aman Thind, Brian Courtney, Beau A. Standish and Victor X. D. Yang, "Feasibility of endovascular optical coherence tomography for high-resolution carotid vessel wall imaging", Proc. SPIE 8207, 82074N (2012);

doi:10.1117/12.910455

6.3 Future work

In EV-OCT, carotid imaging has been proven safe for neurosurgeons' use. But to further enhance neurosurgeons' ability to evaluate patients' cerebrovascular conditions and risk and cause of stroke, the EV-OCT work has to be extended to the cerebral artery. Safety and feasibility of EV-OCT in the cerebral artery must be evaluated. In addition, the ability of EV-OCT to image and characterize cerebral aneurysm must also be clearly evaluated. One way to extend the use of EV-OCT to the cerebral artery is to re-design a thinner and longer imaging catheter, in order to reach the target lesion site efficiently with minimal damage. Fig. 6.1 shows a Zemax simulation of such a catheter. Notice that the dimension is that of single mode fiber (SMF), which is much smaller than that of the state-of-the-art EV-OCT imaging catheters. The mirror can be made as a total internal reflection mirror consisting of a glass-air interface, the air side of which can be made by selective femtosecond laser assisted chemical etching methods. Although the focal length may not be long enough, it may be solved by adding miniaturized diffractive optical elements or by modifying the mirror to generate special beams with longer Rayleigh range (e.g. Airy beams or Bessel beams).

Moreover, many research studies have also started to miniaturize the OCT system itself [120–122]. Future work should be devoted to handheld OCT devices that can be easily transportable between medical facilities. One possible way to realize this is to use femtosecond laser waveguide writing techniques [123], which can dramatically downsize the necessary optical circuit elements in the OCT system.

As mentioned in Ch. 4, more systemic studies should be carried out for studying the dynamics of vasa vasorum when more resources are available. Other than being an

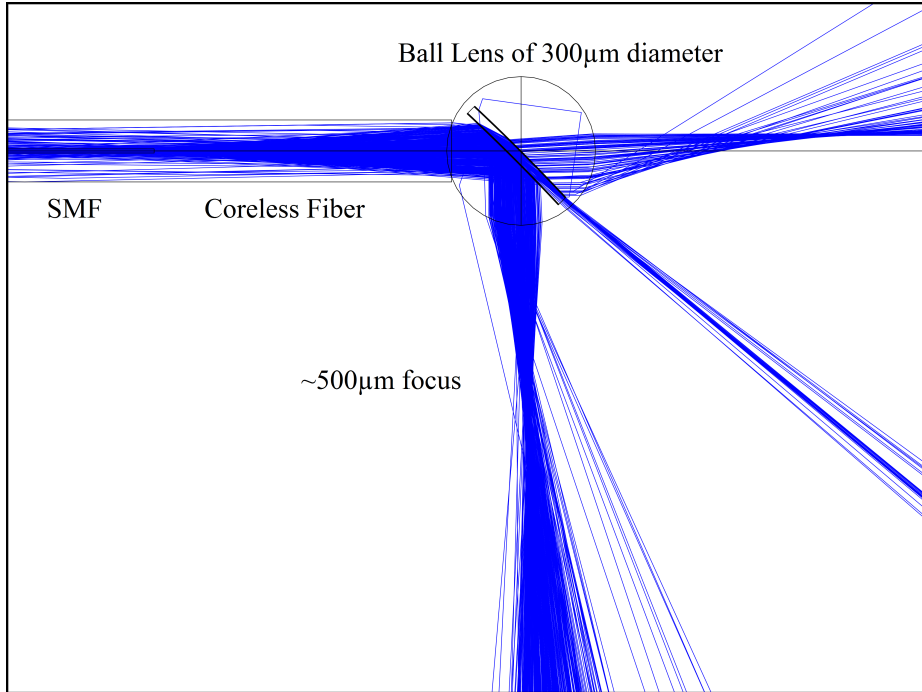


Figure 6.1: Zemax simulation of proposed catheter imaging probe design.

indicator or contributor to atherosclerosis, vasa vasorum may also serve as the conduit to deliver therapeutic drugs into atherosclerotic plaques. Studies have shown that these microvessels actually do connect to the main vessel lumen [83]. By studying whether flow is present in the neovascularization of the atherosclerotic plaque and the normal vasa vasorum, more optimal treatment strategies might be constructed to dissolve these lesions more efficiently, for example, understanding vasa vasorum may enable better design of or tailor specific drug eluting stents.

A more detailed HHT patient study should be carried out to validate any therapeutic interventions. The results from skin imaging is important because they can likely be directly translated to other parts of the body also affected by HHT arteriovenous malformations, such as the lungs and the brain. In addition the method can well be applied to other diseases and conditions such as skin cancers, port wine stains and burn scar recovery. Another direction would be to quantify flow using speckle information. Up till now, a lot of effort has been placed on OCT speckle based microvessel mapping, however,

speckle based quantitative flow estimation *in vivo* remains an elusive challenge. With the advent of swept source laser technologies and ever increasing speed of data acquisition electronics [1, 124], computers are more capable of processing OCT imaging data in unprecedented time frames, thus mandating the need for more advanced algorithms to fully utilize the potential of OCT systems. Our proposed method presents a unique opportunity to map out relative flow rates with enhanced depth *in vivo*. A more sophisticated algorithm and calculations should be able to be devised to analyze the normalized histogram characteristic functions, whilst within a reasonable time.

Appendix A

Data Processing Codes

The following codes are used in Ch. 4 for EV-OCT data manipulation:

Intensity Kurtosis for Detection of Vasa Vasorum (MATLAB):

```
%% LightLab SV-OCT/Kurtosis Measurement Code by Kyle
InFringe_Array = 'Pig7_Unstented_Branch_2.oct';
In_dia = 0;
Out_dia = 1500;
axial_points = 968;
Aline_number = 504;
start_frame = 1;
end_frame = 120;
down = 1;
svk_f = 6;
s_file = 'Pig7_Unstented_Branch_2_S.tif';
output_filename = 'Pig7_Unstented_Branch_2_K_6.tif';

% Odd number for Out_dia

In_radius = In_dia/2; %Inner radius
```

```

spread_factor = 6;

Aline_spreaded = Aline_number + (Aline_number - 1)*spread_factor;
x_polar = zeros(axial_points , Aline_spreaded);
y_polar = zeros(axial_points , Aline_spreaded);
roi_mean1 = zeros(1,end_frame-start_frame);
roi_mean2 = zeros(1,end_frame-start_frame);

%Construct the coordinate system for polar view

for n = 1:round(Out_dia/2)
    for m = 1:Aline_spreaded
        x_polar(n, m) = round((In_radius + n)*cos((2*pi*(m-1))/Aline_spreaded));
        y_polar(n, m) = round((In_radius + n)*sin((2*pi*(m-1))/Aline_spreaded));
    end;
end;
x_polar = x_polar + abs(min(min(x_polar))) - In_dia + 1; % Eliminate negative indices
y_polar = y_polar + abs(min(min(y_polar))) - In_dia + 1;

image_in = zeros(Out_dia , Out_dia , svk_f);
image_innn = zeros(Out_dia , Out_dia , svk_f);
image_ref = imread(InFringe_Array , 'tif' , start_frame);
image_ref = transpose(image_ref);
image_ref = double(abs(image_ref(1:axial_points , :)));
image_ref = linestopolar(image_ref , Out_dia , x_polar , y_polar ,
    axial_points , spread_factor , Aline_spreaded);
image_ref = image_ref(1:Out_dia , 1:Out_dia);
image_innn(:,:,1) = image_ref;

```

```

image_in (:,:,1) = image_ref;
image_ref = 10*log10(image_ref);
image_ref = image_ref./max(max(image_ref));
imwrite(image_ref(1:(Out_dia - In_dia),1:(Out_dia - In_dia)),s_file ,
'writemode','append');

%Start reading in data
for www = (start_frame+down):down:(start_frame+down*(svk_f-1))
    temp_f = imread(InFringe_Array, 'tif', www);
    temp_f = transpose(temp_f);
    temp_f = double(abs(temp_f(1:axial_points,:)));
    temp_f = linestopolar(temp_f,Out_dia,x_polar,y_polar,
        axial_points,spread_factor,Aline_spreaded);
    temp_f = temp_f(1:Out_dia,1:Out_dia);
    image_ref = image_in (:,:, (www/down)-(start_frame/down));
    image_cur = temp_f;
    C = normxcorr2(image_ref,image_cur);
    sizex = Out_dia;
    sizey = Out_dia;
    [C1 I1] = max(C);
    [C2 I2] = max(C1);
    xform = [1 0 0; 0 1 0; sizex-I2 sizey-I1(I2) 1];
    tform = maketform('affine',xform);
    image_cur = imtransform(image_cur, tform,'XData',[1 Out_dia],'
        YData',[1 Out_dia]);
    image_in (:,:, (www/down)-(start_frame/down)+1) = image_cur;
    image_cur1 = 10*log10(image_cur);
    image_cur1 = image_cur1./max(max(image_cur1));
    imwrite(image_cur1(1:(Out_dia - In_dia),1:(Out_dia - In_dia)),
s_file , 'writemode','append');
end

```

```

clear image_cur1

image_innn (:,:, (www/down) - (start_frame/down) + 1) = image_cur;

end;

for nn = (start_frame+down*svk_f):down:end_frame

    temp_f = imread(InFringe_Array, 'tif', nn);

    temp_f = transpose(temp_f);

    temp_f = double(abs(temp_f(1:axial_points,:)));

    temp_f = linesstopolar(temp_f, Out_dia, x_polar, y_polar,
                           axial_points, spread_factor, Aline_spreaded);

    temp_f = temp_f(1:Out_dia, 1:Out_dia);

    image_ref = image_in (:,:, svk_f - 1);

    image_cur = temp_f;

    C = normxcorr2(image_ref, image_cur);

    sizex = Out_dia;

    sizey = Out_dia;

    [C1 I1] = max(C);

    [C2 I2] = max(C1);

    xform = [1 0 0; 0 1 0; sizex-I2 sizey-I1(I2) 1];

    tform = maketform('affine', xform);

    image_cur = imtransform(image_cur, tform, 'XData', [1 Out_dia], ,
                           'YData', [1 Out_dia]);

    image_in (:,:, svk_f) = image_cur;

    image_cur1 = 10*log10(image_cur);

    image_cur1 = image_cur1./max(max(image_cur1));

    imwrite(image_cur1(1:(Out_dia - In_dia), 1:(Out_dia - In_dia)),
            s_file, 'writemode', 'append');

clear image_cur1

```

```
image_innn (:,:,svk_f) = image_cur;

%Speckle Variance / Kurtosis
KKK = kurtosis(image_innn,0,3) - 3;
KKK = KKK./max(max(KKK));

imwrite(KKK(1:(Out_dia - In_dia),1:(Out_dia - In_dia)),
        output_filename, 'writemode', 'append');

image_in (:,:,1:(svk_f-1)) = image_in (:,:,2:svk_f);
image_innn (:,:,1:(svk_f-1)) = image_innn (:,:,2:svk_f);

end;
```

Conversion from Polar Coordinates to Cartesian Coordinates (MATLAB):

```

function [ polar_final ] = linestopolar (image_in , Out_dia , x_polar ,
y_polar , axial_points , spread_factor , Aline_spreaded )

Out_radius = Out_dia /2;
%Spreading the image in its linear form
spreading = 1:( spread_factor + 1):Aline_spreaded ;
Temp_spread = zeros (size (image_in ,1) , Aline_spreaded ) *NaN;
Temp_spread (:, spreading) = image_in ;
interpolate_alines = find (isnan (Temp_spread (1,:))) ;
Temp_spread (:, interpolate_alines) = transpose (interp1 (spreading ,
double (image_in ') , interpolate_alines , 'linear ') );
% figure (2) , imagesc (Temp_spread);
%Assigning pixels to the polar view
polar_img = zeros (max (max (y_polar )) , max (max (x_polar ))) *NaN;
for aaa = 1:axial_points
    for bbb = 1:Aline_spreaded
        polar_img (y_polar (aaa ,bbb) , x_polar (aaa ,bbb)) = Temp_spread (
aaa , bbb) ;
    end ;
end ;
%Interpolate the image in polar view
polar_size_row = size (polar_img ,1) ;
polar_size_column = size (polar_img ,2) ;
polar_final = zeros (max (max (y_polar )) , max (max (x_polar )) );
% polar_final = polar_img;
for ccc = 1:polar_size_row
    original_points = [] ;
    original_points = find (~isnan (polar_img (ccc ,:))) ;

```

```

polar_final(ccc,original_points) = polar_img(ccc,original_points
);
interpolate_points = [];
for ddd = 1:polar_size_column
    polar_value = sqrt((round(polar_size_row/2) - ddd)^2 + (
        round(polar_size_column/2) - ccc)^2);
    if polar_value <= Out_radius && polar_value >= 0 && isnan(
        polar_img(ccc,ddd))
        interpolate_points = [interpolate_points ddd];
    elseif polar_value >= Out_radius || polar_value <= 0
        polar_final(ccc,ddd) = 0;
    end;
end;
if size(original_points) ~= 0
    polar_final(ccc,interpolate_points) = interp1(
        original_points, polar_img(ccc,original_points),
        interpolate_points, 'linear');
end;
end;
polar_final(isnan(polar_final)==1) = 0;
polar_final(isinf(polar_final)==1) = 0;

```

Speckle Reduction of EV-OCT (MATLAB):

```

clear all
clc

[OCTData] = imread( 'Beta_Test.tif' , 'tif' ,1);
OCTData = double((OCTData));
tic

I = OCTData./max(max(OCTData));
size1 = size(I,1);
size2 = size(I,2);
lam2 = 0.75;
beta = 4; %beta ~ = 1 or 0
Ab = 0.03*fspecial( 'gaussian' ,[3 3],1);
xIisedgeu = I;
U = imfilter( medfilt2(I,[7 7]) ,(1/9).*[1 1 1; 1 1 1; 1 1 1] , 'conv' , 'circular' );
U = U./max(max(U));
yp1 = 0.75;
for iterationno3 = 1:40
    xIfil = imfilter( imfilter(xIisedgeu,Ab, 'conv' , 'circular') ,Ab' , 'conv' , 'circular' )-imfilter(I,Ab' , 'conv' , 'circular' );
    xIisedgeu = xIisedgeu - yp1.* (2.*xIfil+lam2.* (2.*beta.*xIisedgeu .^(2.*beta-1)-2.*beta.*xIisedgeu.*U.^ (2.*(beta-1)))./ ( beta.*(beta-1)));
    xIisedgeu = xIisedgeu./max(max(xIisedgeu));
end;
toc

figure(3) , imshow( abs(xIisedgeu));
figure(4) , imshow( I);

```

The following codes are used in Ch. 5 for skin HHT data manipulation:

Depth Enhanced Microangiography (Python):

```
#Speckle Statistics

import numpy
import matplotlib.pyplot as plt
import matplotlib.image as mpimg
from scipy import misc
from scipy import ndimage

start_frame = 2;
end_frame = 5000;
Num_f = 15;

zcPerLine = 882;
numLines = 256;
image_depth = 512;
image_width = numLines*2;
p_depth = 400;

Window = numpy.dot(numpy.atleast_2d(numpy.hanning(image_depth)).T,
                   numpy.atleast_2d(numpy.ones((1,image_width))));

divider = 512;
topHalf = range(0,divider);
bottomHalf = range(divider,zcPerLine);
filename = 'C:/Users/Kyle/Documents/Python_Workspace/
           file_882_256_5000_17HHT5Lesion3.bin';

Array_hist = numpy.zeros((p_depth,image_width,Num_f),numpy.double);
```

```

PMapping = numpy.zeros((p_depth,image_width),numpy.double);

f = open(filename,'rb');

f.seek(zcPerLine*numLines*(start_frame - 1) + zcPerLine*numLines);

for current_frame in xrange(0,Num_f):

    A = numpy.fromfile(f,numpy.int16,count=(zcPerLine*numLines));

    B = numpy.double(numpy.reshape(A,(zcPerLine, numLines),'F'));

    C = numpy.zeros((image_depth,image_width));

    C[0:len(topHalf),0:numLines*2:2] = B[topHalf,0:numLines];

    C[0:len(bottomHalf),1:numLines*2+1:2] = B[bottomHalf,0:numLines

    ];

    C = C*Window;

    complex_temp = numpy.fft.ifft(C,1024,0);

    D = numpy.absolute(complex_temp[0:p_depth,:,:]);

    OCTnnoise = D[370:400,260:290];

    OCTn = D - 1*numpy.sqrt(numpy.mean(numpy.reshape(OCTnnoise

        ,(1,1*30*30))**2));

    OCTn[OCTn < 0] = 0;

    D = 20*numpy.log10(D);

    D = D/numpy.nanmax(D);

    D[D < 0] = 0;

    Array_hist[:, :, current_frame] = OCTn;

    OCT_image2 = D;

    misc.imsave('C:/Users/Kyle/Documents/Python_Output/TestTestS' +

        str(current_frame) + '.jpg',OCT_image2);

for depth_1 in xrange(0,p_depth):

    for width_1 in xrange(0,image_width):

```

```

Array_H, bin_edges = numpy.histogram( Array_hist [ depth_1 ,
    width_1 ,:] , bins=Num_f, range=None , normed=False , weights
    =None , density=None) ;

Array_H = (numpy.imag(numpy.fft.ifft( Array_H ,n=1024))) ;
Array_H1 = Array_H [ 0: len( Array_H ) / 2 ] ;
Array_H1 [ 150:1024 ] = 0 ;
PMapping [ depth_1 ,width_1 ] = numpy.sum( Array_H1 ) ;

PMapping = ndimage.filters.uniform_filter( PMapping ,6 ) ;
PMapping = PMapping - numpy.median( numpy.reshape( PMapping
    [ 0:150 ,:] ,( 1 ,1*150 * image_width ))) ;
PMapping [ PMapping < 0 ] = 0 ;

# for width_1 = 1:image_width
# RRR = xcorr( PMapping (:, width_1 )) ;
# RRR = RRR > 0.2*max(RRR) ;
# RRRind = find( RRR) ;
# for depth_1 = 2:p_depth
# if isempty( RRR) == 0 && length( RRRind ) > (depth_1-1)
# PMapping( depth_1 ,width_1 ) = PMapping( depth_1 ,width_1 )*
# exp(-(1/10)*sum( PMapping ( 1:( depth_1-1 ), width_1 ))) ;
# elseif isempty( RRR) == 0 && length( RRRind ) <= (depth_1-1)
# PMapping( depth_1 ,width_1 ) = PMapping( depth_1 ,width_1 )*
# exp(-(1/10)*sum( PMapping ( depth_1-length( RRRind ):( depth_1-1 ),
    width_1 ))) ;

misc.imsave( 'C:/Users/Kyle/Documents/Python_Output/TestTestP' + str(
    current_frame) + '.jpg' ,PMapping) ;

Array_hist [:,:,0:Num_f-1] = Array_hist [:,:,1:Num_f] ;

```

```

for after in xrange((Num_f),(end_frame-start_frame+1)):

    A = numpy.fromfile(f,numpy.int16,count=(zcPerLine*numLines));
    B = numpy.double(numpy.reshape(A,(zcPerLine,numLines),'F'));
    C = numpy.zeros((image_depth,image_width));
    C[0:len(topHalf),0:numLines*2:2] = B[topHalf,0:numLines];
    C[0:len(bottomHalf),1:numLines*2+1:2] = B[bottomHalf,0:numLines
    ];
    C = C*Window;
    complex_temp = numpy.fft.ifft(C,1024,0);
    D = numpy.absolute(complex_temp[0:p_depth,:]);
    OCTnnoise = D[370:400,260:290];
    OCTn = D - 1*numpy.sqrt(numpy.mean(numpy.reshape(OCTnnoise
    ,(1,1*30*30))**2));
    OCTn[OCTn < 0] = 0;
    D = 20*numpy.log10(D);
    D = D/numpy.nanmax(D);
    D[D < 0] = 0;
    Array_hist[:, :, Num_f-1] = OCTn;
    OCT_image2 = D;
    misc.imsave('C:/Users/Kyle/Documents/Python_Output/TestTestS' +
    str(after) + '.jpg',OCT_image2);

for depth_1 in xrange(0,p_depth):

    for width_1 in xrange(0,image_width):

        Array_H, bin_edges = numpy.histogram(Array_hist[depth_1,
        width_1,:], bins=Num_f, range=None, normed=False,
        weights=None, density=None);

        Array_H = (numpy.imag(numpy.fft.ifft(Array_H,n=1024)));
        Array_H1 = Array_H[0:len(Array_H)/2];

```

```

        Array_H1[150:1024] = 0;
        PMapping [ depth_1 , width_1 ] = numpy.sum( Array_H1 ) ;

PMapping = ndimage.filters.uniform_filter (PMapping,6) ;
PMapping = PMapping - numpy.median (numpy.reshape (PMapping
[0:150 ,:],(1,1*150*image_width))) ;
PMapping [PMapping < 0] = 0;

#      for width_1 = 1:image_width
#          RRR = xcorr (PMapping (:,width_1));
#          RRR = RRR > 0.2*max(RRR);
#          RRRind = find (RRR);
#          for depth_1 = 2:p_depth
#              if isempty (RRR) == 0 && length (RRRind) > (depth_1-1)
#                  PMapping (depth_1 , width_1 ) = PMapping (depth_1 ,
#                      width_1 )*exp(-(1/10)*sum (PMapping (1:(depth_1-1),width_1)));
#              elseif isempty (RRR) == 0 && length (RRRind) <= (depth_1
#                  -1)
#                  PMapping (depth_1 , width_1 ) = PMapping (depth_1 ,
#                      width_1 )*exp(-(1/10)*sum (PMapping (depth_1-length (RRRind):(depth_1
#                  -1),width_1)));
#          misc.imsave( 'C:/Users/Kyle/Documents/Python_Output/TestTestP' +
#              str ( after ) + '.jpg' ,PMapping) ;
        Array_hist [:,:,0:Num_f-1] = Array_hist [:,:,1:Num_f] ;

image1_plot = plt.imshow(PMapping) ;

```

Bibliography

- [1] Wolfgang Wieser, Wolfgang Draxinger, Thomas Klein, Sebastian Karpf, Tom Pfeiffer, and Robert Huber. High definition live 3d-oct in vivo: design and evaluation of a 4d oct engine with 1 gvoxel/s. *Biomed. Opt. Express*, 5(9):2963–2977, Sep 2014.
- [2] D Huang, EA Swanson, CP Lin, JS Schuman, WG Stinson, W Chang, MR Hee, T Flotte, K Gregory, CA Puliafito, and al. et. Optical coherence tomography. *Science*, 254(5035):1178–1181, 1991.
- [3] Ehsan Azimi, Bin Liu, and Mark E. Brezinski. Real-time and high-performance calibration method for high-speed swept-source optical coherence tomography. *Journal of Biomedical Optics*, 15(1):016005–016005–8, 2010.
- [4] Delphine Sacchet, Michal Brzezinski, Julien Moreau, Patrick Georges, and Arnaud Dubois. Motion artifact suppression in full-field optical coherence tomography. *Appl. Opt.*, 49(9):1480–1488, Mar 2010.
- [5] Kenneth K. C. Lee, Adrian Mariampillai, Joe X. Z. Yu, David W. Cadotte, Brian C. Wilson, Beau A. Standish, and Victor X. D. Yang. Real-time speckle variance swept-source optical coherence tomography using a graphics processing unit. *Biomed. Opt. Express*, 3(7):1557–1564, Jul 2012.
- [6] Beau A. Standish, Xiao Jin, Jurek Smolen, Adrian Mariampillai, Nigel R. Munce, Brian C. Wilson, I. Alex Vitkin, and Victor X. D. Yang. Interstitial doppler optical coherence tomography monitors microvascular changes during photodynamic

- therapy in a dunning prostate model under varying treatment conditions. *Journal of Biomedical Optics*, 12(3):034022–034022–7, 2007.
- [7] Brendan F. Kennedy, Xing Liang, Steven G. Adie, Derek K. Gerstmann, Bryden C. Quirk, Stephen A. Boppart, and David D. Sampson. In vivo three-dimensional optical coherence elastography. *Opt. Express*, 19(7):6623–6634, Mar 2011.
- [8] David Stifter, Elisabeth Leiss-Holzinger, Zoltan Major, Bernhard Baumann, Michael Pircher, Erich Götzinger, Christoph K. Hitzenberger, and Bettina Heise. Dynamic optical studies in materials testing with spectral-domain polarization-sensitive optical coherence tomography. *Opt. Express*, 18(25):25712–25725, Dec 2010.
- [9] Samuel Lawman and Haida Liang. High precision dynamic multi-interface profilometry with optical coherence tomography. *Appl. Opt.*, 50(32):6039–6048, Nov 2011.
- [10] Gijs van Soest, Frits Mastik, Nico de Jong, and Anton F W van der Steen. Robust intravascular optical coherence elastography by line correlations. *Physics in Medicine and Biology*, 52(9):2445, 2007.
- [11] Desmond C. Adler, Shu-Wei Huang, Robert Huber, and James G. Fujimoto. Photothermal detection of gold nanoparticles using phase-sensitive optical coherence tomography. *Opt. Express*, 16(7):4376–4393, Mar 2008.
- [12] Victor X. D. Yang, Maggie Gordon, Shou jiang Tang, Norman Marcon, Geoffrey Gardiner, Bing Qi, Stuart Bisland, Emily Seng-Yue, Stewart Lo, Julius Pekar, Brian Wilson, and I. Vitkin. High speed, wide velocity dynamic range doppler optical coherence tomography (part iii): in vivo endoscopic imaging of blood flow in the rat and human gastrointestinal tracts. *Opt. Express*, 11(19):2416–2424, Sep 2003.

- [13] Jiefeng Xi, Anqi Zhang, Zhenyu Liu, Wenxuan Liang, Lih Y. Lin, Shaoyong Yu, and Xingde Li. Diffractive catheter for ultrahigh-resolution spectral-domain volumetric oct imaging. *Opt. Lett.*, 39(7):2016–2019, Apr 2014.
- [14] Nicusor Iftimia, R. Daniel Ferguson, Mircea Mujat, Ankit H. Patel, Ellen Ziyi Zhang, William Fox, and Milind Rajadhyaksha. Combined reflectance confocal microscopy/optical coherence tomography imaging for skin burn assessment. *Biomed. Opt. Express*, 4(5):680–695, May 2013.
- [15] Melissa J. Suter, Seemantini K. Nadkarni, Giora Weisz, Atsushi Tanaka, Farouc A. Jaffer, Brett E. Bouma, and Guillermo J. Tearney. Intravascular optical imaging technology for investigating the coronary artery. *Journal of the American College of Cardiology: Cardiovascular Imaging*, 4(9):1022–1039, 2011.
- [16] Patrick Z. McVeigh, Raphael Sacho, Robert A. Weersink, Vitor M. Pereira, Walter Kucharczyk, Eric J. Seibel, Brian C. Wilson, and Timo Krings. High-resolution angioscopic imaging during endovascular neurosurgery. *Neurosurgery*, 75(2):171–180, 2014.
- [17] H. Zacharatos, A.E. Hassan, and A.I. Qureshi. Intravascular ultrasound: Principles and cerebrovascular applications. *American Journal of Neuroradiology*, 31(4):586–597, 2010.
- [18] Akiko Maehara, Gary S. Mintz, and Neil J. Weissman. Advances in intravascular imaging. *Circulation: Cardiovascular Interventions*, 2(5):482–490, 2009.
- [19] David A. Boas and Andrew K. Dunn. Laser speckle contrast imaging in biomedical optics. *Journal of Biomedical Optics*, 15(1):011109–011109–12, 2010.
- [20] Lisa M. Richards, S. M. Shams Kazmi, Janel L. Davis, Katherine E. Olin, and Andrew K. Dunn. Low-cost laser speckle contrast imaging of blood flow using a webcam. *Biomed. Opt. Express*, 4(10):2269–2283, Oct 2013.

- [21] Phill B. Jones, Hwa Kyoung Shin, David A. Boas, Bradley T. Hyman, Michael A. Moskowitz, Cenk Ayata, and Andrew K. Dunn. Simultaneous multispectral reflectance imaging and laser speckle flowmetry of cerebral blood flow and oxygen metabolism in focal cerebral ischemia. *Journal of Biomedical Optics*, 13(4):044007–044007–11, 2008.
- [22] Victor X.D Yang, Maggie L Gordon, Alvin Mok, Yonghua Zhao, Zhongping Chen, Richard S.C Cobbold, Brian C Wilson, and I Alex Vitkin. Improved phase-resolved optical doppler tomography using the kasai velocity estimator and histogram segmentation. *Optics Communications*, 208(46):209 – 214, 2002.
- [23] Victor Yang, Maggie Gordon, Bing Qi, Julius Pekar, Stuart Lo, Emily Seng-Yue, Alvin Mok, Brian Wilson, and I. Vitkin. High speed, wide velocity dynamic range doppler optical coherence tomography (part i): System design, signal processing, and performance. *Opt. Express*, 11(7):794–809, Apr 2003.
- [24] Adrian Mariampillai, Beau A. Standish, Eduardo H. Moriyama, Mamta Khurana, Nigel R. Munce, Michael K. K. Leung, James Jiang, Alex Cable, Brian C. Wilson, I. Alex Vitkin, and Victor X. D. Yang. Speckle variance detection of microvasculature using swept-source optical coherence tomography. *Opt. Lett.*, 33(13):1530–1532, Jul 2008.
- [25] Adrian Mariampillai, Michael K. K. Leung, Mark Jarvi, Beau A. Standish, Kenneth Lee, Brian C. Wilson, Alex Vitkin, and Victor X. D. Yang. Optimized speckle variance oct imaging of microvasculature. *Opt. Lett.*, 35(8):1257–1259, Apr 2010.
- [26] Benjamin J. Vakoc, Dai Fukumura, Rakesh K. Jain, and Brett E. Bouma. Cancer imaging by optical coherence tomography: preclinical progress and clinical potential. *Nat Rev Cancer*, 12(5):363–368, 2012.

- [27] Benjamin J Vakoc, Ryan M Lanning, James A Tyrrell, Timothy P Padera, Lisa A Bartlett, Triantafyllos Stylianopoulos, Lance L Munn, Guillermo J Tearney, Dai Fukumura, Rakesh K Jain, and Brett E Bouma. Three-dimensional microscopy of the tumor microenvironment *in vivo* using optical frequency domain imaging. *Nat Med*, 15(10):1219–1223, 2009.
- [28] Yali Jia, Ou Tan, Jason Tokayer, Benjamin Potsaid, Yimin Wang, Jonathan J. Liu, Martin F. Kraus, Hrebesh Subhash, James G. Fujimoto, Joachim Horngger, and David Huang. Split-spectrum amplitude-decorrelation angiography with optical coherence tomography. *Opt. Express*, 20(4):4710–4725, Feb 2012.
- [29] Pearse A. Keane, Praveen J. Patel, Sandra Liakopoulos, Florian M. Heussen, Srinivas R. Sadda, and Adnan Tufail. Evaluation of age-related macular degeneration with optical coherence tomography. *Survey of Ophthalmology*, 57(5):389 – 414, 2012.
- [30] Lisandro M Sakata, Julio DeLeon-Ortega, Viviane Sakata, and Christopher A Girkin. Optical coherence tomography of the retina and optic nerve a review. *Clinical & Experimental Ophthalmology*, 37(1):90–99, 2009.
- [31] JohnC. BuAbbud, MotasemM. Al-latayfeh, and JenniferK. Sun. Optical coherence tomography imaging for diabetic retinopathy and macular edema. *Current Diabetes Reports*, 10(4):264–269, 2010.
- [32] C. L. Shields, S. Kaliki, D. Rojanaporn, S. R. Ferenczy, and J. A. Shields. Enhanced depth imaging optical coherence tomography of small choroidal melanoma: Comparison with choroidal nevus. *Archives of Ophthalmology*, 130(7):850–856, 2012.
- [33] WooJhon Choi, Kathrin J. Mohler, Benjamin Potsaid, Chen D. Lu, Jonathan J. Liu, Vijaysekhar Jayaraman, Alex E. Cable, Jay S. Duker, Robert Huber, and

- James G. Fujimoto. Choriocapillaris and choroidal microvasculature imaging with ultrahigh speed oct angiography. *PLoS ONE*, 8(12):e81499, 12 2013.
- [34] Giovanni Staurenghi, Srinivas Sadda, Usha Chakravarthy, and Richard F. Spaide. Proposed lexicon for anatomic landmarks in normal posterior segment spectral-domain optical coherence tomography. *Ophthalmology*, 121(8):1572–1578, 2014.
- [35] Elke Sattler, Raphaela Kstle, and Julia Welzel. Optical coherence tomography in dermatology. *Journal of Biomedical Optics*, 18(6):061224–061224, 2013.
- [36] J. M. Tucker-Schwartz, T. A. Meyer, C. A. Patil, C. L. Duvall, and M. C. Skala. In vivo photothermal optical coherence tomography of gold nanorod contrast agents. *Biomed. Opt. Express*, 3(11):2881–2895, Nov 2012.
- [37] S. Brand, J. M. Poneros, B. E. Bouma, G. J. Tearney, C. C. Compton, and N.S. Nishioka. Optical coherence tomography in the gastrointestinal tract. *Endoscopy*, 32(10):796–803, 2000.
- [38] Y. Chen, A. D. Aguirre1, P. L. Hsiung, S. Desai, P. R. Herz, M. Pedrosa, Q. Huang, M. Figueiredo, S. W. Huang, A. Koski, J. M. Schmitt, J. G. Fujimoto, and H. Mashimo. Ultrahigh resolution optical coherence tomography of barretts esophagus: preliminary descriptive clinical study correlating images with histology. *Endoscopy*, 39(7):599–605, 2007.
- [39] Paul Herz, Yu Chen, Aaron Aguirre, James Fujimoto, Hiroshi Mashimo, Joseph Schmitt, Amanda Koski, John Goodnow, and Chris Petersen. Ultrahigh resolution optical biopsy with endoscopic optical coherence tomography. *Opt. Express*, 12(15):3532–3542, Jul 2004.
- [40] A. Curatolo, R. A. McLaughlin, B. C. Quirk, R. W. Kirk, A. G. Bourke, B. A. Wood, P. D. Robbins, C. M. Saunders, and D. D. Sampson. Ultrasound-guided

- optical coherence tomography needle probe for the assessment of breast cancer tumor margins. *American Journal of Roentgenology*, 199(4):W520–W522, 2012.
- [41] Wei-Cheng Kuo, Jongsik Kim, Nathan D. Shemonski, Eric J. Chaney, Darold R. Spillman, and Stephen A. Boppart. Real-time three-dimensional optical coherence tomography image-guided core-needle biopsy system. *Biomed. Opt. Express*, 3(6):1149–1161, Jun 2012.
- [42] Angel Salinas-Alamn, Alfredo Garca-Layana, Miguel J. Maldonado, Carmen Sainz-Gmez, and Aurora Alvrez-Vidal. Using optical coherence tomography to monitor photodynamic therapy in age related macular degeneration. *American Journal of Ophthalmology*, 140(1):23.e1–23.e7, 2005.
- [43] J. Thomsen, N. Bendse, K. Svanberg, S. Andersson-Engels, T. M. Jrgensen, L. Thrane, H. E. Larsen, F. Pedersen, and P. E. Andersen. Optical doppler tomography for monitoring vascularization during photodynamic therapy of skin cancer lesions. *Proc. SPIE*, 6991:699118–699118–7, 2008.
- [44] Beau A. Standish, Victor X.D. Yang, Nigel R. Munce, Louis-Michel Wong Kee Song, Geoffrey Gardiner, Annie Lin, Youxin I. Mao, Alex Vitkin, Norman E. Marcon, and Brian C. Wilson. Doppler optical coherence tomography monitoring of microvascular tissue response during photodynamic therapy in an animal model of barrett’s esophagus. *Gastrointestinal Endoscopy*, 66(2):326 – 333, 2007.
- [45] Victor X. D. Yang, Julius Pekar, Stewart S. W. Lo, Maggie L. Gordon, Brian C. Wilson, and I. Alex Vitkin. Optical coherence and doppler tomography for monitoring tissue changes induced by laser thermal therapyan in vivo feasibility study. *Review of Scientific Instruments*, 74(1):437–440, 2003.
- [46] Xingde Li, Scott Martin, Costas Pitriss1, Ravi Ghanta1, Debra L. Stamper, Michelle Harman, James G. Fujimoto, and Mark E. Brezinski. High-resolution optical co-

- herence tomographic imaging of osteoarthritic cartilage during open knee surgery. *Arthritis Research & Therapy*, 7(2):R318–R323, 2005.
- [47] Harsha Radhakrishnan and Vivek J. Srinivasan. Compartment-resolved imaging of cortical functional hyperemia with oct angiography. *Biomed. Opt. Express*, 4(8):1255–1268, Aug 2013.
- [48] Vivek J. Srinivasan and Harsha Radhakrishnan. Optical coherence tomography angiography reveals laminar microvascular hemodynamics in the rat somatosensory cortex during activation. *NeuroImage*, 102, Part 2(0):393 – 406, 2014.
- [49] Vivek J. Srinivasan, Sava Sakadžić, Iwona Gorczynska, Svetlana Ruvinskaya, Weicheng Wu, James G. Fujimoto, and David A. Boas. Depth-resolved microscopy of cortical hemodynamics with optical coherence tomography. *Opt. Lett.*, 34(20):3086–3088, Oct 2009.
- [50] B.A. Standish, J. Spears, T.R. Marotta, W. Montanera, and V.X.D. Yang. Vascular wall imaging of vulnerable atherosclerotic carotid plaques: Current state of the art and potential future of endovascular optical coherence tomography. *American Journal of Neuroradiology*, 33(9):1642–1650, 2012.
- [51] H C Stary, D H Blankenhorn, A B Chandler, S Glagov, W Insull, M Richardson, M E Rosenfeld, S A Schaffer, C J Schwartz, and W D Wagner. A definition of the intima of human arteries and of its atherosclerosis-prone regions. a report from the committee on vascular lesions of the council on arteriosclerosis, american heart association. *Circulation*, 85(1):391–405, 1992.
- [52] Herbert C. Stary, A. Bleakley Chandler, Robert E. Dinsmore, Valentin Fuster, Seymour Glagov, William Insull, Michael E. Rosenfeld, Colin J. Schwartz, William D. Wagner, and Robert W. Wissler. A definition of advanced types of atherosclerotic lesions and a histological classification of atherosclerosis: A report from the

- committee on vascular lesions of the council on arteriosclerosis, american heart association. *Circulation*, 92(5):1355–1374, 1995.
- [53] H C Stary, A B Chandler, S Glagov, J R Guyton, W Insull, M E Rosenfeld, S A Schaffer, C J Schwartz, W D Wagner, and R W Wissler. A definition of initial, fatty streak, and intermediate lesions of atherosclerosis. a report from the committee on vascular lesions of the council on arteriosclerosis, american heart association. *Arteriosclerosis, Thrombosis, and Vascular Biology*, 14(5):840–56, 1994.
- [54] WRITING GROUP MEMBERS, Donald Lloyd-Jones, Robert J. Adams, Todd M. Brown, Mercedes Carnethon, Shifan Dai, Giovanni De Simone, T. Bruce Ferguson, Earl Ford, Karen Furie, Cathleen Gillespie, Alan Go, Kurt Greenlund, Nancy Haase, Susan Hailpern, P. Michael Ho, Virginia Howard, Brett Kissela, Steven Kittner, Daniel Lackland, Lynda Lisabeth, Ariane Marelli, Mary M. McDermott, James Meigs, Dariush Mozaffarian, Michael Mussolino, Graham Nichol, Vronique L. Roger, Wayne Rosamond, Ralph Sacco, Paul Sorlie, Randall Stafford, Thomas Thom, Sylvia Wasserthiel-Smoller, Nathan D. Wong, Judith Wylie-Rosett, on behalf of the American Heart Association Statistics Committee, and Stroke Statistics Subcommittee. Heart disease and stroke statistics2010 update: A report from the american heart association. *Circulation*, 121(7):e46–e215, 2010.
- [55] Scott Kinlay. Changes in stroke epidemiology, prevention, and treatment. *Circulation*, 124(19):e494–e496, 2011.
- [56] Henry J.M. Barnett, D. Wayne Taylor, Michael Eliasziw, Allan J. Fox, Gary G. Ferguson, R. Brian Haynes, Richard N. Rankin, G. Patrick Clagett, Vladimir C. Hachinski, David L. Sackett, Kevin E. Thorpe, Heather E. Meldrum, and J. David Spence. Benefit of carotid endarterectomy in patients with symptomatic moderate or severe stenosis. *New England Journal of Medicine*, 339(20):1415–1425, 1998. PMID: 9811916.

- [57] Beneficial effect of carotid endarterectomy in symptomatic patients with high-grade carotid stenosis. *New England Journal of Medicine*, 325(7):445–453, 1991. PMID: 1852179.
- [58] Thomas G. Brott, Robert W. Hobson, George Howard, Gary S. Roubin, Wayne M. Clark, William Brooks, Ariane Mackey, Michael D. Hill, Pierre P. Leimgruber, Alice J. Sheffet, Virginia J. Howard, Wesley S. Moore, Jenifer H. Voeks, L. Nelson Hopkins, Donald E. Cutlip, David J. Cohen, Jeffrey J. Popma, Robert D. Ferguson, Stanley N. Cohen, Joseph L. Blackshear, Frank L. Silver, J.P. Mohr, Brajesh K. Lal, and James F. Meschia. Stenting versus endarterectomy for treatment of carotid-artery stenosis. *New England Journal of Medicine*, 363(1):11–23, 2010. PMID: 20505173.
- [59] Adrian F. Low, Guillermo J. Tearney, Brett E. Bouma, and Ik-Kyung Jang. Technology insight: optical coherence tomographycurrent status and future development. *Nature Clinical Practice Cardiovascular Medicine*, 3(3):154–162, 2006.
- [60] Marlon S. Mathews, Jianping Su, Esmaeil Heidari, Elad I. Levy, Mark E Linskey, and Zhongping Chen. Neuroendovascular optical coherence tomography imaging and histological analysis. *Neurosurgery*, 69(2):430–439, 2011.
- [61] Shinichi Yoshimura, Masanori Kawasaki, Kiyofumi Yamada, Arihiro Hattori, Kazuhiko Nishigaki, Shinya Minatoguchi, and Toru Iwama. Oct of human carotid arterial plaques. *Journal of the American College of Cardiology: Cardiovascular Imaging*, 4(4):432–436, 2011.
- [62] Bernhard Reimers, Dimitrios N. Nikas, Eugenio Stabile, Luca Favero, Salvatore Sacc, Alberto Cremonesi, and Paolo Rubino. Preliminary experience with optical coherence tomography imaging to evaluate carotid artery stents: safety, feasibility and techniques. *EuroIntervention*, 7(1):98–105, 2011.

- [63] Kyle H. Y. Cheng, Cuiru Sun, Juan P. Cruz, Thomas R. Marotta, Julian Spears, Walter J. Montanera, Aman Thind, Brian Courtney, Beau A. Standish, and Victor X. D. Yang. Comprehensive data visualization for high resolution endovascular carotid arterial wall imaging. *Journal of Biomedical Optics*, 17(5):056003–1–056003–6, 2012.
- [64] Guillermo J. Tearney, Evelyn Regar, Takashi Akasaka, Tom Adriaenssens, Peter Barlis, Hiram G. Bezerra, Brett Bouma, Nico Bruining, Jin man Cho, Saqib Chowdhary, Marco A. Costa, Ranil de Silva, Jouke Dijkstra, Carlo Di Mario, Darius Dudeck, Erlin Falk, Marc D. Feldman, Peter Fitzgerald, Hector Garcia, Nieves Gonzalo, Juan F. Granada, Giulio Guagliumi, Niels R. Holm, Yasuhiro Honda, Fumiaki Ikeno, Masanori Kawasaki, Janusz Kochman, Lukasz Koltowski, Takashi Kubo, Teruyoshi Kume, Hiroyuki Kyono, Cheung Chi Simon Lam, Guy Lamouche, David P. Lee, Martin B. Leon, Akiko Maehara, Olivia Manfrini, Gary S. Mintz, Kiyouchi Mizuno, Marie angle Morel, Seemantini Nadkarni, Hiroyuki Okura, Hiromasa Otake, Arkadiusz Pietrasik, Francesco Prati, Lorenz Rber, Maria D. Radu, Johannes Rieber, Maria Riga, Andrew Rollins, Mireille Rosenberg, Vasile Sirbu, Patrick W.J.C. Serruys, Kenei Shimada, Toshiro Shinke, Junya Shite, Eliot Siegel, Shinjo Sonada, Melissa Suter, Shigeho Takarada, Atsushi Tanaka, Mitsuyasu Terashima, Thim Troels, Shiro Uemura, Giovanni J. Ughi, Heleen M.M. van Beusekom, Antonius F.W. van der Steen, Gerrit-Ann van Es, Gijs van Soest, Renu Virmani, Sergio Waxman, Neil J. Weissman, and Giora Weisz. Consensus standards for acquisition, measurement, and reporting of intravascular optical coherence tomography studies: A report from the international working group for intravascular optical coherence tomography standardization and validation. *Journal of the American College of Cardiology*, 59(12):1058 – 1072, 2012.
- [65] Oliver A. Meissner, Johannes Rieber, Gregor Babaryka, Melanie Oswald, Susanne

- Reim, Uwe Siebert, Thomas Redel, Maximilian Reiser, and Ullrich Mueller-Lisse. Intravascular optical coherence tomography: Comparison with histopathology in atherosclerotic peripheral artery specimens. *Journal of Vascular and Interventional Radiology*, 17:343–349, 2005.
- [66] Smita I. Negi and Oscar Rosales. The role of intravascular optical coherence tomography in peripheral percutaneous interventions. *Journal of invasive cardiology*, 25(3):E51–E53, 2013.
- [67] R. Michael Scott and Edward R. Smith. Moyamoya disease and moyamoya syndrome. *New England Journal of Medicine*, 360(12):1226–1237, 2009. PMID: 19297575.
- [68] Per C. Hansen, James G. Nagy, and Dianne P. O’ Leary. *Deblurring Images: Matrices, Spectra, and Filtering*. Society for Industrial and Applied Mathematics, 2006.
- [69] Minami Mihoko and Shinto Eguchi. Robust blind source separation by beta divergence. *Neural Computation*, 14(8):1859–1886, 2002.
- [70] R. Hennequin, B. David, and R. Badeau. Beta-divergence as a subclass of bregman divergence. *Signal Processing Letters, IEEE*, 18(2):83–86, Feb 2011.
- [71] G. Le Besnerais, J.-F. Bercher, and G. Demoment. A new look at entropy for solving linear inverse problems. *Information Theory, IEEE Transactions on*, 45(5):1565–1578, Jul 1999.
- [72] Joesph W. Goodman. *Speckle Phenomena in Optics*. Roberts & Company Publishers, 2007.
- [73] HKon Gudbjartsson and Samuel Patz. The rician distribution of noisy mri data. *Magnetic Resonance in Medicine*, 34(6):910–914, 1995.

- [74] E. Regar, H.M.M. van Beusekom, W.J. van der Giessen, and P.W. Serruys. Optical coherence tomography findings at 5-year follow-up after coronary stent implantation. *Circulation*, 112(23):e345–e346, 2005.
- [75] Marc Vorpahl, Masataka Nakano, and Renu Virmani. Small black holes in optical frequency domain imaging matches intravascular neoangiogenesis formation in histology. *European Heart Journal*, 31(15):1889, 2010.
- [76] B E Bouma, G J Tearney, H Yabushita, M Shishkov, C R Kauffman, D De-Joseph Gauthier, B D MacNeill, S L Houser, H T Aretz, E F Halpern, and I-K Jang. Evaluation of intracoronary stenting by intravascular optical coherence tomography. *Heart*, 89(3):317–320, 2003.
- [77] Nieves Gonzalo, Patrick W. Serruys, Takayuki Okamura, Heleen M. van Beusekom, Hector M. Garcia-Garcia, Gijs van Soest, Wim van der Giessen, and Evelyn Regar. Optical coherence tomography patterns of stent restenosis. *American Heart Journal*, 158(2):284 – 293, 2009.
- [78] Erik L. Ritman and Amir Lerman. The dynamic vasa vasorum. *Cardiovascular Research*, 75(4):649–658, 2007.
- [79] Monty A. Martin and Tom R. Marotta. Vasa vasorum: Another cause of the carotid string sign. *American Journal of Neuroradiology*, 20(2):259–262, 1999.
- [80] Juan F. Granada and Steven B. Feinstein. Imaging of the vasa vasorum. *Nature Clinical Practice Cardiovascular Medicine*, 5:S18–S25, 2008.
- [81] Song Hu and Lihong V. Wang. Photoacoustic imaging and characterization of the microvasculature. *Journal of Biomedical Optics*, 15(1):011101–011101–15, 2010.
- [82] Jimmy L Su, Bo Wang, Katheryne E Wilson, Carolyn L Bayer, Yun-Sheng Chen, Seungsoo Kim, Kimberly A Homan, and Stanislav Y Emelianov. Advances in

- clinical and biomedical applications of photoacoustic imaging. *Expert Opinion on Medical Diagnostics*, 4(6):497–510, 2010. PMID: 20718689.
- [83] Mario Gssl, Michael Rosol, Nasser M. Malyar, Lorraine A. Fitzpatrick, Patricia E. Beighley, Mair Zamir, and Erik L. Ritman. Functional anatomy and hemodynamic characteristics of vasa vasorum in the walls of porcine coronary arteries. *The Anatomical Record Part A: Discoveries in Molecular, Cellular, and Evolutionary Biology*, 272A(2):526–537, 2003.
- [84] Kevin P. Baland and H. L. MacGillivray. Kurtosis: A critical review. *The American Statistician*, 42(2):111–119, 1988.
- [85] Jens H. Jensen and Joseph A. Helpern. Mri quantification of non-gaussian water diffusion by kurtosis analysis. *NMR in Biomedicine*, 23(7):698–710, 2010.
- [86] A Briassouli and I Kompatsiaris. Robust temporal activity templates using higher order statistics. *Image Processing, IEEE Transactions on*, 18(12):2756–2768, Dec 2009.
- [87] Michael Pircher, Erich Gotzinger, Rainer Leitgeb, Adolf F. Fercher, and Christoph. K. Hitzenberger. Speckle reduction in optical coherence tomography by frequency compounding. *Journal of Biomedical Optics*, 8(3):565–569, 2003.
- [88] A. E. Desjardins, B. J. Vakoc, W. Y. Oh, S. M. Motaghiannezam, G. J. Tearney, and B. E. Bouma. Angle-resolved optical coherence tomography with sequential angular selectivity for speckle reduction. *Opt. Express*, 15(10):6200–6209, May 2007.
- [89] Desmond C. Adler, Tony H. Ko, and James G. Fujimoto. Speckle reduction in optical coherence tomography images by use of a spatially adaptive wavelet filter. *Opt. Lett.*, 29(24):2878–2880, Dec 2004.

- [90] Prabakar Puvanathasan and Kostadinka Bizheva. Speckle noise reduction algorithm for optical coherence tomography based on interval type ii fuzzy set. *Opt. Express*, 15(24):15747–15758, Nov 2007.
- [91] Zhongping Jian, Zhaoxia Yu, Lingfeng Yu, Bin Rao, Zhongping Chen, and Bruce J. Tromberg. Speckle attenuation in optical coherence tomography by curvelet shrinkage. *Opt. Lett.*, 34(10):1516–1518, May 2009.
- [92] J. Rogowska and M.E. Brezinski. Evaluation of the adaptive speckle suppression filter for coronary optical coherence tomography imaging. *Medical Imaging, IEEE Transactions on*, 19(12):1261–1266, Dec 2000.
- [93] Prabakar Puvanathasan and Kostadinka Bizheva. Interval type-ii fuzzy anisotropic diffusion algorithm for speckle noise reduction in optical coherence tomography images. *Opt. Express*, 17(2):733–746, Jan 2009.
- [94] Daniel L. Marks, Tyler S. Ralston, and Stephen A. Boppart. Speckle reduction by i-divergence regularization in optical coherence tomography. *J. Opt. Soc. Am. A*, 22(11):2366–2371, Nov 2005.
- [95] Manuel Guizar-Sicairos, Samuel T. Thurman, and James R. Fienup. Efficient subpixel image registration algorithms. *Opt. Lett.*, 33(2):156–158, Jan 2008.
- [96] Kyle H. Y. Cheng, Cuiru Sun, Barry Vuong, Kenneth K. C. Lee, Adrian Mariampil-lai, Thomas R. Marotta, Julian Spears, Walter J. Montanera, Peter. R. Herman, Tim-Rasmus Kiehl, Beau A. Standish, and Victor X. D. Yang. Endovascular optical coherence tomography intensity kurtosis: visualization of vasa vasorum in porcine carotid artery. *Biomed. Opt. Express*, 3(3):388–399, Mar 2012.
- [97] Anuja Nair, Barry D. Kuban, E. Murat Tuzcu, Paul Schoenhagen, Steven E. Nissen, and D. Geoffrey Vince. Coronary plaque classification with intravascular ultrasound radiofrequency data analysis. *Circulation*, 106(17):2200–2206, 2002.

- [98] Rishi Puri, Matthew I. Worthley, and Nicholls Stephen J. Intravascular imaging of vulnerable coronary plaque: current and future concepts. *Nature Reviews Cardiology*, 8(3):131–139, 2011.
- [99] Joseph F. Polak. Carotid ultrasound. *Radiologic Clinics of North America*, 39(3):569–589, 2001.
- [100] Bruce A. Wasserman. Advanced contrast-enhanced mri for looking beyond the lumen to predict stroke: Building a risk profile for carotid plaque. *Stroke*, 41(10 suppl 1):S12–S16, 2010.
- [101] Yuji Watanabe and Masako Nagayama. Mr plaque imaging of the carotid artery. *Neuroradiology*, 52(4):253–274, 2010.
- [102] Guillermo J. Tearney, Sergio Waxman, Milen Shishkov, Benjamin J. Vakoc, Melissa J. Suter, Mark I. Freilich, Adrien E. Desjardins, Wang-Yul Oh, Lisa A. Bartlett, Mireille Rosenberg, and Brett E. Bouma. Three-dimensional coronary artery microscopy by intracoronary optical frequency domain imaging. *JACC: Cardiovascular Imaging*, 1(6):752 – 761, 2008.
- [103] Aydogan Ozcan, Alberto Bilenca, Adrien E. Desjardins, Brett E. Bouma, and Guillermo J. Tearney. Speckle reduction in optical coherence tomography images using digital filtering. *J. Opt. Soc. Am. A*, 24(7):1901–1910, Jul 2007.
- [104] J K Williams, M L Armstrong, and D D Heistad. Vasa vasorum in atherosclerotic coronary arteries: responses to vasoactive stimuli and regression of atherosclerosis. *Circulation Research*, 62(3):515–23, 1988.
- [105] Pedro R. Moreno, K-Raman Purushothaman, Marc Sirol, Andrew P. Levy, and Valentin Fuster. Neovascularization in human atherosclerosis. *Circulation*, 113(18):2245–2252, 2006.

- [106] Alexander C. Langheinrich, Agata Michniewicz, Daniel G. Sedding, Gerhard Walker, Patricia E. Beighley, Wigbert S. Rau, Rainer M. Bohle, and Erik L. Ritman. Correlation of vasa vasorum neovascularization and plaque progression in aortas of apolipoprotein e//low-density lipoprotein/ double knockout mice. *Arteriosclerosis, Thrombosis, and Vascular Biology*, 26(2):347–352, 2006.
- [107] Reza Motaghiannezam and Scott Fraser. Logarithmic intensity and speckle-based motion contrast methods for human retinal vasculature visualization using swept source optical coherence tomography. *Biomed. Opt. Express*, 3(3):503–521, Mar 2012.
- [108] Alexander Doronin and Igor Meglinski. Imaging of subcutaneous microcirculation vascular network by double correlation optical coherence tomography. *Laser & Photonics Reviews*, 7(5):797–800, 2013.
- [109] Xiang Liu and L. Hanzo. A unified exact ber performance analysis of asynchronous ds-cdma systems using bpsk modulation over fading channels. *Wireless Communications, IEEE Transactions on*, 6(10):3504–3509, October 2007.
- [110] David W. Cadotte, Adrian Mariampillai, Adam Cadotte, Kenneth K. C. Lee, Tim Rasmus Kiehl, Brian C. Wilson, Michael G. Fehlings, and Victor X. D. Yang. Speckle variance optical coherence tomography of the rodent spinal cord: in vivo feasibility. *Biomed. Opt. Express*, 3(5):911–919, May 2012.
- [111] Jamie McDonald, Pinar Bayrak-Toydemir, and Reed E. Pyeritz. Hereditary hemorrhagic telangiectasia: An overview of diagnosis, management, and pathogenesis. *Genetics in Medicine*, 13(7):607–616, 2011.
- [112] Shou-jiang Tang, Maggie L. Gordon, Victor X.D. Yang, Marie E. Faughnan, Maria Cirocco, Bing Qi, Emily Seng Yue, Geoffrey Gardiner, Gregory B. Haber, Gabor Kandel, Paul Kortan, Alex Vitkin, Brian C. Wilson, and Norman E. Marcon.

- In vivo doppler optical coherence tomography of mucocutaneous telangiectases in hereditary hemorrhagic telangiectasia. *Gastrointestinal Endoscopy*, 58(4):591–598, 2003.
- [113] Wolfgang Wieser, Thomas Klein, Desmond C. Adler, Francois Trépanier, Christoph M. Eigenwillig, Sebastian Karpf, Joseph M. Schmitt, and Robert Huber. Extended coherence length megahertz fdml and its application for anterior segment imaging. *Biomed. Opt. Express*, 3(10):2647–2657, Oct 2012.
- [114] Vyacheslav Kalchenko, Yuri Kuznetsov, Igor Meglinski, and Alon Harmelin. Label free in vivo laser speckle imaging of blood and lymph vessels. *Journal of Biomedical Optics*, 17(5):050502–1–050502–3, 2012.
- [115] Vyacheslav Kalchenko, Noa Madar-Balakirski, Igor Meglinski, and Alon Harmelin. In vivo characterization of tumor and tumor vascular network using multi-modal imaging approach. *Journal of Biophotonics*, 4(9):645–649, 2011.
- [116] I. M. Braverman, A. Keh, and B. S. Jacobson. Ultrastructure and three-dimensional organization of the telangiectases of hereditary hemorrhagic telangiectasia. *Journal of Investigative Dermatology*, 95(4):422–427, 1990.
- [117] Sung Ok Park, Mamta Wankhede, Young Jae Lee, Eun-Jung Choi, Naime Fliess, Se-Woon Choe, Seh-Hoon Oh, Glenn Walter, Mohan K. Raizada, Brian S. Sorg, and S. Paul Oh. Real-time imaging of de novo arteriovenous malformation in a mouse model of hereditary hemorrhagic telangiectasia. *The Journal of Clinical Investigation*, 119(11):3487–3496, 11 2009.
- [118] Eun-Jung Choi, Wanqiu Chen, Kristine Jun, Helen M. Arthur, William L. Young, and Hua Su. Novel brain arteriovenous malformation mouse models for type 1 hereditary hemorrhagic telangiectasia. *PLoS ONE*, 9(2):e88511, 02 2014.

- [119] Jennifer Barton and Steven Stromski. Flow measurement without phase information in optical coherence tomography images. *Opt. Express*, 13(14):5234–5239, Jul 2005.
- [120] Günay Yurtsever, Nicolás Weiss, Jeroen Kalkman, Ton G. van Leeuwen, and Roel Baets. Ultra-compact silicon photonic integrated interferometer for swept-source optical coherence tomography. *Opt. Lett.*, 39(17):5228–5231, Sep 2014.
- [121] Günay Yurtsever, Boris Považay, Aneesh Alex, Behrooz Zabihian, Wolfgang Drexler, and Roel Baets. Photonic integrated mach-zehnder interferometer with an on-chip reference arm for optical coherence tomography. *Biomed. Opt. Express*, 5(4):1050–1061, Apr 2014.
- [122] V. Duc Nguyen, N. Weiss, W. Beeker, M. Hoekman, A. Leinse, R. G. Heideman, T. G. van Leeuwen, and J. Kalkman. Integrated-optics-based swept-source optical coherence tomography. *Opt. Lett.*, 37(23):4820–4822, Dec 2012.
- [123] Ho Yiu Cheng, Jason Grenier, and Peter R. Herman. Femtosecond laser-written couplers in fused silica fiber: Towards fiber cladding optical circuits. In *CLEO: 2013*, page CM1H.3. Optical Society of America, 2013.
- [124] Daguang Xu, Yong Huang, and Jin U. Kang. Volumetric (3d) compressive sensing spectral domain optical coherence tomography. *Biomed. Opt. Express*, 5(11):3921–3934, Nov 2014.